Quantitative Characterization of 3D Deformations of Cell Interactions with Soft Biomaterials

Thesis by

Christian Franck

In Partial Fulfillment of the Requirements

for the Degree of

Doctor of Philosophy

California Institute of Technology

Pasadena, California

2008

(Defended May 14, 2008)

To my parents, Jen, Angie and Blitz

Acknowledgments

I would like to begin by thanking all of my friends whom I have interacted with over the course of my five years here at Caltech. Your friendship, interactions and discussions have made my experience at Caltech truly rewarding, enriching and wonderful. In particular, I would like to thank some outstanding individuals who have made my personal and academic adventures at Caltech particularly special. Foremost, I want to thank my advisor Professor Ravichandran who besides many things taught me that nothing is ever impossible no matter how insurmountable the task may seem. I would like to thank him for making all my endeavors possible and providing me with so many wonderful opportunities, for that I am truly grateful.

I want to thank Professor Tirrell for mentoring me throughout my final years at Caltech, and for giving me all of the wonderful research opportunities. I also want to thank Professor Bhattacharya for all of his advice and support in my various academic projects. I would like to thank Professors Knauss and Daraio for all the fruitful discussions and support throughout my thesis work. I want to thank Stacey Maskerinec for her friendship and for spending many endless hours working with me side by side, from imaging photopatterns to electrospinning poly-vinyl-alcohol at 36,000 Volts to making more than 300 hundred agarose and polyacrylamide samples. I want to thank Dr. Soonsung Hong for working with me to bring the first stage of this project to life, and for developing the digital volume correlation code, in particular the stretch-correlation algorithm. I also want to thank him for teaching me the ins-and-outs of Matlab, and for his mentorship overall. I want to thank Petros Arakelin for his ingenuity and work on all of my home-built little devices, and for insights and advice on the many different projects I have worked on. I am particularly grateful (and I am sure the little fibroblast cells are too) for always keeping the arterial blood gas flowing, day and

night. I want to thank Linda Miranda not only for being the best assistant ever, but also for many funny and joyful conversations including random trips to the bookstore and the post office. I want to gratefully acknowledge the funding support for this project sponsored by the National Science Foundation through their Materials Research Science and Engineering Center at Caltech. I would like to thank Winston Jackson for his friendship and all the great discussions both academically and personally during my time at Caltech.

I want to thank my family, my parents Barbara and Walter for always supporting me in pursuing my dreams, and my siblings Philipp, Julie and Max for whose support and love I am so thankful. Finally, I want to thank my wonderful wife, Jen, who has contributed so much to the person I am today. For her continuous and unconditional love and support, I will be forever grateful.

Abstract

In recent years, the importance of mechanical forces in directing cellular function has been recognized as a significant factor in biological and physiological processes. In fact, these physical forces are now viewed equally as important as biochemical stimuli in controlling cellular response. Not only do these cellular forces, or cell tractions, play an important role in cell migration, they are also significant to many other physiological and pathological processes, both at the tissue and organ level, including wound healing, inflammation, angiogenesis, and embryogenesis. A complete quantification of cell tractions during cell-material interactions can lead to a deeper understanding of the fundamental role these forces play in cell biology. Thus, understanding the function and role of a cell from a mechanical framework can have important implications towards the development of new implant materials and drug treatments.

Previous research has contributed significant descriptions of cell-tissue interactions by quantifying cell tractions in two-dimensional environments; however, most physiological processes are three-dimensional in nature. Recent studies have shown morphological differences in cells cultured on two-dimensional substrates versus three-dimensional matrices, and that the intrinsic extracellular matrix interactions and migration behavior are different in three dimensions versus two dimensions. Hence, measurement techniques are needed to investigate cellular behavior in all three dimensions.

This thesis presents a full-field imaging technique capable of quantitatively measuring cell traction forces in all three spatial dimensions, and hence addresses the need of a three-dimensional quantitative imaging technique to gain insight into the fundamental role of physical forces in biological processes. The technique combines laser scanning confocal microscopy (LSCM) with digital volume correlation (DVC) to track the motion of fluorescent particles during cell-induced or ex-

ternally applied deformations. This method is validated by comparing experimentally measured non-uniform deformation fields near hard and soft spherical inclusions under uniaxial compression with the corresponding analytical solution. Utilization of a newly developed computationally efficient stretch-correlation and deconvolution algorithm is shown to improve the overall measurement accuracy, in particular under large deformations.

Using this technique, the full three-dimensional substrate displacement fields are experimentally determined during the migration of individual fibroblast cells on polyacrylamide gels. This is the first study to show the highly three-dimensional structure of cell-induced displacement and traction fields. These new findings suggest a three-dimensional push-pull cell motility, which differs from the traditional theories based on two-dimensional data. These results provide new insight into the dynamic cell-matrix force exchange or mechanotransduction of migrating cells, and will aid in the development of new three-dimensional cell motility and adhesion models.

As this study reveals, the mechanical interactions of cells and their extracellular matrix appear to be highly three-dimensional. It also shows that the LSCM-DVC technique is well suited for investigating the mechanics of cell-matrix interactions while providing a platform to access detailed information of the intricate biomechanical coupling for many cellular responses. Thus, this method has the capability to provide direct quantitative experimental data showing how cells interact with their surroundings in three dimensions and might stimulate new avenues of scientific thought in understanding the fundamental role physical forces play in regulating cell behavior.

Contents

List of Figures

List of Tables

Chapter 1

Introduction

1.1 Mechanics in the Context of Cell Biology

Mechanical forces play an important role in the activities of our daily lives from sitting to lifting objects to running. During all of these activities our bones and ligaments experience cycles of different mechanical loads, and need to adjust accordingly. For example, a runner's foot constantly experiences physical forces as it periodically impacts the ground. These forces are balanced by the runner's joints and bones, where the bone carries some of the compressive loading. If we examine the structure of the runner's bone in more detail, we would find a fairly porous structure made up of mostly calcium phosphate and collagen fibers, much resembling a light-weight composite structure. Intertwined with this structure are cells, some of which are constantly remodeling and restructuring the bone adjusting to the external loading.

In fact, one can think of the bone as an active mechanical system in which a particular type of cells called osteocytes act as mechanosensors. These "sensor" cells can communicate with other cells through an intricate feedback system to ensure the health or homeostasis of the bone itself. In particular, two of the cells with which osteocytes communicate are osteoblasts and osteoclasts. Osteoblasts are responsible for bone remodeling or remineralization. Osteoclasts, on the other hand, are in charge of removing or resorbing bone. So, in order to maintain a healthy bone structure, the activities of osteoblasts and osteoclasts need to be balanced.

However, since this system is based upon an active feedback loop, if the external mechanical

loading were to be removed, as in the case of an astronaut in space (zero-gravity environment), then the osteoblasts will cease to create more healthy bone structure due to the absence of the mechanical stimulus. Another type of imbalance is created in the case of osteoporosis, where insufficient osteoblasts exist to counteract the bone removal created by the more numerous osteoclasts. Of course this is a simplification of a delicate biochemical and mechanical system, which needs to be fully understood in order to maintain healthy, long-lasting bones.

Another example of the importance mechanical forces play in cellular behavior, is when tumor cells metastasize, or spread to the surrounding tissue in the body. In this case, as the tumor cells spread from their primary site they must venture through a jungle of extracellular proteins, such as proteoglycans, collagen, and elastin fibers collectively known as the extracellular matrix (ECM). For these malignant cells to successfully reach the arterial walls they need to push, squeeze, and cleave their way through the ECM, which involves exerting mechanical forces. Yet unfortunately, this migration mechanism, in particular the three-dimensional cell-matrix force exchange is relatively poorly understood.

As suggested by the above examples, there is an established connection between mechanical forces and cellular function [45]. In fact, these physical forces are today viewed equally as important as biochemical stimuli in directing cellular response. The translation of mechanical forces into biochemical signals that are responsible for determining cellular behavior is coined *mechanotransduction* [23]. Since the purpose of this investigation focuses on the physical interactions of cells and their ECM, the following overview presents a rather simplified version of the intricate interplay between mechanical forces and biochemical signaling, which can be found in more detail elsewhere [7, 24, 29, 36].

There are at least three ways in which mechanical forces can introduce biochemical signals [53]. The first one involves the opening and closing of cell membrane ion channels, which are activated through physical stresses. The second consists of the unraveling of protein molecules by mechanical forces, thus opening up previously hidden or cryptic binding sites. In the third, the application of physical forces can stabilize chemical bonds that are otherwise unstable or short-lived. However, for

these forces to take place, the cell needs to anchor itself to the surrounding ECM. These particular anchor points that connect the cell to the ECM are called focal adhesion sites. They serve as a gateway for the cell to transmit its internal forces to the ECM and vice versa.

Internal cellular forces are created through the interaction of actin with myosin II. Actin is one of the three structural elements found inside the cell, beside microtubules and intermediate filaments. Actin filaments can form long bundles also known as stress fibers that form a collaborate intracellular network that connects the focal adhesion sites (e.g., α and β integrins), much like truss structures support a steel bridge. Myosin II is a molecular motor protein that hydrolizes adenosine-5′-triphosphate (ATP) for energy, and induces contraction of the actin framework. The cell membrane has receptors or integrins that connect to the ECM proteins or ligands at the focal adhesion site. Cell contraction is first felt by actin, then transmitted to the membrane receptors across a multitude of focal adhesion proteins and finally to the ECM ligands. In order for the cell to move, all it needs to do is to detach from a particular focal adhesion site, thus creating a force imbalance. Not only do these cellular forces or cell traction forces play an important role in cell migration, they are also significant to many other physiological and pathological processes, both at the tissue and organ level. Some of these include wound healing, inflammation, angiogenesis, and embryogenesis [54]. Hence, quantification and understanding of their nature and regulation become an important part for the development of new implant material and drug treatments.

1.2 Previous Work on Quantifying Cell-ECM Interactions

Within the last few decades, studies began to quantify surface traction forces that are developed by migrating cells through a variety of techniques. In 1980 Harris et al. demonstrated that cellular forces could be visualized by creating thin elastic silicone rubber substrates and tracking the wrinkle formation response to the cell's applied stresses [20]. However, since wrinkle formation or buckling is an intrinsically nonlinear and unstable process, the quantitative characterization using this technique is difficult. In 1995 Oliver et al. and Dembo et al. developed a quantitative, non-wrinkling technique called *traction force microscopy (TFM)* to study fibroblast migration on two-dimensional

substrate surfaces [13, 34, 27]. This method utilizes optical phase and wide-field microscopy to track substrate surface displacements due to cellular traction forces via fluorescent particles embedded in a polyacrylamide substrate. This technique is currently one of the most widely used methods in determining cellular traction forces that are part of the mechanotransduction process. It will be described in more detail within the next section.

Another method to determine cell-induced traction forces was proposed by Tan et al. in 2003 where, instead of using fluorescent beads, thin cantilevers (micro needle-like posts) are fabricated out of poly-dimethylsiloxane (PDMS) substrates, from which traction forces can be calculated according to linear beam theory [49]. This method produces similar spatial resolution as the TFM technique on the micrometer scale with resolved forces of the order of nano-Newtons. Yet another approach demonstrated by Balaban *et al.* relies on displacement measurements of submicron patterned dots on PDMS susbtrate. However, both this technique and TFM employ an inverse Bousinessq formulation to convert the observed displacements into traction forces as will be explained later. Although these reports have contributed much to describing cell behaviors in two-dimensional environments, many physiological processes are three dimensional in nature and recent studies have not only shown morphological differences in cells cultured on two-dimensional substrates versus three-dimensional matrices, but their intrinsic ECM interactions and migration behavior also appears different [12, 16, 55]. Yet few advances have been made to address the need for three-dimensional quantitative imaging techniques [32]. Thus, a new class of experimental tools capable of quantitatively capturing such interactions is needed for more in-depth studies. This thesis presents a three-dimensional imaging technique capable of quantitatively measuring cell traction forces in all three spatial dimensions.

1.2.1 Traction Force Microscopy (TFM)

As previously mentioned probably the most wide-spread technique for investigating cellular traction forces utilizes traction force microscopy [7, 41, 14, 38]. This method measures surface displacement using either a single-particle or digital image correlation (DIC) based approach between two successive images. In most studies submicron fluorescent tracker particles are embedded in poly-

acrylamide or similar polymer based substrates with typical Young's moduli ranging from $\sim$ 1 - 30 kPa [14, 7, 38]. Balaban et al. used a geometrical pattern stamped into PDMS to track cell-induced surface displacements. To record cell surface deformations, cells are initially seeded on the substrate material and allowed to spread and migrate. After some time, a first image is recorded via an optical microscope, where typically both the cell and the tracker particles are recorded simultaneously. Then, the cells are chemically detached from the surface involving cleaving proteases such as trypsin to disrupt all cell substrate attachments. Without moving the microscope objective another image is captured serving as the undeformed or reference configuration. The two-dimensional full-field displacements are then determined from the set of the two images by either using a single particle tracking or digital image correlation algorithm.

In order to determine the cell-induced surface traction forces from the recorded displacement data, the Boussinesq formulation is utilized. The Boussinesq theory describes the displacement equilibrium solutions inside a semi-infinite elastic half-space with applied forces at its free boundary (surface) via the governing equation

$$\nabla(\nabla \cdot \mathbf{u}(\mathbf{x})) + (1 - 2\nu)\nabla^2 \mathbf{u}(\mathbf{x}) = 0 \tag{1.1}$$

where $\mathbf{u}(\mathbf{x})$ is the three-dimensional displacement vector, and ν is the Poisson's ratio of the linearly elastic material. The details of the derivation in formulating the solution is given by Landau and Lifshitz [25], so only the end result is presented here. The displacement field $\mathbf{u}(\mathbf{x})$ in the semi-infinite half space can be written as a convolution integral with the Green's tensor $\mathbf{G}(\mathbf{x})$ and the applied surface traction forces given by

$$u_i = \int\int G_{ik}(\mathbf{x}_1 - \mathbf{x}'_1, \mathbf{x}_2 - \mathbf{x}'_2, \mathbf{x}_3 - \mathbf{x}'_3) P_k(\mathbf{x}'_1, \mathbf{x}'_2) d\mathbf{x}'_1 d\mathbf{x}'_2, \quad (i, j, k = 1, 2, 3) \tag{1.2}$$

where the surface traction forces $P_k(\mathbf{x}'_1, \mathbf{x}'_2)$ at a particular location $(\mathbf{x}'_1, \mathbf{x}'_2)$ are expressed as

$$P_k = F\delta(\mathbf{x}'_1)\delta(\mathbf{x}'_2), \tag{1.3}$$

where F is a concentrated surface force. In the TFM calculations, Eq. 1.2 is simplified by setting ν = 0.5, and assuming only two-dimensional, in-plane displacements resulting in,

$$G_{\alpha\beta}(\mathbf{r}) = \frac{3}{4\pi E r}(\delta_{\alpha\beta} + \frac{x_\alpha x_\beta}{\mathbf{r}^2}), \quad \mathbf{r} = \sqrt{\mathbf{x}_1^2 + \mathbf{x}_2^2}. \tag{1.4}$$

Finally, in order to determine the surface traction forces Eq. 1.2 needs to be discretized and inverted. However, the inversion of this problem is ill posed, especially in the presence of noise in the displacement data, and thus requires regularization schemes to calculate the traction forces accurately [14, 42]. Butler et al. addressed this issue and developed an approach of performing the inverse calculations in Fourier space and noted that the Fourier transform of the Green's tensor is diagonal and invertible without regularization or other modifications to the problem [7].

While the Boussinesq solution provides an approach to determine surface tractions and traction forces directly, it depends on the assumption of a semi-infinite elastic half-space or an elastic substrate of finite thickness. However, the criterion of when a substrate can be treated as infinitely thick is difficult to assess without any direct information about the deformation extending in the third spatial dimension (i.e. the thickness direction). It has been shown that the Boussinesq solution underestimates the forces when cells are seeded on gels ranging from 5 - 60 μm thick, and that finite height corrections are necessary [31]. To apply the Boussinesq solution, one must ensure that the displacement data is indeed recorded at the free surface, which is difficult to determine without depth information.

Another limitation to the conventional TFM formulation is that extreme care must be exercised when recording two-dimensional image data to ensure no focal (out-of-plane) drift occurs during imaging. This is especially challenging when imaging biological systems that require constant physiological temperature (37°C), where thermal drift is likely to occur.

Although these reports have contributed much to describing cell behaviors in two-dimensional environments, it has been recently demonstrated that many cell types show distinct three-dimensional morphologies and interactions, as expected *in vivo* [12, 16, 55]. Therefore the extension of TFM into the third spatial dimension has the capability to provide a more complete picture of cell-ECM

interactions.

1.3 Previous Digital Volume Correlation (DVC) Techniques

To extend the existing two-dimensional traction force microscopy techniques into three-dimensional, a different set of instruments and algorithms needs to be utilized. A few recent studies have begun to develop quantitative three-dimensional imaging techniques using X-ray tomography and laser scanning confocal microsopy in conjunction with digital volume correlation. In 1998 Bay *et al.* first proposed an extension of the DIC method into three-dimensional and named it digital volume correlation (DVC) [4]. In their study, volumetric images were acquired using X-ray tomography of trabecular bone, where the microstructure of the porous bone is used as a tracking pattern. Analagous to DIC, DVC algorithms divide the entire volume image into smaller sized subsets. Bay *et al.* based their correlation algorithm on the translation of the center of these subsets only, where terms in the deformation gradient are ignored. In 2002 Smith *et al.* refined the existing DVC algorithm developed by Bay *et al.* by accounting for finite rotations, presenting an improvement in the overall accuracy of the technique when rotations exceed 0.05 radians [46, 9]. Their study utilized a micro computer tomography scanner and aluminum foam samples, where again the material microstructure was used as the tracking pattern. In 2004 Roeder *et al.* combined a translation-based only DVC algorithm similar to Bay *et al.* with laser scanning confocal microscopy to measure the three-dimensional deformations of a collagen based gel under uniaxial tension. To track material displacements they utilized the native material microstructure under autofluorescent illumination [39]. In 2005 Pizzo *et al.* applied the translation-based DVC and LSCM method developed by Roeder *et al.* to measure volumetric strain and cell area in human dermal fibroblast cells encapsulated in collagen I extracellular matrices. The purpose of this study was to investigate the role of collagen fibril density in regulating local cell-ECM behavior. In particular, the connection between cell shape and proliferation as a function of fibril density was examined. Again, the microstructure of the collagen-based ECM was used to track cell mediated displacements [37]. Throughout these studies

it was found that DVC subsets of the size 64 x 64 x 64 voxels[1] gave optimal correlation results, while the subset spacing or grid resolution was typically between 64 - 16 voxels due to computational constraints.

1.4 Accomplishments

This thesis presents a quantitative imaging technique using laser scanning confocal microscopy (LSCM) and digital volume correlation (DVC). This technique has the capability of determining the three-dimensional full-field displacements inside transparent materials, in particular, soft biomaterials. This technique was validated by comparing experimentally measured displacement and strain field data obtained from uniaxial compression and spherical inclusion tests, and obtained excellent agreement with the predicted analytical solution [18]. Next, this method was applied to migrating single cells on the surface of polyacrylamide substrates and successfully captured the three-dimensional deformation fields induced by these cells. This demonstrates that the newly developed LSCM and DVC method has the capability of quantitatively capturing the three-dimensional mechanical interaction of cells and their extracellular matrix.

One of the advantages of the developed three-dimensional quantitative imaging technique over those reported previously [4, 46, 39] is that the method presented here takes into consideration the stretch deformation of each volume subset. This allows for a more accurate strain estimate, especially when local strains are large and subset deformation is significant. Another advantage over previous studies is the addition of a deconvolution algorithm, which minimizes the blurring of confocal images. Thus, the overall resolution of the images, in particular along the optical axis, is significantly improved leading to an increase in the accuracy of the subsequent DVC calculations. Also advantageous over previous studies is that the presented results do not depend on the local sample feature size to achieve high correlation resolution, but rather can be tailored to the relevant length scale of interest. This is achieved by utilizing commercially available fluorescent markers rather than relying on autofluorescence of the sample, which can limit the field of view. The method

[1] A voxel is generally defined as a three-dimensional pixel.

presented here allows the user to choose virtually any field of view provided the appropriate markers are available. Using this method, locally varying displacement and strain fields around motile cells are determined in all three spatial dimensions. Also, this technique can be used to experimentally determine the material properties of soft materials, especially where conventional characterization techniques fail due to the compliant nature of the material.

In the second part of this thesis, an application of the new LSCM and DVC technique to live cell systems is described. In particular, it presents the time-dependent measurements of the three-dimensional deformations induced by single migrating fibroblasts on polyacrylamide substrates. Results are presented for cell-induced displacements and cellular traction forces information during different stages of cell movement in all three dimensions for the first time. While the focus in this study was to track single cell material deformations, this technique is capable of measuring three-dimensional deformation fields of cell clusters and cell sheets of many different cell types.

Chapter 1 has described the motivation of this project and presented a literature review of the crossroads between biochemistry and mechanics in cell-matrix interactions followed by the currently employed two-dimensional (two-dimensional) traction force methodologies. It also reviewed previous developments in digital volume correlation, and concluded by stating the accomplishments of this thesis. The remainder of this the thesis is organized as follows:

Chapter 2 presents the development of the quantitative full-field three-dimensional imaging technique based on laser scanning confocal microscopy and digital volume correlation, and its validation. Chapter 3 describes the experimental setup of the cell system, which has been chosen as an application of the developed quantitative imaging method. Chapter 4 presents the experimental findings and observations of applying the LSCM-DVC method to migrating fibroblast cells on polyacrylamide substrates. Lastly, Chapter 5 concludes this study by providing a summary of findings, including preliminary experimental observations on cells interacting with artificial extracellular matrix (aECM) proteins, and provides recommendations for future work.

Chapter 2

Development of a Quantitative Full-Field, Three-Dimensional Imaging Technique

This chapter describes the development of a quantitative, full-field three-dimensional imaging technique for measuring deformations in solids including transparent soft materials. The method presented here employs a laser scanning confocal microscope to acquire three-dimensional volumetric images, while a digital volume correlation algorithm is used to determine the full field displacements. In particular, the DVC computes the displacement of fluorescent microparticles embedded in a transparent agarose polymer. What follows is a detailed presentation of the quantitative full field three-dimensional imaging technique development and its validation, including in-depth description of laser scanning confocal microscopy (LSCM) and digital volume correlation (DVC).

2.1 Laser Scanning Confocal Microscopy (LSCM)

This section presents an overview of laser scanning confocal microscopy and discusses how its resolution along the optical imaging axis can be improved by means of a computationally efficient deconvolution algorithm.

2.1.1 Overview of Laser Scanning Confocal Microscopy

Confocal microscopy has emerged as a powerful imaging technique due to its optical sectioning capability, which enables construction of three-dimensional images. In conventional wide-field microscopy, light is collected from the entire sample volume, including the focal plane as well as all other planes. In confocal microscopy light is generally collected from the focal plane only. This is achieved by using a pinhole in front of a photomultiplier tube (PMT) detector that blocks the incoming light from all other planes. As illustrated in Fig. 2.1, the solid line represents light reflected or emitted from the focal plane, while the dashed lines represent light from the out-of-focus planes.

The overall contrast and resolution of the image is significantly increased as compared to conventional wide-field microscopy where the image is blurred by out-of-plane light. As a consequence, the inherent optical sectioning of the specimen in confocal microscopy allows the assembly of three-dimensional image volumes by stacking together individually acquired planar slices. In an LSCM system, a laser with a single-diffraction limited spot size is used to sequentially scan a selected focal plane. Thus, the image is not formed using a CCD camera as in conventional microscopy, but rather the image is a result of the lights interaction with successive areas of the specimen, i.e., the image is recorded pixel by pixel, analogous to a scanning electron microscope (SEM). The resulting image is generally superior in resolution to images recorded by conventional optical microscopy. The spatial resolution of a confocal microscope is determined by the three-dimensional point spread function (PSF), which is an intensity distribution near the focal point corresponding to a volume image of a point light source under a diffraction-limited imaging system. Thus, the obtained confocal image is the convolution of actual intensity distributions using the point spread function as

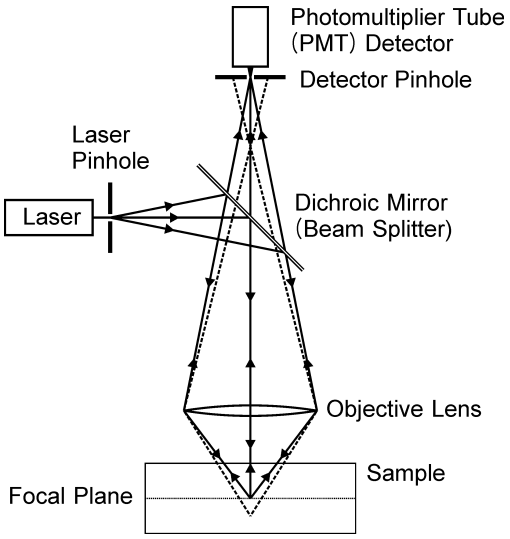

Figure 2.1: Illustration of the confocal imaging principle (solid lines = in-focus light; dashed lines = out-of-focus light)

a kernel or an optical impulse response function. A given point spread function will depend on each imaging situation but is typically a function of the imaging wavelength, λ, refractive index surrounding the lens, n, the numerical aperture of the lens, NA, and the image magnification. The numerical aperture of a lens can be expressed as $NA = nsin\theta$, where θ is the half angle of the light cone collected by the microscope lens. Following the derivations given by Stevens *et al.* [47], a representive expression for the intensity distribution of the point spread function along the lateral and optical imaging axis (u, v) gives

$$h^2[u, v] = | \int_0^1 J_0[v\rho]exp(iu\rho^2/2)\rho d\rho|^2, \tag{2.1}$$

where ρ is the radial distance from the optical axis and J_0 is the Bessel function of order zero. The optical coordinates u and v are related to the spatial coordinates r and z by

$$v = \frac{2\pi}{\lambda}(NA)r, \quad u = \frac{2\pi}{\lambda}(NA)^2 z/n, \tag{2.2}$$

where r is the radial distance from the optical axis, and z is the distance from the focal plane. Figure 2.2 shows a typical line intensity plot of the above point spread function expression both along the lateral and optical imaging axis. The lateral intensity profile of the point spread function in the focal plane, i.e., $h^2[0, v]$, gives the known line profile of the Airy disk[1]. Using Eqs. 2.2, estimates on the typical lateral and axial resolutions can be formulated by using the generally adopted Rayleigh criterion. This criterion states that the ultimate lateral resolution of the optical system is determined by the first zero of the Airy pattern or J_0.

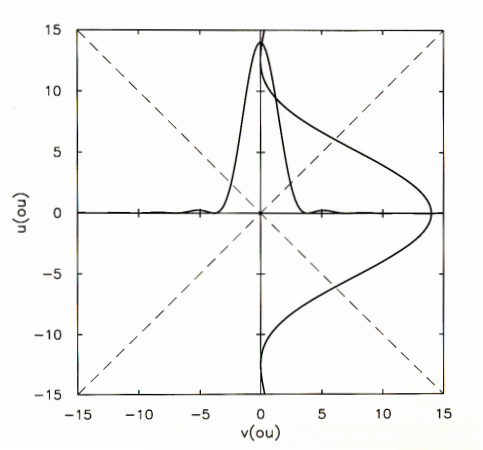

Figure 2.2: Profiles of the PSF for $u = 0$ (lateral), and $v = 0$ (vertical) from Stevens *et al.* [47]. The units of u and v are arbitrary optical units (ou). The peak widths determine the resolution.

[1]The interference pattern created from light diffracting through a circular aperture is known as the Airy disk

Following the same criterion in determining the axial direction, both lateral and axial resolution limits can be estimated as

$$Resolution_{lateral} = 0.61\frac{\lambda}{NA}, \tag{2.3}$$

and

$$Resolution_{axial} = 1.4\frac{n\lambda}{NA^2}. \tag{2.4}$$

This result is shown graphically in Fig. 2.2 by the width of both lateral and axial intensity peaks. Further details describing the confocal principle, including a more rigorously mathematical treatment of confocal imaging and the current applications of confocal microscopy, are well documented and can be found elsewhere [11, 43, 47, 19] . The next section will describe a method to improve the axial resolution of LSCM by accounting for the effects of the point spread function.

2.1.2 Improving Axial Resolution through Deconvolution

Figure 2.2 illustrates the differences in the lateral and axial resolutions during confocal imaging. As can be seen, the axial resolution of confocal imaging is typically three to ten times worse than the lateral resolution depending on the refractive index of the medium and the numerical aperture of the objective lens. In Fig. 2.3, an isosurface[2] plot of a typical confocal subvolume image (64 x 64 x 64 voxels) of a transparent agarose gel with randomly dispersed fluorescent spherical particles of two voxels in diameter is shown. A voxel is defined as a pixel in three-dimensional space, which in the present case is equal to 0.45 μm. The spherical fluorescent particles appear as axially elongated ellipsoids. The blurring in the axial direction causes increased uncertainties in the digital volume correlation measurements of the axial direction components. The consequence of such blurring is particularly critical to the performance of the large deformation digital volume correlation algorithm that uses the Fourier power spectrums. In this study, the noise-resistant Lucy-Richardson deconvolution algorithm [30] was used to deconvolve the raw confocal images using the following point

[2] An isosurface is a surface consisting of points of constant value

spread *sinc* function (PSF),

$$PSF = \frac{sin(x_3)}{x_3}, \tag{2.5}$$

in the axial direction prior to the stretch correlation. The appropriateness of using a *sinc* function in approximating the three-dimensional point spread function can be seen in Fig. 2.2, and from Eq. 2.1, where $h^2[u, 0]$ describes a typical *sinc* profile. Figure 2.4 shows the subvolume from Fig. 2.3 after deconvolution of the raw image.

There are two additional confocal-imaging artifacts caused by the refractive index mismatch in the optical path. First, spherical aberration due to the refractive index mismatch causes asymmetric distortions of the three-dimensional point spread function as a function of the penetration depth. Such a distorted and depth-dependent point spread function makes the deconvolution of the confocal images difficult and causes significant error in the digital volume correlation. Effects of such spherical aberration in confocal imaging have been extensively studied in the past [51, 44]. In practice, the spherical aberrations can be minimized by adjusting the correction collar commonly found in commercial microscope objectives. In order to minimize the distortion of the point spread function within the field of view, the correction collar needs to be adjusted appropriately prior to each test. The second form of confocal imaging artifact due to the refractive index mismatch is caused by the fact that the focal point does not follow the axial motion of the scanning stage [52, 15]. This causes an over- or under-estimation of the depths depending on the ratio of the refractive indeces. This apparent discrepancy between the axial and the lateral scanning resolutions can be calibrated by imaging large fluorescent microspheres embedded in a sample.

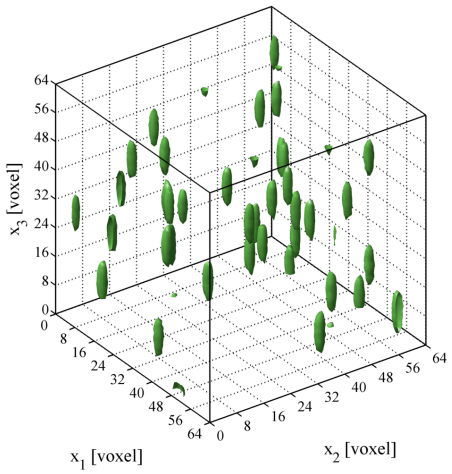

Figure 2.3: Isosurface plot of fluorescent particles as recorded by LSCM (1 voxel = 0.45 µm)

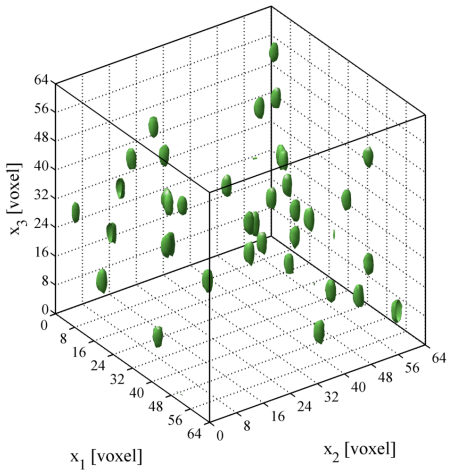

Figure 2.4: Isosurface plot of fluorescent particles after deconvolution of the PSF (1 voxel = 0.45 µm)

2.2 Digital Volume Correlation (DVC)

2.2.1 Principle of DVC

LSCM provides discretized volume images visualizing three-dimensional structural patterns of fluorescent markers in a transparent sample. In this study, the combination of digital volume correlation (DVC) and confocal images is used to achieve three-dimensional full-field deformation measurements as an extension of the vision-based surface deformation measurement techniques, well-known as digital image correlation (DIC) [10]. The basic principle of the DVC is schematically illustrated in Fig. 2.5. Two confocal volume images of an agarose gel with randomly dispersed fluorescent particles are obtained before and after mechanical loading.

Then, the two images are subdivided into a set of subvolumes that are centered on the points of interest. Using each pair of corresponding subvolume images, the respective local displacement vector can be obtained from three-dimensional volume correlation methods. Consider two scalar signals $f(\mathbf{x})$ and $g(\mathbf{x})$ which represent a pair of intensity patterns in a subvolume Ω before and after a continuous mapping, $\hat{\mathbf{y}}(\mathbf{x})\colon \mathbf{x} \rightarrow \mathbf{y}$, respectively. Assuming that the signal is locally invariant during the mapping, $f(\mathbf{x}) = g(\mathbf{y}(\mathbf{x}))$, correlation matching by subvolume can be obtained by finding an optimal mapping that maximizes the cross-correlation functional defined as

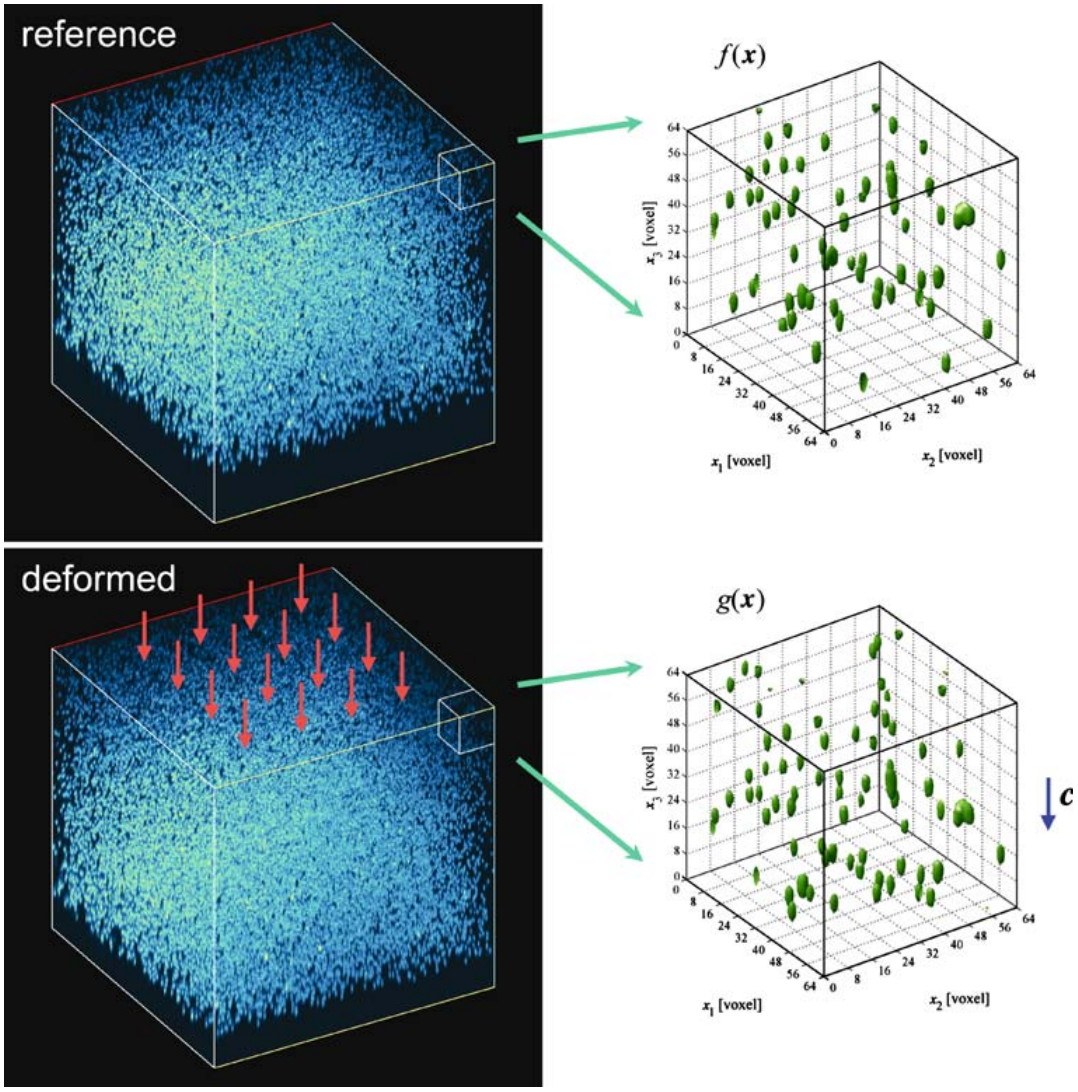

Figure 2.5: Schematic illustration of the principle of digital volume correlation (DVC)

$$m(\hat{\mathbf{y}}) = \int f(\mathbf{x}) g(\mathbf{y}(\mathbf{x}) d\Omega_x. \tag{2.6}$$

The methodology is illustrated using a translational volume correlation, which is presented below. The continuous mapping is assumed to be a rigid body translation, $\mathbf{y} = \mathbf{x} + \mathbf{c}$, and the cross-correlation function is represented as a function of a displacement vector $\mathbf{c}$ as

$$m(\mathbf{c}) = \int f(\mathbf{x}) g(\mathbf{x} + \mathbf{c}) d\Omega_x. \tag{2.7}$$

The cross-correlation function can be written using Fourier transforms as

$$m(\mathbf{c}) = \mathscr{F}^{-1}[\mathscr{F}[f(\mathbf{x})]^{*}\mathscr{F}[g(\mathbf{x})]], \tag{2.8}$$

where the Fourier transform of $f(\mathbf{x})$ is defined as

$$\mathscr{F}[f(\mathbf{x})] = \int f(\mathbf{x})e^{-ik\cdot\mathbf{x}}d\Omega_x, \tag{2.9}$$

and * denotes the complex conjugate. The discrete cross-correlation function can be computed efficiently by using the fast Fourier transform (FFT) algorithm. Then, the rigid body translation vector $\mathbf{c}$ can be estimated from the location of the cross-correlation peak with respect to the origin. Finding the displacement vector $\mathbf{c}$ from the discrete cross-correlation function is straightforward and provides half-voxel accuracy. Determining the displacement vector $\mathbf{c}$ within subvoxel accuracy generally requires fitting and interpolation of the correlation function near the peak. Various fitting models have been used in the past [9, 48], employing somewhat arbitrary assumptions that the cross-correlation function near the peak can be approximated by a Gaussian or a parabolic function. The subvoxel accuracy of such peak-finding algorithms is determined by the choice of fitting function as well as the size of the fitting window. In this study, a three-dimensional quadratic polynomial fitting is used to fit the correlation function near the peak and hence provides improved subvoxel accuracy over previously used lower order fitting polynomials.

Significant measurement error can be introduced from the decorrelation of the intensity patterns when the rotation or the stretch of the subvolume is large. Thus, applications of such simple correlation algorithms have been limited to small strain and small rotation problems due to the inherent limitation of the rigid-translation assumption. In general, the applicability of such an algorithm is limited up to about 5% of strain or 0.05 radian of rotation [9]. To overcome this limitation and to obtain more accurate displacement measurements, a higher order approximation of the deformation field within each subvolume is required for large deformation measurements in soft materials. In the following section, an extension of the FFT-based DVC to measure large

deformation fields is presented.

2.2.2 Stretch Correlation Algorithm

Assuming a general homogeneous deformation of each subvolume, the deformation field can be written as

$$\hat{\mathbf{y}}(\mathbf{x}) = \mathbf{F}\mathbf{x} + \mathbf{c}, \tag{2.10}$$

with a deformation gradient tensor $\mathbf{F} = \mathbf{I} + \nabla\mathbf{u}$ and a displacement vector $\mathbf{u}$. Therefore, any uniform deformation in three-dimensions can be represented with a total of 12 parameters which consist of three displacement components and nine displacement gradient components. Optimal programming in three-dimensions for a total of 12 degrees of freedom (DOF) is computationally expensive in conventional correlation algorithms. Alternatively, the general homogeneous deformation can be represented using a polar decomposition of the deformation gradient tensor as

$$\hat{\mathbf{y}}(\mathbf{x}) = \mathbf{R}\mathbf{U}\mathbf{x} + \mathbf{c}, \tag{2.11}$$

where $\mathbf{R}$ is the orthogonal rotation tensor and $\mathbf{U}$ is the symmetric right-stretch tensor. Then, the general homogeneous deformation in three dimensions is represented with six stretch, three rotation, and three translation components. Depending on the dominant mode of the deformation of interest, the correlation algorithm can be modified to include additional optimization parameters selectively. A digital volume correlation algorithm that includes three rotational degrees of freedom has been presented previously [46]. In this study, assuming small rotations and small shear stretch components, three normal stretch components are included as additional correlation parameters in the FFT-based DVC algorithm, as an extension of the stretch-correlation algorithm developed for large deformation measurements in two dimensions [22]. Neglecting the small rotations, the mapping of a pure homogeneous deformation and a rigid translation is written as

$$\hat{\mathbf{y}}(\mathbf{x}) = \mathbf{U}\mathbf{x} + \mathbf{c}. \tag{2.12}$$

When the loading axes are aligned with the global coordinate axes so that the shear stretch components are small, the invariant condition can be written as

$$f(\mathbf{x}) \approx g(\overline{\mathbf{U}}\mathbf{x} + \mathbf{c}), \tag{2.13}$$

where $\overline{\mathbf{U}}$ denotes the diagonal part of $\mathbf{U}$. Then, the six optimization parameters for the stretch correlation in DVC algorithm are $\{c_1, c_2, c_3, U_{11}, U_{22}, U_{33}\}$. In the case of a pure stretch problem without any translation, a simple coordinate transform into a logarithmic scale converts the stretch correlation problem into a simple translational correlation problem. However, when there is a non-zero translation, the coordinate transform cannot be directly performed in the spatial-domain to achieve the stretch correlation. Therefore, an equivalent invariant condition of Eq. (2.13) in the Fourier domain is considered to implement the stretch correlation in the Fourier domain as

$$||\overline{\mathbf{U}}||\mathscr{F}(\overline{\mathbf{U}}\mathbf{k}) = e^{i\mathbf{k}\cdot\mathbf{c}}\mathscr{G}(\mathbf{k}), \tag{2.14}$$

where, again, $\mathscr{F}(\mathbf{k})$ and $\mathscr{G}(\mathbf{k})$ represent Fourier transforms of $f(\mathbf{x})$ and $g(\mathbf{x})$, respectively. Then by using the Fourier power spectrums only and therefore dropping the phase term, a translation-invariant stretch-correlation problem can be achieved in the Fourier domain. A stretch cross-correlation function to be maximized for determining the three axial stretch components neglecting the determinant of the Jacobian is shown as

$$m(\overline{\mathbf{U}}) = \int |\mathscr{F}(\overline{\mathbf{U}}\mathbf{k})||\mathscr{G}(\mathbf{k})| d\Omega_x. \tag{2.15}$$

The stretch correlation problem in the Fourier domain can be transformed into a translational correlation problem in a log-frequency domain as

$$\widetilde{m}(\boldsymbol{\eta}) = \int |\widetilde{\mathscr{F}}(\boldsymbol{\xi} + \boldsymbol{\eta})||\widetilde{\mathscr{G}}(\boldsymbol{\xi}) d\Omega_\xi, \tag{2.16}$$

where $\boldsymbol{\xi} = log_b \mathbf{k}$, $\boldsymbol{\eta} = log_b \overline{\mathbf{U}}$, and b is an arbitrarily chosen logarithmic base. The translational correlation problem in the log-frequency domain can be easily solved using Eq. 2.8. Finally, the three axial stretch components can be obtained from the optimal vector $\boldsymbol{\eta}$ in the log-frequency domain as

$$U_{11} = b^{\eta_1}, \quad U_{22} = b^{\eta_2} \quad and \quad U_{33} = b^{\eta_3}. \tag{2.17}$$

The accuracy of the obtained stretch components depends strongly on the spectral content of the original signals. If the signals are already band-limited, special considerations, such as normalizing the power spectrums and employing the Hanning window, must be included to achieve robust stretch correlations. Also, in the numerical implementation of the stretch correlation algorithm, incorporating zero-padding of the signals before Fourier transforms can improve the overall accuracy of the stretch correlation algorithm by providing ideal interpolations of the Fourier transforms at a cost of increased computational load.

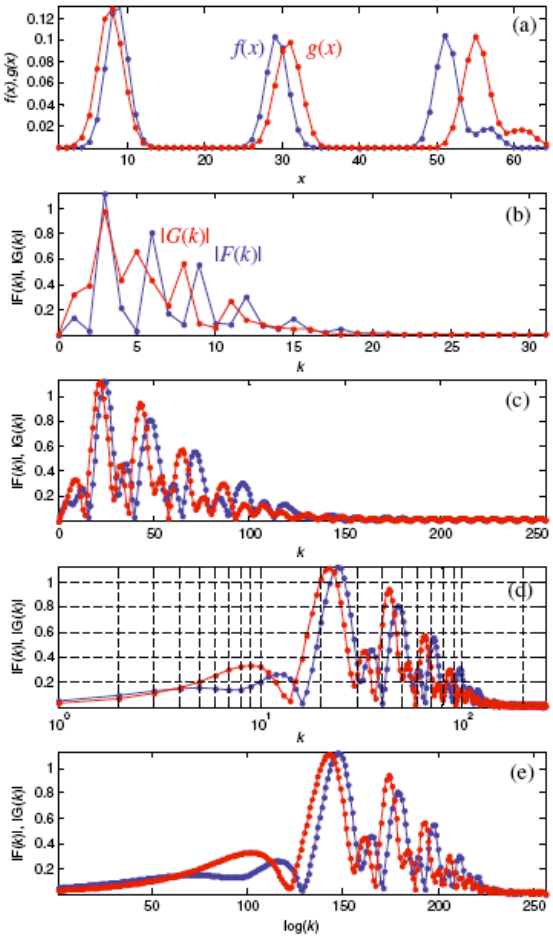

Figure 2.6: Illustration of the stretch-correlation procedures using a one-dimensional (1D) example

In Fig. 2.6, the stretch-correlation procedures are illustrated for a one-dimensional example. Two reference and deformed signals representing 10% of uniform strain are shown in Fig. 2.6 (a). The Fourier power spectra of the two signals are shown in Fig. 2.6 (b). Note that only half of the full frequency range is shown due to the inherent Fourier symmetry. In Fig. 2.6 (c), the equivalent Fourier power spectra are shown after applying zero-padding (interpolation) to the power spectra in Fig. 2.6 (b). Figure 2.6 (d) shows the Fourier power spectra along the logarithmic axis. After interpolating the power spectra using a uniform interval

in the log-frequency domain as shown in Fig. 2.6 (e), the translational correlation as presented in Eq. 2.16 can be applied to find the one-dimensional stretch value. Extension of the one-dimensional stretch-correlation into two dimensions or three dimensions is straightforward as long as the rotations and shear stretches are small.

In the implementation of three-dimensional stretch correlation, two-dimensional projections of the three-dimensional subvolume images were used to circumvent the geometrically increased computational load after the zero-padding, as shown in Fig. 2.7. Essentially, the stretch correlations using the large zero-padding were conducted in a reduced dimension for computational efficiency. Three separate two-dimensional projections were made so that three sets of two stretch components could be obtained. From the six stretch values, three stretch components (U_{11}, U_{22}, U_{33}) were obtained by computing the average of the two corresponding stretch components. Once the three axial stretch components are found, the translation vector $\mathbf{c}$ can be determined more accurately by conducting the stretch-compensated translational correlation using

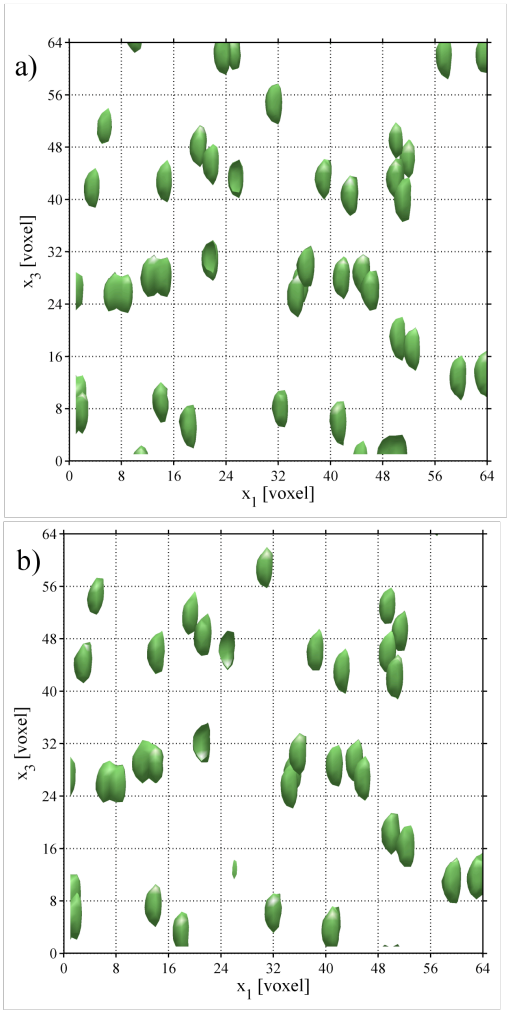

Figure 2.7: Two-dimensional projection of confocal subvolume images (a) before and (b) after uniaxial compression of 10% in x_3-direction

$$m(\mathbf{c}) = \int \widetilde{f}(\boldsymbol{x}')g(\boldsymbol{x}' + \mathbf{c})d\Omega_x, \qquad (2.18)$$

where $f(\mathbf{x}) = \widetilde{f}(\overline{\mathbf{U}}\mathbf{x})$ and $\boldsymbol{x}' = \overline{\mathbf{U}}\mathbf{x}$. The stretch-compensated translational correlation requires the initial subvolume image $f(\mathbf{x})$ to be stretched to $\widetilde{f}(\boldsymbol{x}')$ using the three stretch values obtained earlier. Therefore, the process involves sub-voxel interpolations of the initial subvolume image. Because

the stretch part of the deformation is compensated, a more accurate translation vector **c** can be obtained. The stretch correlation and the translational correlation were conducted iteratively to achieve converged results. For all experiments executing the stretch and translational correlation twice yielded sufficient convergence based on a mean difference criterion, where the mean and standard deviation of the difference of the before and after displacement matrices were compared (this is similar to the least-square error estimate). Such an iteration process is equivalent to the iterative optimization of a correlation coefficient in conventional image correlation scheme conducted in the two-dimensional spatial domain.

Finally, the displacement gradients were computed by using a three-dimensional least-square fitting of each displacement component in a 3 x 3 x 3 grid of neighboring data points. Although a more sophisticated smoothing or filtering algorithm can be employed before or during the gradient calculation to obtain smoother strain fields, no such algorithm was used in this study to assess the performance and robustness of the proposed DVC algorithm. Once the displacement gradient fields are determined, either infinitesimal or finite strain values can be computed from the displacement gradient fields.

2.3 Experimental Procedures

Agarose test specimens were prepared from a 1% weight-in-volume (w/v) solution of agarose (J.T. Baker, NJ) in standard 0.5X TBE buffer (Tris/Borate/EDTA, pH 8.0). The agarose solution was heated until molten, and carboxylate-modified red fluorescent (580/605) polystyrene microspheres (Invitrogen, CA) of 1 μm diameter were injected into the liquid agarose. The nominal volume fraction of fluorescent markers in the gel was 0.3%. The mixture was cast into a pre-chilled Teflon mold mounted onto a glass plate. Samples were left at room temperature for 5 minutes to solidify.

This protocol yielded circular agarose specimens with typical dimensions of 6.4 mm diameter and 1.4 mm height. The addition of the fluorescent microspheres had negligible effect on both the local and global mechanical response of the agarose gel. For spherical inclusion measurements describing a hard inclusion surrounded by a soft matrix, spherical polymethylmethacrylate (PMMA) beads

(Sigma-Aldrich, MO) of 100 μm diameter were added to the mixture before casting. For spherical inclusion measurements describing a soft inclusion of a hard matrix, a burst of air was injected into the molten agarose gel to allow the formation of voids inside the material. The air inclusions (bubbles) were consequently imaged and a particular isolated bubble (only bubble within entire field of view) with a diameter of 200 μm was chosen.

To apply uniaxial compressive loading to the sample while imaging, a miniature loading-fixture was built and mounted directly on the microscope stage of an inverted optical microscope as shown in Fig. 2.8. The sample was kept immersed in the buffer solution to prevent swelling or shrinking during the test. The compressive loading was achieved by translating a micrometer head with a resolution of 1 μm. For all experiments the imposed strain increments were controlled by the micrometer (Mc Master-Carr, Los Angeles, CA) and were calculated using the dimension of the specimen and the imposed loading (displacement) step. The resulting applied force was measured using a 10-gram load cell (A.L. Design, NY). Nominal stress-strain curves were compiled using this setup for each test. The LSCM used in this study was a confocal system (Nikon C-1) combined with an inverted optical microscope (Nikon TE-2000-U). A 40x CFI planar fluor air objective with a numerical aperture of 0.6 was used in all experiments. All DVC computations were performed using Matlab (Mathworks, Natick, MA), and executed on an Intel based Pentium Xeon with 4 core processors. The typical computation time for 512 x 512 x 512 voxel image with a spatial resolution of 8 voxels is $\sim$ 4.3 hours/image.

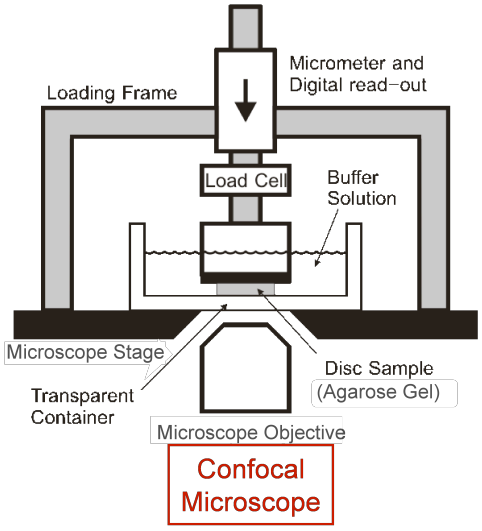

Figure 2.8: Loading fixture for uniaxial compression of soft materials mounted onto a laser scanning confocal microscope

	Stationary	Translation
u_1 [voxel]	0.0605	0.1392
u_2 [voxel]	0.0541	0.1238
u_3 [voxel]	0.2106	0.6491
ϵ_{11} (%)	6.39 x 10^{-3}	4.18 x 10^{-2}
ϵ_{22} (%)	9.80 x 10^{-3}	4.96 x 10^{-2}
ϵ_{33} (%)	0.260	0.718

Table 2.1: Standard deviation values for measured displacement and strain fields in the undeformed condition

2.4 Uniaxial Compression Results

To verify the measurement precision of the DVC algorithm using confocal volume images, two tests were conducted under zero-strain condition. In the first test, two confocal volume images were repeatedly acquired from a stationary sample under zero load. The scanning resolution was 512 x 512 x 512 voxels, and the scan spacing was 0.45 μm in all three directions. This resulted in a field of view of 230 x 230 x 230 μm^3. In the second test, confocal images were acquired before and after translating the unloaded sample using the x_3-directional scanning stage of the confocal microscope. The two pairs of the confocal images were analyzed by using the DVC algorithm with a subvolume size of 64 x 64 x 64 voxels. Displacements were measured at 15 x 15 x 15 points (total 3375 points) in a uniform grid of 32 voxels spacing. Displacement gradients were then calculated by using the displacement data at 3 x 3 x 3 neighboring grid points following linear least-square fitting of the displacement components. Although the quadratic (Lagrangian) or the logarithmic (true) strain measure can be used for large deformation analysis, the linear (engineering) strain measure was used to represent the deformations in this study. As a quantitative measure of the uncertainties in the DVC results, standard deviation values of three displacement components and three normal strain components were computed and are summarized in Table 2.1.

The absolute values of the uncertainties in the displacements and the strains are comparable to previously reported results [4, 39]. These measurement uncertainties are likely due to the noise in the confocal images caused by the photomultiplier tube detector noise as well as the positional uncertainty of the laser scanning system. It is also noted that the axial uncertainties of the displacement

and strain components in the x_3-direction (axial) are approximately three to five times larger than the corresponding lateral uncertainties in the x_1- and x_2-directions (in-plane). This result shows that the axially elongated three-dimensional point spread function causes a significantly degraded measurement precision in the x_3-direction. These tests under zero-strain condition provide a simple way to assess baseline uncertainties of the measurements using the DVC algorithm.

In order to verify the three-dimensional deformation measurement capability of the DVC using the LSCM, the agarose gel sample was compressed uniaxially with nominal strain increments of 2-3%. The total imposed nominal strain was approximately 10%. The obtained confocal images were analyzed using the DVC algorithm with a subvolume size of 64 x 64 x 64 voxels. Figure 2.10 shows a vector plot of the measured displacement field and Fig. 2.9 shows a three-dimensional contour plot of the vertical displacement components.

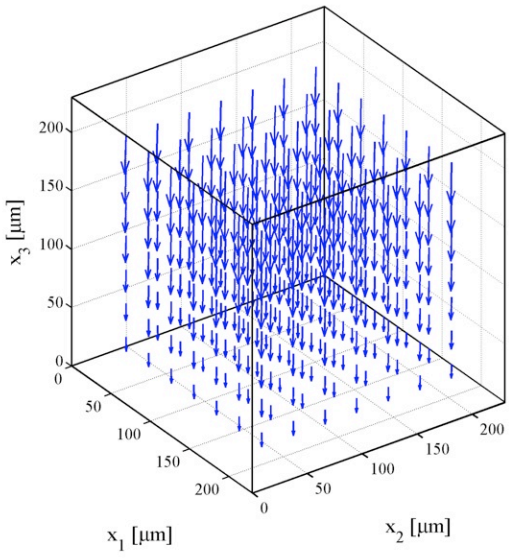

Figure 2.9: Experimentally determined three-dimensional displacement vector field under uniaxial compression

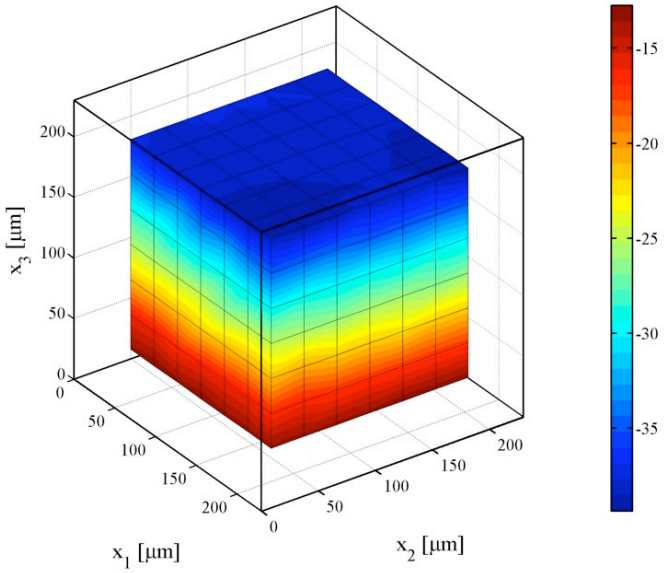

Figure 2.10: Experimentally determined vertical displacement field u_3 under uniaxial compression

In order to assess the performance of the DVC algorithm with the stretch-correlation for large deformation measurements, accuracy and precision must be established systematically. The accuracy and the precision of a measurement technique are usually achieved by repeatedly measuring some traceable reference standard. Then, the accuracy and precision are typically quantified as

	No stretch-correlation		Stretch-correlation	
	Mean	Std. Deviation	Mean	Std. Deviation
ϵ_{11} (%)	0.8 x 10^{-2}	7.1 x 10^{-2}	-3.6 x 10^{-2}	7.4 x 10^{-2}
ϵ_{22} (%)	1.1 x 10^{-2}	6.8 x 10^{-2}	7.8 x 10^{-2}	7.1 x 10^{-2}
ϵ_{33} (%)	-9.25	0.866	-9.34	0.392

Table 2.2: Mean and standard deviation values for measured strain fields under uniaxial compression

the difference between the mean of the measured values and the true value, and by the standard deviation of the measured values, respectively.

Mean and standard deviation values of the measured strain fields are presented in Table 2.2 to assess the effectiveness of the stretch-correlation algorithm. The mean values of the lateral strain components ϵ_{11} and ϵ_{22} are close to zero and smaller than their corresponding standard deviation values, i.e., the measurement precision, and are therefore negligible. The standard deviations of the no-stretch-correlated and stretch-correlated lateral strain components are similar, illustrating that the stretch-correlation does not improve the precision of the strain measurements for small strains. Comparing the no-stretch and stretch-corrected axial strain component ϵ_{33}, the difference of 0.09% between the two mean values is smaller than their corresponding standard deviations, which shows that the stretch correlation does not improve the accuracy of the average strain measurement. However, the standard deviation in the stretch-correlation case is less than half of that in the no-stretch-correlation case. This proves that the stretch-correlation greatly improves the precision of the large deformation measurement. Although precise measurements do not necessarily mean accurate measurements, it is often not possible to reliably achieve high accuracy in individual measurements without precision. This point is particularly important in the full-field measurement of non-uniform deformation fields.

Since it is not possible to know the true value of the compressive strain up to the level of accuracy and precision of the measurement technique under investigation, the absolute accuracy of the proposed DVC method cannot be assessed with the nominal strain value from the global measurement. However, it is clear that the overall measurement accuracy can be improved by providing better precision, since precision is a limit of accuracy. The results from the uniaxial compression test show

that the proposed stretch-correlation algorithm in conjunction with the deconvolution algorithm improved the overall accuracy of large deformation measurement with better precision.

The average axial compressive strain was 9.3%, whereas the average lateral strain values were negligible. This result showed that the lateral expansion due to the Poisson effect was effectively constrained due to the disc-shaped geometry of the sample. To determine the material properties of the agarose sample correctly the uniaxial test results need to be interpreted as a constrained compression ($\epsilon_{11} = \epsilon_{22} = 0$) of a soft layer. The axial stress-strain ratio for constrained compression is defined as a constrained modulus ($\overline{E}$) and related to elastic properties as

$$\overline{E} = \frac{\sigma_{33}}{\epsilon_{33}} = \frac{(1-\nu)E}{(1+\nu)(1-2\nu)}, \tag{2.19}$$

where E and ν denote the Young's modulus and the Poisson's ratio, respectively.

2.5 Spherical Inclusion Results

In order to demonstrate the capability of the measurement technique using the DVC and the LSCM, non-uniform three-dimensional deformation fields near a hard and a soft (void) spherical inclusion were measured under far-field uniaxial compressive loading. Confocal images near a 100 μm-diameter PMMA bead and a 200 μm air bubble embedded within the agarose gel sample were recorded during incremental compressive loading. The experimental setup is shown in Fig. 2.11 schematically. The nominal strain increment was approximately 3%. The scanning resolution was 512 x 512 x 512 voxels, and the scan spacing was 0.45 μm

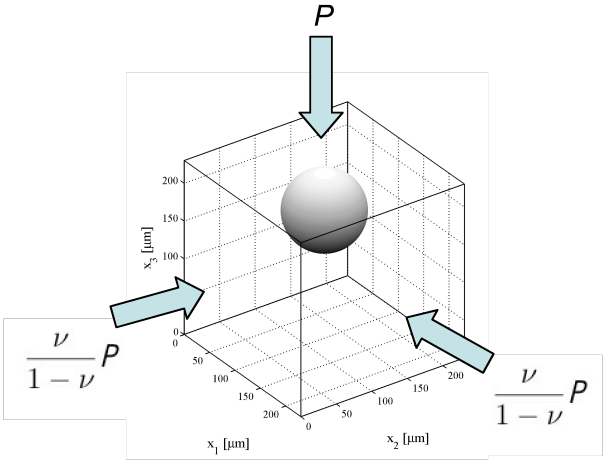

Figure 2.11: Schematic of a spherical inclusion with a sliding interface under confined uniaxial compression

in all three directions. The experimentally determined displacement fields were qualitatively and quantitatively compared to the analytical solution given by Ghahremani [18] and is presented in the next section. The solution by Ghahremani describes a spherical "sliding" inclusion, where the "sliding" is defined by vanishing tractions along the inclusion-matrix interface and continuity in the displacements normal to the inclusion-matrix interface.

2.5.1 Analytical Solution of a Sliding Spherical Inclusion

This section presents the analytical solution of a sliding spherical inclusion in a linearly elastic matrix under applied far field uniaxial compressive loading as formulated by Ghahremani [18] . Most analytical elasticity solutions of the inclusion problem assume the continuity of displacement at the interface. Considering the high water content in the agarose gel and the large deformations in the sample, the perfect bonding condition is inadequate to accurately represent the present experiment. Using the solution of the sliding inclusion problem under uniaxial loading, and considering that only the deformations inside the agarose gel and not the inclusion itself are measured, the elasticity solution of the matrix displacements beginning with the far field solution due to an applied uniform compressive loading stress P is

$$u_\infty = \frac{P}{2G_m(1+\nu_m)}(\nu x_1 \mathbf{i} + \nu x_2 \mathbf{j} - x_3 \mathbf{k}), \tag{2.20}$$

where G_m and ν_m denote the shear modulus and Poisson's ratio of the matrix, respectively, and $\mathbf{i}$, $\mathbf{j}$, $\mathbf{k}$ are the Cartesian unit vectors. The radial displacements due to the inclusions are

$$u_r(r,\theta) = -\frac{A}{r^2} + [\frac{B(5-4\nu_m)}{r^2} - \frac{3C}{2r^4}](3cos^2\theta - 1), \tag{2.21}$$

with $r = \sqrt{x_1^2 + x_2^2 + x_3^2}$, and $\theta = tan^{-1}(x_3/\sqrt{x_1^2 + x_2^2})$, and constants A, B, and C as described later. The tangential displacements due to the inclusion are

$$u_\theta(r,\theta) = -[\frac{B(1-2\nu_m)}{r^2} + \frac{C}{2r^4}](sin2\theta). \tag{2.22}$$

The constants A, B, and C are defined as

$$A = \frac{Pr_0^3}{12G_m} - \frac{Dr_0^3(1+\nu_i)G_i}{G_m}, \tag{2.23}$$

$$B = -\frac{5P}{12G_m} \cdot \frac{r_0^3}{7-5\nu_m} + \frac{G_i}{G_m} \cdot \frac{7+5\nu_i}{7-5\nu_m} F r_0^5, \tag{2.24}$$

$$C = -\frac{P}{2G_m} \cdot \frac{r_0^5}{7-5\nu_m} + \frac{G_i}{2G_m} - \frac{1+\nu_m}{7-5\nu_m}(7+5\nu_i) F r_0^7, \tag{2.25}$$

where G_i and ν_i denote the shear modulus and Poisson's ratio of the inclusion, respectively, r_0 is the inclusion diameter, and the constants D and F are given by

$$D = \frac{P(1-\nu_m)}{4(1+\nu_m)[(2G_m+G_i)+\nu_i(G_i-4G_m)]}, \tag{2.26}$$

$$F = \frac{-10P(1-\nu_m)}{r_0^2[4G_m(7-5\nu_m)(4\nu_i-7)-G_i(17-19\nu_m)(7+5\nu_i)]}. \tag{2.27}$$

The final form of the analytical solution of the sliding inclusion under the laterally-constrained uniaxial compressive loading is constructed by the superposition of three mutually-orthogonal uniaxial compression solutions using Eqs. (2.20-2.27) as illustrated in Fig. 2.11.

2.5.2 PMMA Bead and Air Bubble Inclusion Results

This section presents the experimentally determined full-field three-dimensional displacements near a hard (PMMA) and soft (air bubble) inclusion. Confocal images of each embedded inclusion were recorded during successive compressive loading increments. The nominal strain increment was approximately 3%. The scanning resolution was 512 x 512 x 512 voxels as before, and the scan spacing was 0.45 μm in all three directions. A representative confocal scanning volume near the inclusion is illustrated schematically in Fig. 2.11. Figures 2.12 and 2.13 show a vertical slice of the confocal image along the meridian plane of the PMMA bead and the air bubble at the undeformed

configuration, respectively. The superimposed uniform grid with spacing increments of 16 voxels represents the locations where displacements measurements were conducted. The confocal images were analyzed by using the proposed DVC algorithm with a subvolume size of 64 x 64 x 64 voxels. The spatial resolution of the DVC technique can be adjusted and increased to a maximum resolution of 1 voxel. However, due to the increased computational load with increased resolution, the typical spatial resolution for calculating the displacement is 8 voxels, or 3.6 μm.

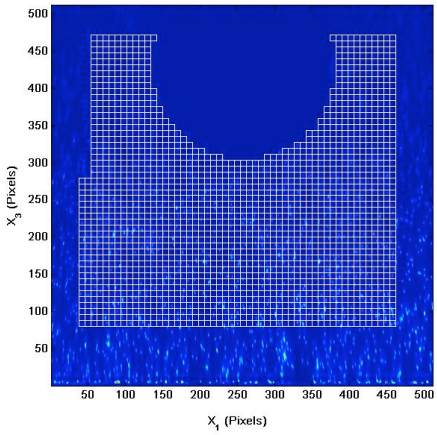

Figure 2.12: Confocal slice along the meridian plane of an embedded 100 μm PMMA bead within an agarose sample

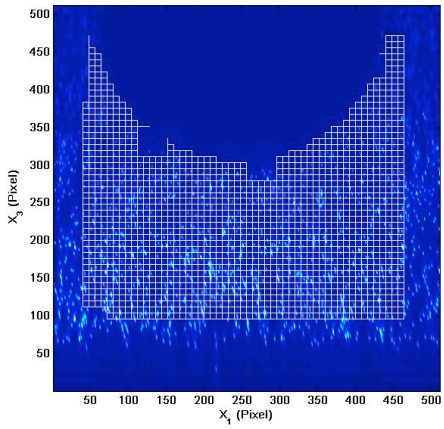

Figure 2.13: Confocal slice along the meridian plane of an embedded 200 μm air bubble within an agarose sample

Initially, the displacement fields are calculated using the translational DVC algorithm, the output of which is then used as an initial guess in calculating the displacement fields using the stretch-correlation algorithm. Figures 2.14 and 2.15 show a representative cross-sectional three-dimensional contour plot of the u_3 displacement fields near the PMMA bead and air bubble inclusion. Figures 2.16 and 2.17 show the results of the DVC stretch-correlation algorithm for the same experimental data on a smaller data domain (around the center plane of each inclusion). Since the stretch-correlation algorithm is computationally more expensive than the regular translational DVC algorithm, only a particular region of interest, which here is a volumetric region around the center plane of each inclusion, is selected. In order to compare the experimental data with the analytical elasticity solution presented in the previous section, the data set is refined further by selecting and executing the DVC stretch-correlation on the meridian plane of each inclusion. The voxel spacing or spatial

resolution of the DVC measured displacement field is further increased to a grid spacing of 4 voxels. Generally such an increase in resolution is only performed on thin volumes consisting of less than 10 slices to be computationally efficient.

The contour maps in Figs. 2.18 and 2.19 represent constant contours of the vertical (u_3) displacement components on the meridian plane of the PMMA and air bubble inclusion, respectively. The local distortion of the displacement contours near the PMMA bead and the air bubble indicate that the proposed DVC algorithm effectively captures non-uniform deformation fields near both spherical inclusions. It should be noted that the magnitude of the u_3 displacements as indicated in pixels by the color bar in both Figs. are different. This difference is due to rigid body translation during the experiments that is also captured by the DVC algorithm. This rigid body motion arises since the imaging reference frame is stationary and the inclusion location within the agarose gel is different for the two inclusions. Hence, the amount of recorded rigid body translation will be different. The rigid body translation is accounted for in the analytical model through the simple addition of a displacement constant. The experimentally measured displacement fields in Figs. 2.18 and 2.19 were compared to the analytical solution of the equivalent linear-elasticity problem as described in detail in the previous section.

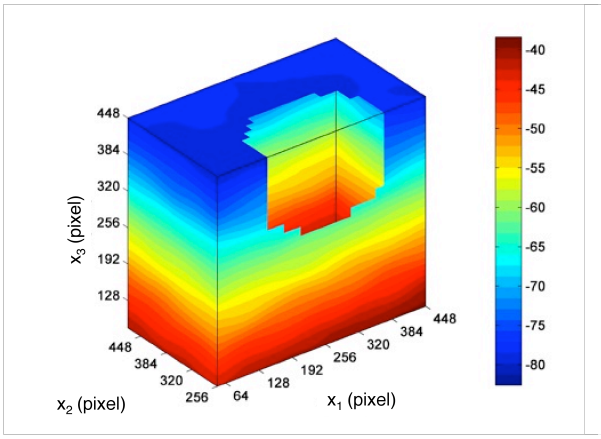

Figure 2.14: Cross-section of the experimentally determined vertical displacement field u_3 near PMMA bead inclusion under uniaxial compression. Contour values are in pixels (1 pixel = 0.45 µm).

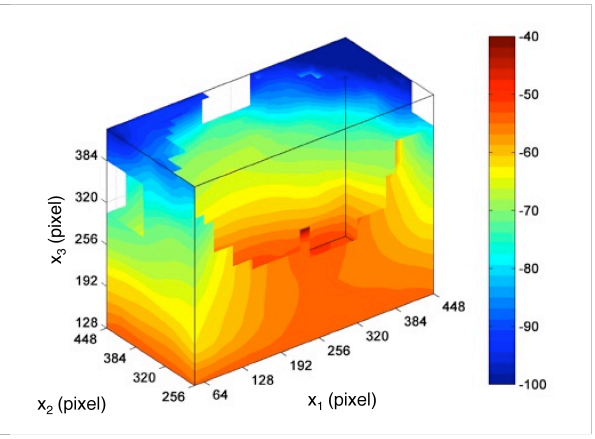

Figure 2.15: Cross-section of the experimentally determined vertical displacement field u_3 near air bubble inclusion under uniaxial compression. Contour values are in pixels (1 pixel = 0.45 µm).

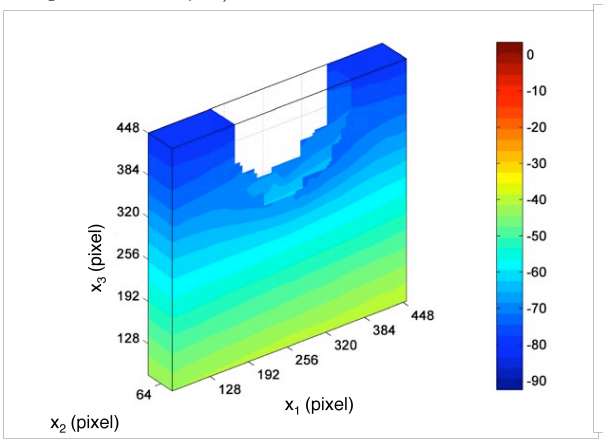

Figure 2.16: Cross-section of the stretch-corrected measured vertical displacement field u_3 near the PMMA bead inclusion under uniaxial compression. Contour values are in pixels (1 pixel = 0.45 µm).

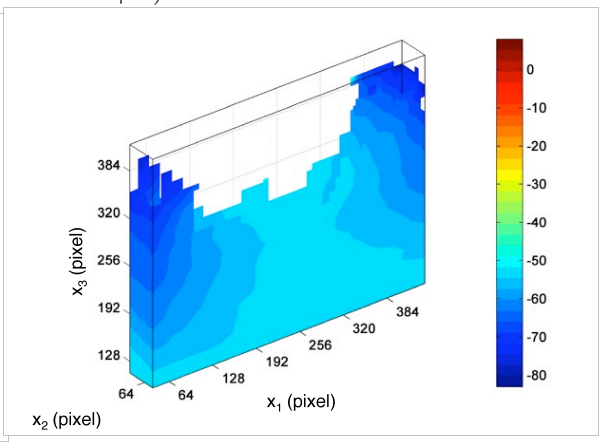

Figure 2.17: Cross-section of the stretch-corrected measured vertical displacement field u_3 near the air bubble inclusion under uniaxial compression. Contour values are in pixels (1 pixel = 0.45 µm).

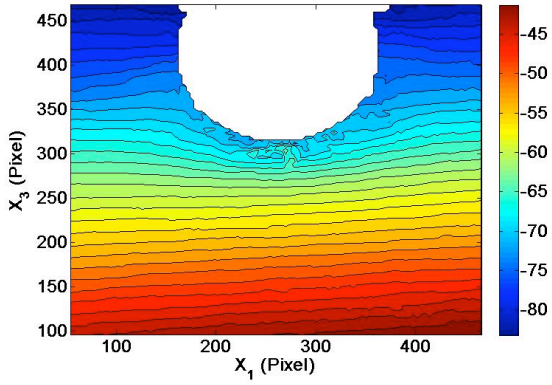

Figure 2.18: Experimentally determined vertical displacement field u_3 near PMMA bead inclusion under uniaxial compression. Contour values are in pixels (1 pixel = 0.45 μm).

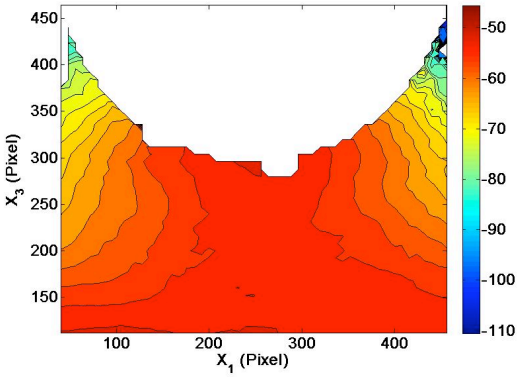

Figure 2.19: Experimentally determined vertical displacement field u_3 near air bubble inclusion under uniaxial compression. Contour values are in pixels (1 pixel = 0.45 μm).

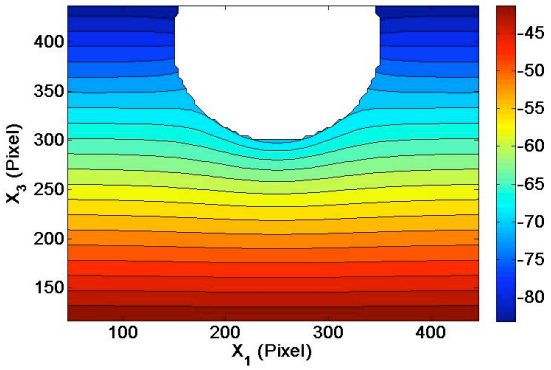

Figure 2.20: Analytical vertical displacement field u_3 near a rigid bead inclusion with a sliding interface under uniaxial constrained compression. Contour values are in pixels (1 pixel = 0.45 μm).

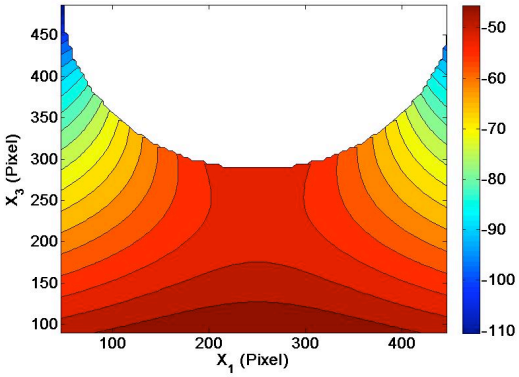

Figure 2.21: Analytical vertical displacement field u_3 near a soft inclusion with a sliding interface under uniaxial constrained compression. Contour values are in pixels (1 pixel = 0.45 μm).

The contour maps in Fig. 2.20 and Fig. 2.21 show the horizontal and the vertical displacement fields of the constructed analytical solution. Qualitative comparisons of the contour maps in Fig. 2.18 and Fig. 2.20, and Fig. 2.19 and Fig. 2.21 indicate that the proposed DVC algorithm is well-suited for the full-field measurements of non-uniform deformation fields in three dimensions. Once the full field displacements are obtained, the strain tensor is calculated by using a displacement-gradient technique [26]. In brief, the local displacement field around each grid point is approximated by

$$\hat{\mathbf{u}}(x_1, x_2, x_3) = ax_1 + bx_2 + cx_3 + d, \tag{2.28}$$

where a,b,c, and d are constants to be determined by minimizing the following vector $\mathbf{S}$ in the least-square sense using the measured displacement vector $\mathbf{u}$

$$\mathbf{S} = \sum_{i=1}^{N}\sum_{j=1}^{M}\sum_{k=1}^{P}(\hat{u}_{ijk} - u_{ijk})^2. \tag{2.29}$$

Point-wise least-square minimization of Eqs. 2.28 and 2.29 using a 3 x 3 x 3 voxel stencil or kernel, yields the constants a,b,c and d from which the full-field strain tensor is constructed. A more detailed description of the displacement-gradient technique can be found in [26]. Figures 2.22 and 2.23 show a contour plot of ϵ_{33} from the experimentally obtained displacement fields around the PMMA and air bubble inclusions, respectively.

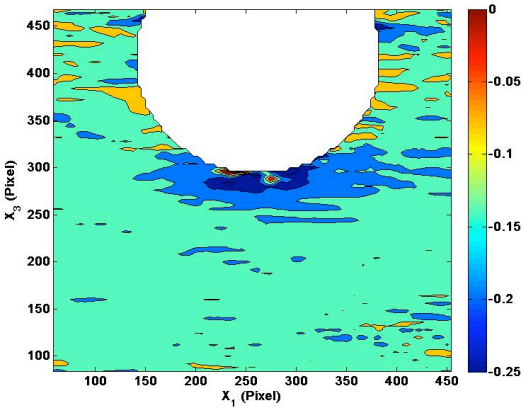

Figure 2.22: Experimentally determined vertical strain field ϵ_{33} near a PMMA bead inclusion under uniaxial compression

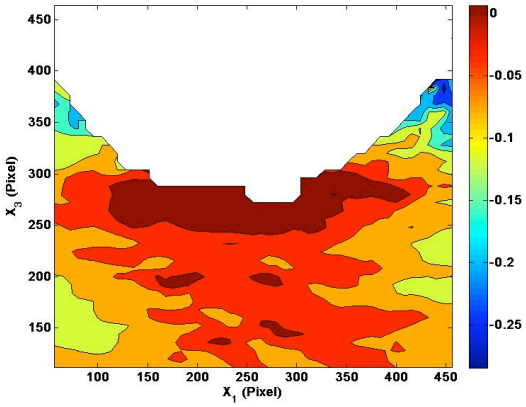

Figure 2.23: Experimentally determined vertical strain field ϵ_{33} near an air bubble inclusion under uniaxial compression

At the bottom of the inclusion in Fig. 2.22, a region of high strain concentration of up to 25% strain, or 2.5 times of the far field applied strain is shown. Figure 2.23 displays a similar picture in case of the strain profile near the air bubble, where ϵ_{33} is approximately zero directly beneath the bubble. Following the time-lapse series of the air bubble compression measurements (not shown here), the air bubble collapses under the applied far field strain with no noticeable deformation occurring in the agarose gel underneath the bubble. Figure 2.24 displays the line-profile of the ϵ_{33} strain component along the central axis in the x_3-direction from the PMMA bead inclusion contour plot (Fig. 2.22). Also shown in Fig. 2.24 is the analytical description of ϵ_{33} along the meridian

plane of a hard inclusion as described by Ghahremani [18]. The local compressive strain reaches the far-field applied strain level at approximately one diameter length away from the center of the bead. The high strain gradient will decrease the accuracy of the stretch-correlation by violating the assumption of uniform stretch deformation. In such cases, iterative applications of the DVC using a smaller subvolume will increase the accuracy of the measurements since each subvolume will be subjected to a more uniform stretch.

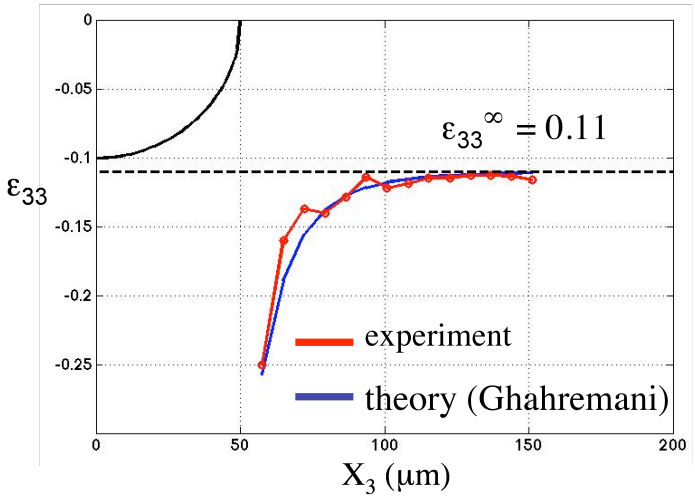

Figure 2.24: Plot of the experimentally determined strain field ϵ_{33} as a function of outward distance ($x_3 = 0$ denotes the center of the inclusion) in the meridian plane of the spherical PMMA inclusion under uniaxial compression

2.6 Summary of LSCM and DVC Development

A novel experimental technique for measuring three-dimensional large deformation fields in soft materials has been developed [17]. The technique utilizes the three-dimensional measurement capability of the DVC algorithm in conjunction with the three-dimensional imaging capability of laser scanning confocal microscopy. Introduction of the stretch-correlation algorithm and the deconvolution algorithm greatly improved the strain measurement accuracy by providing better precision especially under large deformation. Also, the large deformation measurement capability of the proposed DVC algorithm was successfully demonstrated by measuring a uniform deformation field for the case of simple uniaxial compression and a non-uniform deformation field surrounding both a hard and soft

(void) spherical inclusion. This new technique should prove particularly useful in situations where local three-dimensional strain non-uniformities need to be measured with high resolution. An application of this technique in characterizing the three-dimensional time-dependent cell interactions with its surrounding extracellular matrix are documented in the following chapters. While it is anticipated that this technique will lead to valuable insights into the role of mechanical forces on biological processes and mechanical characterization of biological materials in three dimensions, the application of the DVC itself is not limited to usage with LSCM. Since DVC is a post-processing technique, it renders itself as a quantitative full-field displacement measurement technique that can be combined with many methods in experimental mechanics including computer tomography (CT) scanning, magnetic resonance imaging (MRI), and many others.

Chapter 3

Application of LSCM and DVC to Migrating Fibroblasts

This chapter describes the experimental setup of the substrate-cell system that will be studied in Chapter 4. In particular, the experimental procedure to produce polyacrylamide gel samples, cell culturing, mechanical testing of the substrates as well as the LSCM live cell imaging setup are described in detail below.

3.1 Experimental Procedure

Polyacrylamide gels are one of the most commonly used polymer-based substrate materials in studying cell force responses due to their mechanical tunability, optical translucency, and elastic material behavior [35]. By controlling the incorporation percentage or volume fraction of added crosslinker N, N-methylene-bis-acrylamide (BIS), the Young's modulus of each particular polyacrylamide gel can be modified with a typical modulus ranging from around 1 - 20 kPa [14, 41, 49]. Polyacrylamide substrates were prepared for all of the results shown in the subsequent chapters.

In order to control the thickness of each polyacrylamide substrate, a polyacrylamide solution of known volume was pipetted onto a clean coverslip. A chemically-activated coverslip was then laid on top of the solution causing the gel mixture to spread uniformly in-between both coverslips. After the polymerization reaction of the polyacrylamide gel was completed, the bottom coverslip was removed, and the polyacrylamide gel was left adherent to the activated bottom coverslip. The following

protocols describe how to chemically activate the coverslips followed by the preparations of the polyacrylamide films, including biological functionalization of the polyacrylamide substrates through fibronectin. Concluding this section is a description of the characterization of the fibronectin-modified polyacrylamide substrates and the employed cell culture.

3.1.1 Preparation of Activated Coverslips

Glass coverslips (Gold-Seal coverslip No. 0, Electron Microscopy Sciences) were chemically modified to allow for covalent attachment of polyacrylamide sheets using a previously established protocol [40, 35]. Briefly, coverslips were rinsed with ethanol and then placed in a sample dish containing a solution of 0.5% (v/v) 3-aminopropyltrimethoxysilane (Gelest) in ethanol for 5 minutes. The coverslips were removed from the dish and rinsed thoroughly with ethanol before being immediately submersed with the treated side facing upwards in a solution of 0.5% glutaraldehyde (Polysciences, Inc.) and water for 30 minutes. Activated coverslips were rinsed thoroughly with deionized water and left to dry for several hours at 60^o C. Treated coverslips were then covered and stored at room temperature for up to one week after the preparation.

3.1.2 Preparation of Polyacrylamide Films

Micron-sized polyacrylamide films were generated and fused to functionalized coverslips using a previously adapted protocol [14, 40]. Two different solutions of polyacrylamide (Bio-Rad, 40% w/v) and N, N-methylene-bis-acrylamide (BIS, Bio-Rad, 2.5% w/v) were mixed with distilled water to obtain substrates with different mechanical properties. The first solution contains a total volume fraction of 10% acrylamide and 0.015% BIS, whereas the second solutions consists of 10% acrylamide and 0.0075% BIS total volume fraction. By adjusting the concentration of BIS in the formulation mechanical properties of the polyacrylamide substrate was modified in a controlled manner. Next, fluorescent micro-particles (0.5 μm in diameter, carboxylate-modified, Molecular Probes) in a 2% (w/v) suspension were vortexed for 10-15 seconds and subsequently added to either polyacrylamide solution in a volume ratio of 9:100. Crosslinking was initiated through the addition of ammonium

persulfate (Sigma) and TEMED (Invitrogen). The samples were vortexed for 10 seconds, and 5-7 microliters of the acrylamide solution was pipetted on the surface of a precleaned microscope slide (No. 1, 22 mm x 50 mm, VWR). To generate thicker films, 20-40 microliters of the solution were used. The activated surface of the coverslip was then placed on top of the acrylamide droplet, causing the solution to flatten under the weight of the coverslip. The entire assembly was set out to allow complete polymerization for 5 minutes, and then placed in a 60 mm Petri dish (VWR) containing distilled water for 10-30 minutes. The bottom coverslip was then peeled off using a pair of tweezers, leaving the polyacrylamide gel bonded to the activated coverslip. The polyacrylamide gel was then thoroughly rinsed with water and hydrated in a 60 mm Petri dish.

The thickness of each sample was measured by vertical slicing of the acquired volumetric confocal images, and calculating the distance from the top layer of fluorescent particles to the bottom layer of fluorescent beads. Sample thicknesses were controlled by adjusting the total volume of acrylamide mixture used.

3.1.3 Functionalization of Polyacrylamide Substrates with Fibronectin (FN)

In order to promote cell attachment to polyacrylamide films, a saturating density of fibronectin was conjugated to the gel surface using the heterobifunctional crosslinker, sulfo-SANPAH (Pierce Chemicals). Adopting a previously outlined procedure [14], polyacrylamide gel samples were briefly dried in air to remove any excess water before 200 µl of sulfo-SANPAH (1.0 mg/ml) were deposited on the surface of the film. The sample was then exposed to unfiltered UV light from a high-pressure mercury lamp (Oriel Q 100W at 5 A, $>$ 10 min warm up time) at a distance of 10 inches away from the sample for 7.5 minutes. The darkened sulfo-SANPAH solution was subsequently removed from the surface of the gel and replaced with another 200 µl aliquot solution of sulfo-SANPAH and irradiated for another 7.5 minutes for a total of 15 minutes of UV exposure. The samples were then rinsed vigorously with water for 5 minutes, and adhered to the bottom of 60 mm Petri dishes (Becton Dickinson) by applying a thin layer of vacuum grease (Dow Corning) around the perimeter

of the unmodified side of the coverslip. The samples were rinsed twice with phosphate buffered saline (pH 7.4), and covered with a solution of fibronectin (FN, 0.2 mg/ml, Millipore) and left undisturbed overnight at 4^o C. Following overnight incubation, the substrates were rinsed three times with a phosphate buffered saline (PBS) solution and sterilized by rinsing with ethanol before use.

3.1.4 Characterization of Fibronectin-Modified Films

A comparison of the relative concentration of covalently attached fibronectin on samples made with varying percentages of crosslinker was conducted using a bicinchoninic acid (BCA) assay (Sigma). In this assay, the relative protein concentration is exhibited as a color change in the sample solution upon the addition of the copper/BCA reagents. The degree of color change can be quantified by measuring the absorbance at 542 nm using a plate reader. A set of fibronectin-modified samples made with varying crosslinker (BIS) percentages (3-4 total samples for each percentage) were prepared as described above, and placed in a 6-well plate. However, fluorescent particles were not added to the polyacrylamide samples in the BCA assays in order to avoid unintentional complications, since the microparticles partially fluoresce at the absorbance wavelength of the plate reader. Negative controls consisting of unmodified samples made with each crosslinker percentage were also prepared. All samples were then treated with the copper/BCA reagent for 1 hour at 60^o C, followed by an absorbance reading. All tests were repeated twice. The absorbance reading for both sets of samples showed similar absorbance values, and lie within the standard deviation calculated from the tested samples. These results confirm that cells are responding to the difference in mechanical properties and not differences in the chemical composition of the surfaces.

3.1.5 Cell Culture

Prior to depositing cells, fibronectin-modified gel samples were equilibrated in a growth medium at 37^o C for 15 minutes. Swiss 3T3 fibroblasts transfected with a green-fluorescent-protein-actin (GFP-actin) vector (from Scott Frasier's laboratory) were cultured in Dulbecco's Modified Eagle Medium (DMEM) supplemented with 10% fetal bovine serum, 50 μg/ml streptomycin, and 50 μg/ml

penicillin. For all experiments, cells were first treated with Mitotracker Deep Red (Invitrogen) for 45 minutes before passaging with trypsin. Mitotracker dyes accumulate in actively respiring mitochondria providing a second method in addition to the GFP-actin vector for tracking the location of cells on the material as well as showing cell viability. Cells were plated at a concentration of $\sim$ 40,000 cells/coverslip, and were incubated on samples for 8-12 hours before imaging.

3.2 Mechanical Testing of the Substrate Material

The mechanical properties of the substrates were determined by performing both unconfined and confined compression testing on cylindrical polyacrylamide specimens using a custom-built compression setup [17]. The typical sample dimensions were 8 mm in diameter and 4 mm in height. The displacements during each compression increment were controlled using a digital micrometer with a resolution of 1 µm. The resulting nominal force was measured using a 10 g load cell (A.L. Design, NY). For each volume fraction of polyacrylamide crosslinker 6-8 samples were tested in both confined and unconfined uniaxial compression.

For unconfined tests, gel samples were cast in a circular washer secured to the bottom of a 60 mm diameter plastic Petri dish. Following polymerization ($\sim$ 2-5 minutes), the washer was removed from the dish and the sample was hydrated and left covered at room temperature overnight to ensure hydrostatic (swelling) equilibrium. Prior to compression, the alignment of the setup with the sample was inspected to ensure pure compression along the nominal loading axis. The samples were compressed between the top platen of the compression setup and the bottom of the Petri dish with a nominal strain increment of 1-2%. Force values were obtained continuously during each 5-minute increment in order to detect any time-dependent relaxation of the material during the compression. The typical total applied compressive strain was $\sim$ 13-15%. After complete loading, the sample was successively unloaded using the same strain increments to record the entire loading-unloading cycle. Figure 3.1 shows the raw data for an incremental loading cycle highlighting negligible time-dependent material behavior, whereas Figure 3.2 shows the loading-unloading stress strain curve for a typical sample.

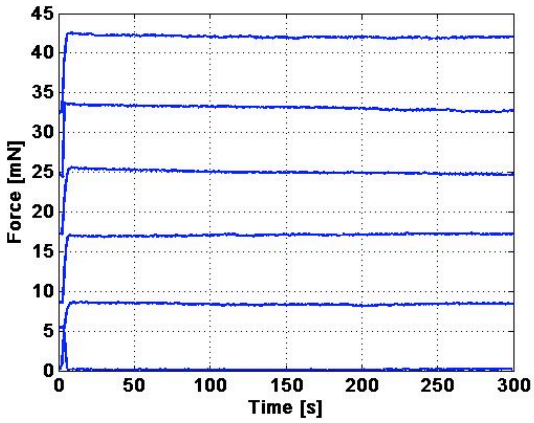

Figure 3.1: Representative force history plot during uniaxial compression experiments on a polyacrylamide gel showing negligible time-dependent material behavior.

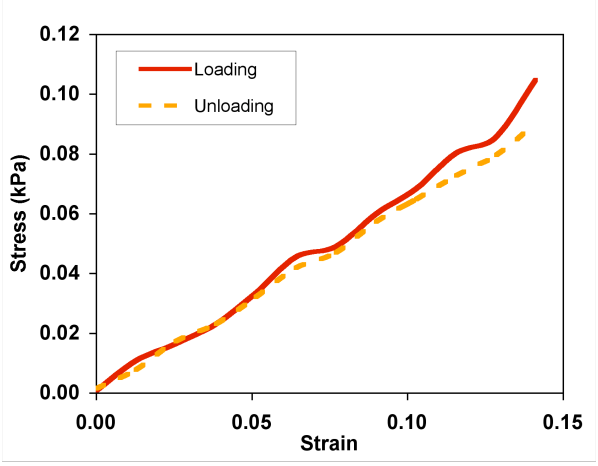

Figure 3.2: Representative loading and unloading stress-strain plot of a polyacrylamide gel, highlighting the linear elastic material response with negligible hysteresis.

The Young's modulus for the polyacrylamide samples was calculated from each stress-strain curve as $E = \sigma_{33}/\epsilon_{33}$ ($\sigma_{11} = \sigma_{22} = 0$), where σ and ϵ denote the uniaxial engineering stress and engineering strain. Table 3.1 summarizes the unconfined compression test results for two different crosslinker volume fractions.

Crosslinker Volume Fraction	Young's Modulus (kPa)
0.015% BIS	9.64 ± 1.12
0.0075% BIS	0.82 ± 0.23

Table 3.1: Young's modulus values for polyacrylamide substrates with different crosslinker volume fraction.

In order to determine the Poisson's ratio for each polyacrylamide gel, cylindrical specimens were cast and polymerized in a confined Teflon sleeve 15 mm in diameter and about 8 mm in height. Samples were hydrated following the same protocol as described above. The samples were compressed following the same loading-unloading protocol used for the unconfined test. Using the determined Young's modulus value of the unconfined test case and observing that further compression beyond an initial compression strain of $\sim 0.25\%$ was not possible (due to the Poisson effect), Poisson's ratio was determined to be $\sim$ 0.48 - 0.5 according to the following equation:

$$\overline{E} = \frac{\sigma_{33}}{\epsilon_{33}} = \frac{(1-\nu)}{(1+\nu)(1-2\nu)}E, \tag{3.1}$$

where $\overline{E}$ denotes the measured confined compression modulus, ν is the Poisson's ratio, and E is the Young's modulus as determined from unconfined compression test. From this set of experiments, Poisson's ratio was taken to be 0.5, and the material behavior is described as a linearly elastic, isotropic, incompressible for all traction calculations.

3.3 Live Cell Imaging

Three-dimensional image stacks were acquired using a Nikon C-1 confocal system mounted on a TE-2000-U inverted optical microscope. A 40x CFI planar fluor air objective with a numerical aperture of 0.6 was used in all experiments. Three laser lines were used to image the cells and the fluorescent microparticles: an argon (488 nm) laser for the GFP-actin, a green helium neon (543 nm) for the microparticles inside the polyacrylamide gels, and a red helium neon (633 nm) illuminating Mitotracker Deep Red for mitochondrial labeling. Confocal stacks were acquired every 35 minutes for several hours at a resolution of 512 x 512 x Z voxels (x_1 x x_2 x x_3), where Z ranges from 120 250 pixels (voxels). Typical imaging areas were between 150-200 μm^2 in-plane (x_1, x_2) with imaged volume depth of $\sim$ 15 - 20 μm. Images with a larger field of view were captured before and after experiments to ensure that measured displacements were not the result of contributions from neighboring cells. Physiological conditions were maintained during all times by housing the entire confocal microscope inside a custom-built temperature-controlled chamber. The temperature was controlled using a feedback controlled heater, Air-Therm ATX Air Heater Controller (World Precision Instruments), and cell media PH-levels were maintained by the addition of arterial gas (5% CO_2, 20% O_2, 75% N_2) into the chamber.

3.4 Establishing LSCM and DVC Resolution for Polyacrylamide Gels

Chapter 2 already presented the resolution of the LSCM-DVC technique, however, all measurements in the development of this technique were performed at room temperature. Here, several zero-load (baseline) measurements were performed on fibronectin-modified polyacrylamide gels for both crosslinker volume fraction levels at 37^o C to establish the maximum resolution of the technique for softer materials at elevated temperatures. Table 3.2 shows representative results of the fibronectin-modified polyacrylamide gels side by side with the earlier presented no-load DVC results from an agarose gel. As can been seen in Table 3.2, the standard deviation of the experimental uncertainties at room temperature and 37^o C are similar in magnitude, highlighting subpixel or submicron resolution.

	25^o C	37^o C
u_1 [voxel]	0.0605	0.0289
u_2 [voxel]	0.0541	0.0282
u_3 [voxel]	0.2106	0.187
ϵ_{11} (%)	6.39 x 10^{-3}	6.59 x 10^{-2}
ϵ_{22} (%)	9.80 x 10^{-3}	6.04 x 10^{-2}
ϵ_{33} (%)	0.260	0.526

Table 3.2: Standard deviation values for measured displacement fields in the undeformed condition for agarose gels at 25^o C and polyacrylamide gels at 37^o C

This chapter describes the experimental setup to perform live cell imaging experiments using laser scanning confocal microscopy including the fabrication of fibronectin-modified polyacrylamide gel substrates with embedded submicron fluorescent particles. The next chapter presents the quantitative findings of cell induced material deformations during cell movement as imaged by laser scanning confocal microscopy and analyzed by digital volume correlation.

Chapter 4

Quantifying Three-Dimensional Deformations of Migrating Fibroblasts

This chapter presents the full-field displacements and tractions of 3T3 fibroblast cells during migration on polyacrylamide (PA) substrates of varying stiffness. The notation of a *soft* substrate corresponds to a Young's modulus of the polyacrylamide gel of ~ 0.82 kPa, whereas *stiff* denotes a Young's modulus of ~ 9.64 kPa as presented in Chapter 3. While the displacement fields are calculated on a uniformly spaced Cartesian grid given by the DVC algorithm, the cell's orientation oftentimes does not follow a principal Cartesian coordinate direction. Hence, due to the finite grid spacing used in the DVC calculations (8 voxels or ~ 2 μm) interpolation may be necessary to determine the displacement and strain field values for an arbitrary orientation. The data presented here are interpolated only as necessary between grid points utilizing primarily a trilinear scheme. Occasionally tricubic interpolation is utilized to better resolve steeper gradients, though trilinear interpolation is generally preferred since it introduces less data smoothing. However, for additional computational cost the DVC grid spacing could be reduced to a minimal value of 1 voxel. Yet this cost is enormous (on the order of days to weeks per volume stack), and hence is not performed within the scope of this study.

4.1 Three-Dimensional Displacements and Tractions

This section defines the displacement and traction notations that will be used throughout the chapter. It also describes how cell applied tractions are calculated. Chapter 2 described in depth how the three-dimensional displacements and the associated strains are calculated. All of the calculated and presented displacements, tractions and surface normals are referenced to the generalized Cartesian coordinates x_1, x_2, x_3.

4.1.1 Definition of the Three-Dimensional Displacement Vector

The three-dimensional displacement vector $\mathbf{u}$, having components u_1, u_2, and u_3, is defined as

$$\mathbf{u} = \begin{pmatrix} u_1 \\ u_2 \\ u_3 \end{pmatrix}, \tag{4.1}$$

with its magnitude given by

$$|\mathbf{u}| = \sqrt{u_1^2 + u_2^2 + u_3^2}. \tag{4.2}$$

4.1.2 Traction Calculations

Chapter 3 presented the material characterization of the polyacrylamide gels, and it was experimentally shown that these can be reasonably treated as isotropic, linearly elastic, incompressible, time-independent materials for the context of the here presented study. At each time increment the cell-induced strains were computed and it was found that the strains were within the linear range of the material behavior, in particular, the strain magnitudes per time increment were consistently found to be less than 5%. Chapter 2 described how the strain tensor is calculated, which will be denoted here as $\boldsymbol{\epsilon}$.

In order to calculate traction stresses including surface tractions, the stress tensor $\boldsymbol{\sigma}$ needs to be

determined first, and is calculated, based on the above constitutive properties as

$$\boldsymbol{\sigma} = 2\mu\boldsymbol{\epsilon}, \tag{4.3}$$

where μ is the shear modulus, which is related to Young's modulus E and to Poisson's ratio ν by

$$E = 2\mu(1+\nu). \tag{4.4}$$

Calculation of the traction stresses involves using the well-known Cauchy relation

$$\mathbf{T} = \boldsymbol{\sigma} \cdot \mathbf{n}, \tag{4.5}$$

where $\mathbf{T}$ is defined as the three-dimensional traction vector, and $\mathbf{n}$ is the surface normal of an arbitrary plane on which $\mathbf{T}$ acts given by

$$\mathbf{T} = \begin{pmatrix} T_1 \\ T_2 \\ T_3 \end{pmatrix}, \tag{4.6}$$

and

$$\mathbf{n} = \begin{pmatrix} n_1 \\ n_2 \\ n_3 \end{pmatrix}. \tag{4.7}$$

The magnitude of the three-dimensional traction vector is then defined as

$$|\mathbf{T}| = \sqrt{T_1^2 + T_2^2 + T_3^2}. \tag{4.8}$$

All tractions are presented in units of $pN/\mu m^2$ or Pascal (Pa), and can also be represented as a individual traction forces per unit area.

4.2 Three-Dimensional Cell-Induced Displacements During Cell Migration on Soft Substrates

Full-field displacement measurements were carried out using the LSCM-DVC technique applied to migrating 3T3 Fibroblast cells on soft polyacrylamide gels. The results shown here represent the cell-induced deformation fields that were observed tracking single cells over an extended period of time. Confocal volume stacks were recorded at 35 min time increments, while each cell was tracked over several hours. Further details of the imaging conditions including the size of the imaged volumes is described in Chapter 3. Time t_0 denotes the start point of each experiment, whereas t_1 describes the first 35 min time increment. Altough the initial cell spreading time history was not recorded, the results display snapshots of the dynamic interactions between the single fibroblast cell and the substrate. The substrate thickness for the subsequently shown results is 40 μm. In order to reduce the effects of phototoxicity and photobleaching during cell imaging, the imaged confocal volume size was limited to 48% of the total substrate thickness. As the subsequent Figs. show, this volume size is sufficient to capture most of the cell-induced deformation field within the resolution limits of the technique. The LSCM-DVC method is able to detect displacement changes greater than 0.12 μm, where 0.12 μm was determined to be the sensitivity threshold through baseline tests. These baseline tests consist of the same material and experimental setup but without any cells present, which allows establishing the measurement sensitivity.

The cell is visualized simultaneously with the displacement of the fluorescent particles inside the polyacrylamide gels using two separate photodetectors. This procedure allows correlating the position of the cell determined by the GFP-actin fluorescent marker construct with the substrate displacement field. GFP-actin highlights the actin filaments of the cell, which are one of the three main structural filaments comprising a cell. Therefore, GFP-actin can be used the visualize the shape of the cell during the migration increments. However, due to the finite life-time of the fluorescent protein marker used to visualize the cell shape, occasionally parts of the cell are not visible at locations where considerable deformations are observed.

Figure 4.1 shows a time evolution of the surface displacement fields beneath a migrating cell over a time span of 140 min. The color contour plots display the magnitude of the three-dimensional displacement vector $|\mathbf{u}|$ in μm. The linear dimension of the cell along its major axis in all of the plots is approximately 100 μm. The direction of cell migration is from the left to the right. The cell migration speed, as determined by tracking the nucleus of the cell, is $\approx$ 18 μm/hr, which is within the range of reported fibroblast migration speeds on polyacrylamide gels [29].

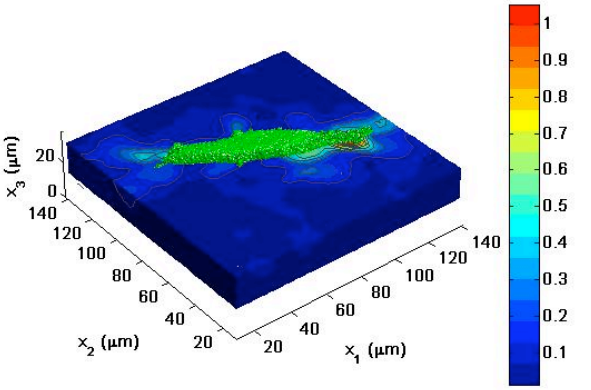

(a) Cell-induced surface displacements at $t_1 = 35$ min

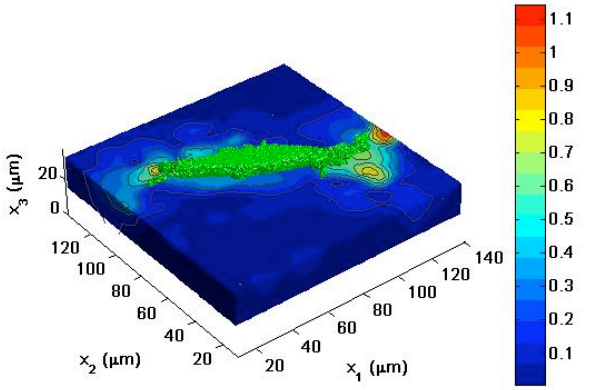

(b) Cell-induced surface displacements at $t_2 = 70$ min

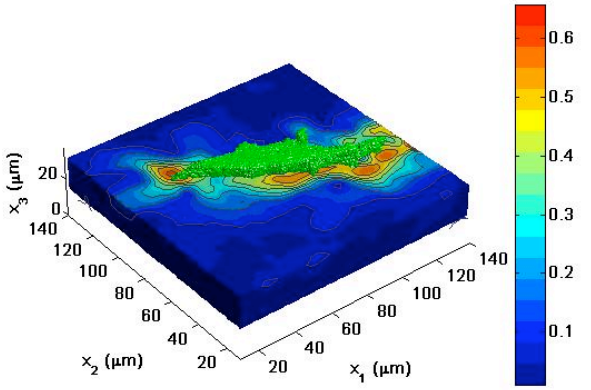

(c) Cell-induced surface displacements at $t_3 = 105$ min

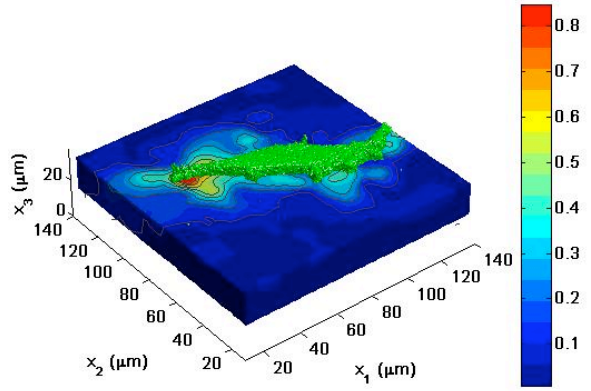

(d) Cell-induced surface displacements at $t_4 = 140$ min

Figure 4.1: Surface contour plots of the magnitude of the three-dimensional displacement vector during cell migration. The color bar represents the magnitude of the total three-dimensional displacement vectors in μm, and the cell (green) is superimposed on the three-dimensional contour plots to show its position with respect to the deformation field.

Figure 4.2 shows the time evolution of the displacement field along an arbitrary slice beneath the migrating cell's long axis over a time span of 140 min. Here the decay of the magnitude of the three-dimensional displacement vectors are shown for the same time series as in Fig. 4.1. The color contour plots display the magnitude of the three-dimensional displacement vector in μm. The displacement contour slices highlight the dynamic interaction of the cell with its substrate as characterized by changes in magnitudes and location of the observed displacements.

Figure 4.3 examines the displacement field of the arbitrary planar slice in Fig. 4.2(a) in more detail. Figure 4.3(a) shows the magnitude of the three-dimensional displacement vector as color contours along the same planar slice, while the white arrows represent the (u_3, u_1) displacement components. The color bar displays the units in μm, whereas the magnitude of the longest arrow corresponds to 0.8 μm. Figure 4.3(b) plots an enlarged picture of Fig. 4.3(a) highlighting an arbitrarily chosen location to generate a line profile of each displacement component as a function of depth (x_3), which is shown in Fig. 4.3(c). While the overall displacement magnitude decays approximately as $x_3^{3/2}$, the magnitude of the individual displacement components highlights the importance of the u_3 component at that particular time increment (t_1).

Figure 4.4 displays the displacement distribution along the same arbitrary plane as in Fig. 4.3 for the next time increment $t_2 = 70$ min. Figure 4.4(a) shows the magnitude of the three-dimensional displacement vector as color contours along the same planar slice, while the white arrows represent the (u_3, u_1) displacement components. The color bar displays the units in μm, whereas the magnitude of the longest arrow corresponds to 0.8 μm. Figure 4.3(b) plots an enlarged picture of Fig. 4.3(a) highlighting an arbitrarily chosen location to generate a line profile of each displacement component as a function of penetration depth (x_3), which is shown in Fig. 4.3(c). The displacement contour and line profiles show a slower decay with thickness than presented in Fig. 4.3 at time t_1.

Figures 4.5 and 4.6 display the surface displacement fields presented in Figs. 4.1(a) and 4.1(b) in more detail. In particular, Fig. 4.5(a) shows the magnitude of the three-dimensional displacement vector as color contours directly underneath the migrating cell, while the white arrows represent the $\{u_1, u_2\}$ displacement components. The color bar displays the units in μm, whereas the magnitude

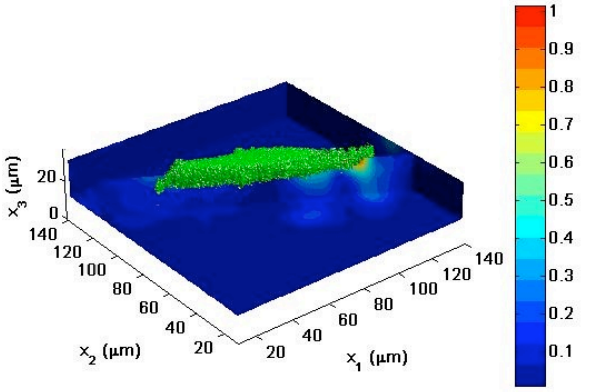

(a) Cell-induced displacements at $t_1 = 35$ min

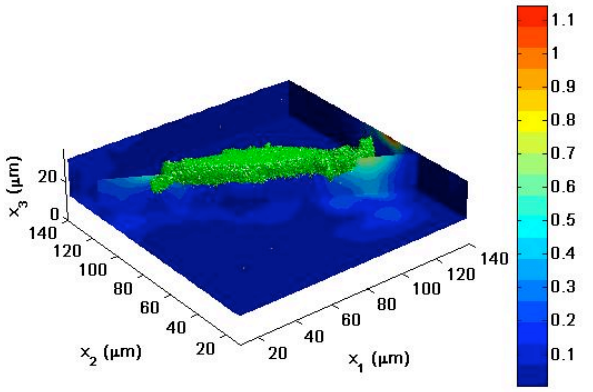

(b) Cell-induced displacements at $t_2 = 70$ min

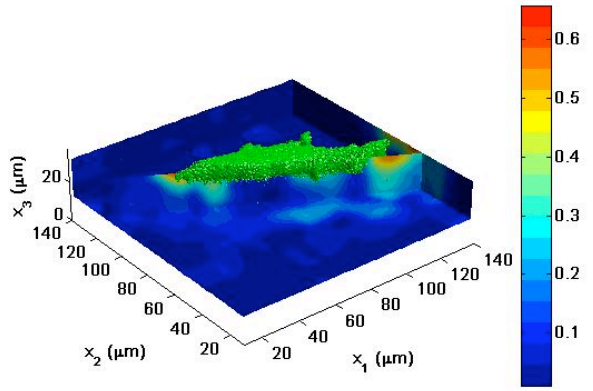

(c) Cell-induced displacements at $t_3 = 105$ min

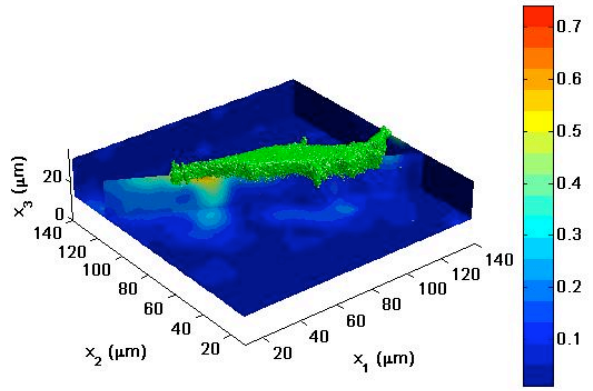

(d) Cell-induced displacements at $t_4 = 140$ min

Figure 4.2: Arbitrary displacement contour slices along the long axis of the cell. The slices of displacement contours underneath migrating cells show significant deformation in the normal plane that decay along the thickness of the sample. The two edges in the image are included to show that there are negligible displacements detected from neighboring cells (contours are dark blue). The color bar represents the magnitude of the total three-dimensional displacement vectors in μm, and the cell (green) is superimposed on the three-dimensional contour plots to show its position with respect to the deformation field.

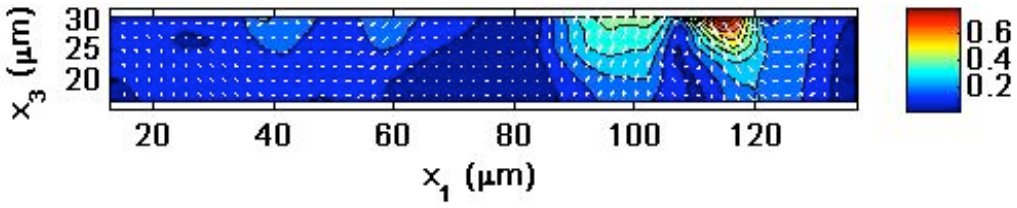

(a) Cross-sectional displacement contour plot through the substrate thickness at $t_1 = 35$ min

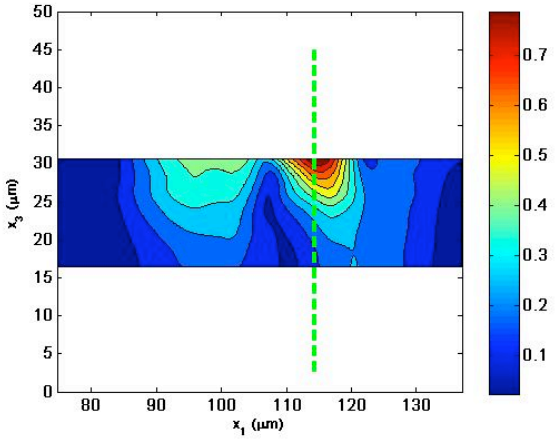

(b) Enlarged view of the contour plot in 4.3(a) and location of displacement line plot shown in 4.3(c)

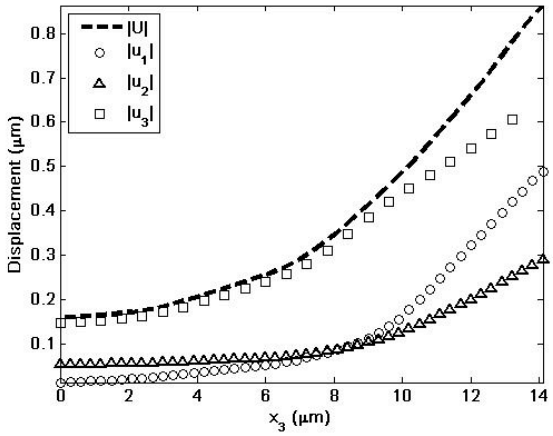

(c) Displacement line profile through the thickness of the gel (x_3). The maximum x_3 value corresponds to the gel surface.

Figure 4.3: Displacement contour and line plot profiles as a function of depth (x_3) through the thickness of the gel. Figure 4.3(a) shows the same displacement contours along the long axis of the cell as shown in Fig. 4.2(a), where the color bar represents the magnitude of the three-dimensional displacement vectors in μm, and the white arrows show the direction of the in-plane (u_1,u_3) displacement components only. Figure 4.3(b) shows the zoom-in image of Fig. 4.3(a), whereas Fig. 4.3(c) illustrates the decay of all three displacement components in the x_3 direction, where $x_3 = 14$ represents the location of the top surface.

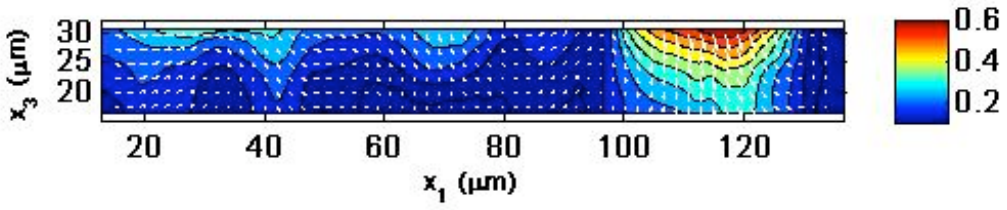

(a) Cross-sectional displacement contour plot through the substrate thickness at $t_2 = 70$ min

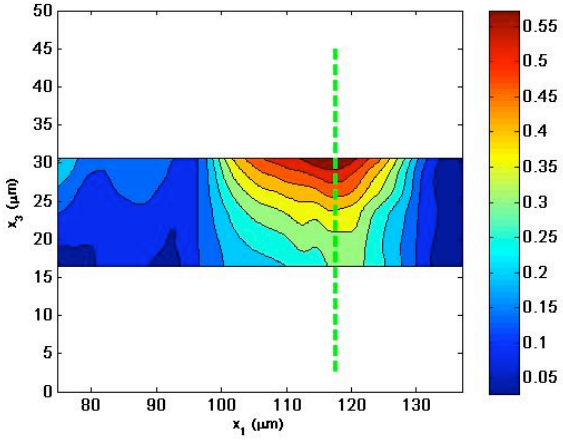

(b) Enlarged view of the contour plot in 4.4(a) and location of displacement line plot shown in 4.4(c)

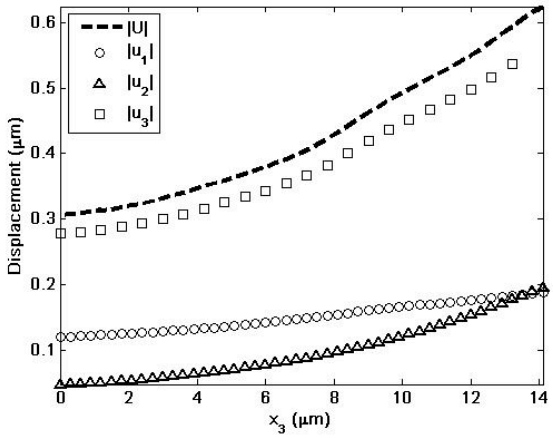

(c) Displacement line profile through the thickness of the gel (x_3). The maximum x_3 value corresponds to the gel surface.

Figure 4.4: Displacement contour and line plot profiles as a function of depth (x_3) through the thickness of the gel. Figure 4.4(a) shows the same displacement contours along the long axis of the cell as shown in Fig. 4.2(b), where the color bar represents the magnitude of the three-dimensional displacement vectors in μm, and the white arrows show the direction of the in-plane (u_1,u_3) displacement components only. Figure 4.3(b) shows the zoom-in image of Fig. 4.3(a), whereas Fig. 4.3(c) illustrates the decay of all three displacement components in the x_3 direction, where $x_3 = 14$ represents the location of the top surface.

of the longest arrow corresponds to 1.6 μm. Figure 4.5(b) plots an enlarged picture of Fig. 4.5(a) highlighting an arbitrarily chosen location to generate a line profile of each displacement component as a function of spatial distance, which is shown in Fig. 4.3(c). Here, the displacement distribution follows an almost Gaussian profile obtaining a maximum value of 1.8 μm over a length of $\sim$ 1 μm, most likely corresponding to the particular location of a focal adhesion complex. As shown in Fig. 4.3(c), the u_3 displacement components obtain their local maximum values around the overall displacement peak, with a minimum at the location where the overall displacements are maximum.

Figure 4.6(a) shows the same series of plots as Fig. 4.5(a) for the next time increment (t_2 = 70 min). The color contours display the magnitude of the three-dimensional displacement vector underneath the fibroblast, while the white arrows represent the (u_1, u_2) displacement components. The color bar displays the units in μm, whereas the magnitude of the longest arrow corresponds to 1.8 μm. Figure 4.6(b) plots an enlarged picture of Fig. 4.6(a), highlighting an arbitrarily chosen location to generate a line profile of each displacement component as a function of spatial distance, which is shown in Fig. 4.3(c). The line profiles for both Figs. 4.3(c) and 4.4(c) were chosen at the leading edge of the motile cell. Comparing the contour plots and in particular the line profile plots, Fig. 4.4(c) shows a similar displacement distribution profile. In particular, the u_3 displacement component follows the same trend as in Fig. 4.3(c) attaining two local maxima right before the maximum peak in the total displacement, showing a minimum at the overall displacement peak itself. However, instead of showing only one single total displacement peak, Fig. 4.4(c) depicts two local maxima over an approximate distance of $\sim$ 1 μm.

Figure 4.7 compares the surface displacement fields directly underneath the migrating cells shown in Fig. 4.1(a) and 4.1(b) by highlighting the contribution of the u_3 displacement component. Figures 4.7(a) and 4.7(c) show the displacement contours of the magnitude of the three-dimensional displacement vector whereas Figs. 4.7(b) and 4.7(d) display the magnitude of only the two-dimensional (u_1, u_2) displacement vectors. Side-by-side comparison reveals that most of the deformation occurs in-plane, i.e. (u_1, u_2) are dominating, however there are particular areas where the u_3 displacement component proves to be significant. These areas are found along the periphery of the maximum

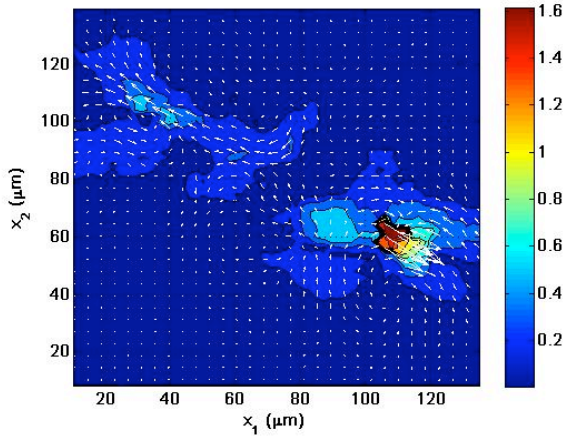

(a) Surface displacement contour plot underneath the migrating cell at $t_1 = 35$ min

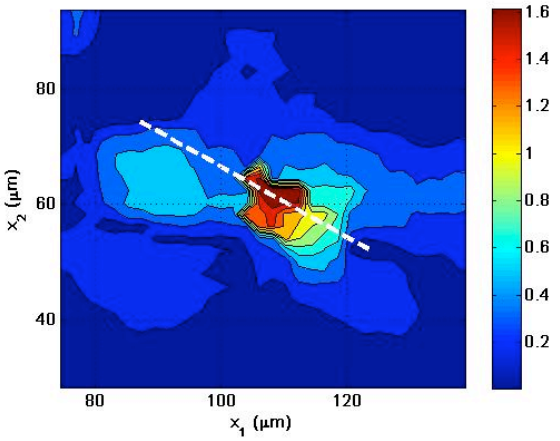

(b) Enlarged view of the contour plot in 4.5(a) and location of displacement line plot shown in 4.5(c) (dashed line)

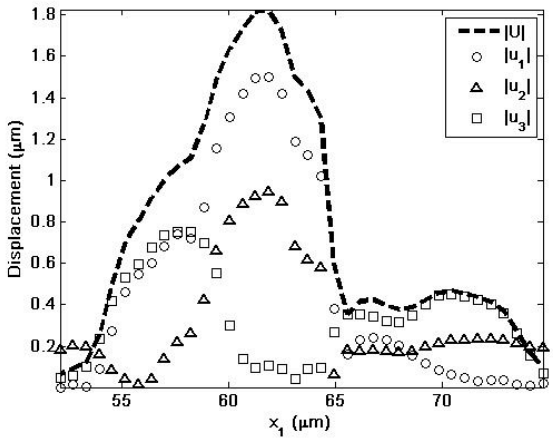

(c) Surface displacement profile along the selected line in 4.5(b)

Figure 4.5: Surface displacement contour and line plot profiles along a particular line in the $x_1 - x_2$ surface plane at $t_1 = 35$ min. Figure 4.5(a) shows the same displacement contours as shown in Fig. 4.1(a), where the color bar represents the magnitude of the three-dimensional displacement vectors in μm, and the white arrows show the direction of the in-plane (u_1,u_2) displacement components only. Figure 4.5(b) shows the zoom-in image of Fig. 4.5(a) highlighting the particular region where the line plot was generated. Figure 4.5(c) illustrates the distribution of all three displacement components along the selected line.

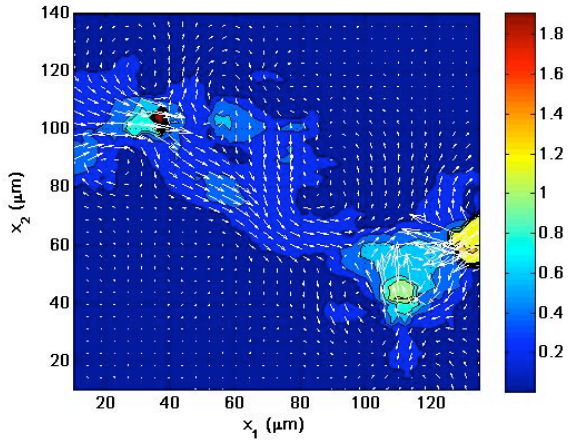

(a) Surface displacement contour plot underneath the migrating cell at $t_2 = 70$ min

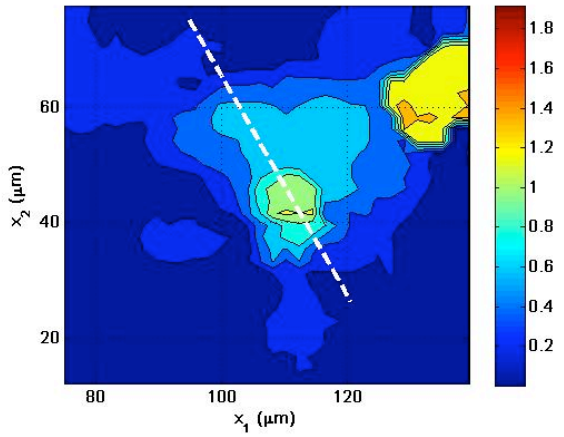

(b) Enlarged view of the contour plot in 4.6(a) and location of displacement line plot shown in 4.6(c) (dashed line)

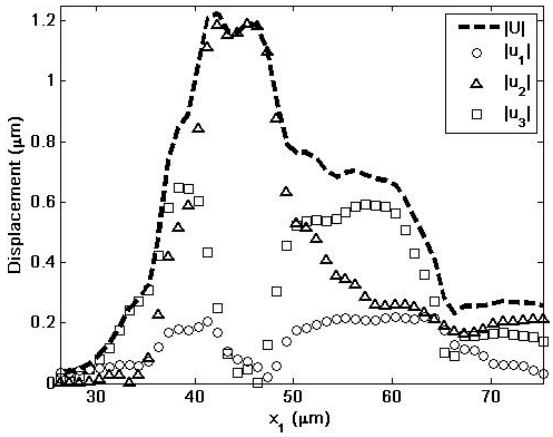

(c) Surface displacement profile along the selected line in 4.6(b)

Figure 4.6: Surface displacement contour and line plot profiles along a particular line in the $x_1 - x_2$ surface plane at $t_2 = 70$ min. Figure 4.6(a) shows the same displacement contours as shown in Fig. 4.1(b), where the color bar represents the magnitude of the three-dimensional displacement vectors in μm, and the white arrows show the direction of the in-plane (u_1,u_2) displacement components only. Figure 4.5(b) shows the zoom-in image of Fig. 4.6(a) highlighting the particular region where the line plot was generated. Figure 4.6(c) illustrates the distribution of all three displacement components along the selected line.

displacement peaks, and are also observed in Figs. 4.5(c) and 4.6(c).

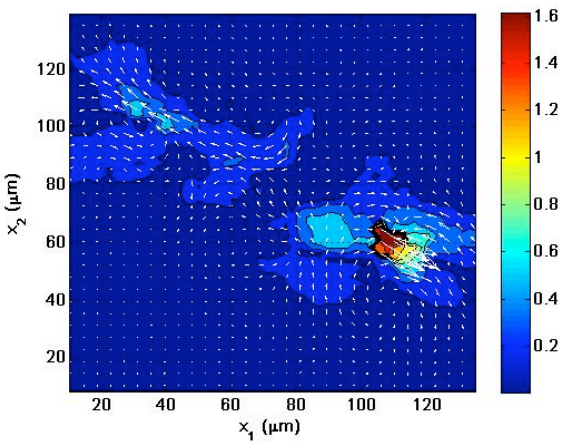

(a) Cell-induced surface displacements (3D) at $t_1 = 35$ min

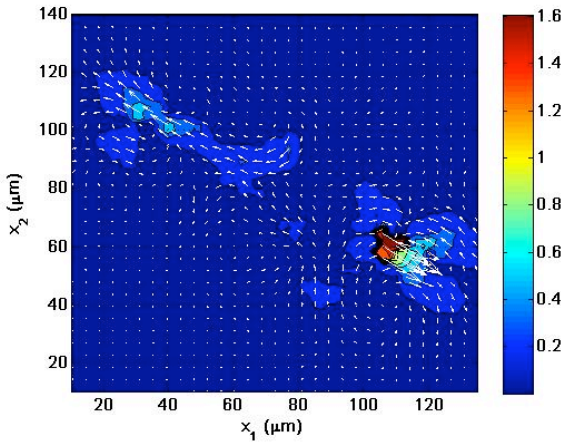

(b) Cell-induced surface displacements (2D) at $t_1 = 35$ min

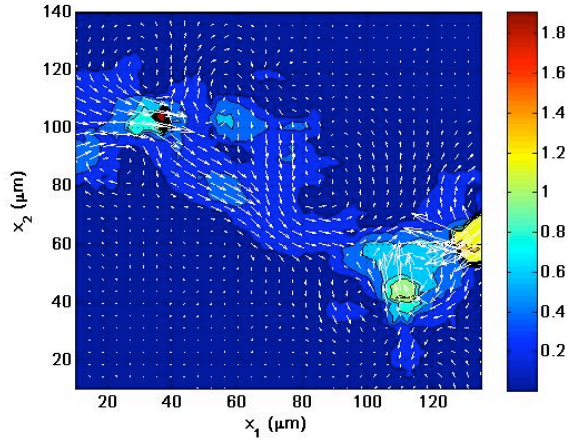

(c) Cell-induced surface displacements (3D) at $t_2 = 70$ min

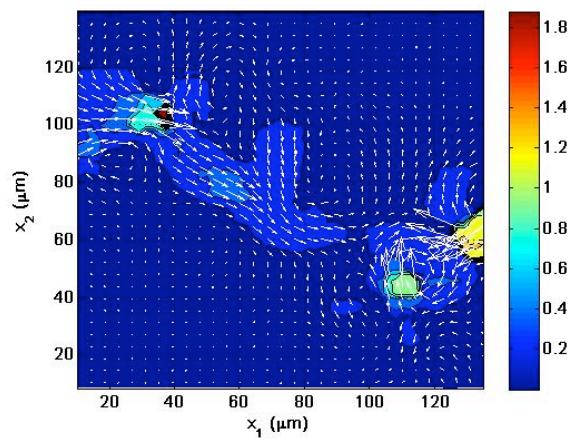

(d) Cell-induced surface displacements (2D) at $t_2 = 70$ min

Figure 4.7: Comparison between the displacement magnitude of all three-dimensional vector components (4.7(a) and 4.7(c)) and the magnitude of the two-dimensional vector components only (4.7(b) and 4.7(d)). The color bar is displaying all displacement values μm, and and the white arrows show the direction of the in-plane (u_1,u_2) displacement components only.

4.3 Three-Dimensional Tractions During Cell Migration on Soft Substrates

This section presents the tractions calculated based upon the measured displacement fields reported in the previous section. Since the determination of the tractions involves calculating the strain tensor and the experimental determination of material constants, the sensitivity of the LSCM-DVC technique in terms of the calculated tractions needs to be assessed. This is accomplished by performing experiments using the same materials setup as in the case for the migrating fibroblasts, but without any cells present. Hence, the measured displacements and calculated tractions are solely due to thermal fluctuations, instrumental and measurement error, and thus establish the sensitivity of the traction calculations. Using standard error analysis the technique can accurately detect stresses and tractions that are greater than 8 Pa or 8 pN/μm^2. All of the subsequently presented Figs. are from the same data set as the displacement results reported in Section 4.2.

Figure 4.8 shows a time evolution of the cell surface tractions during migration over a time span of 140 min. The color contour plots display the magnitude of the three-dimensional traction vector in $pN/\mu m^2$. Again, the linear dimension of the cell in all of the plots is approximately 100 μm. The direction of cell migration is from the left to the right. The localized nature of the tractions is clearly visible in all time frames. As explained earlier due to the degradation of the actin-fluorescent cell stain (GFP-actin), the cell's outline is not always visible directly above some of the stress concentration locations, although the cell is still transmitting force there, as has been confirmed through multiple experiments where GFP-actin was clearly visible.

Figure 4.9 shows the time evolution of the traction field along an arbitrary slice beneath the migration cell's long axis over a time span of 140 min. The tractions acting along the shown plane were calculated through the Cauchy relationship (see Section 4.1.2) with the stress tensor, where the plane is defined by its normal, $\mathbf{n} = (n_1 \quad n_2 \quad 0)^T$, where n_1 and n_2 can be expressed in terms of sine and cosine of the in-plane angle that defines each arbitrarily chosen plane. The decay of the magnitude of the three-dimensional traction vector is shown for the same time series as in figure

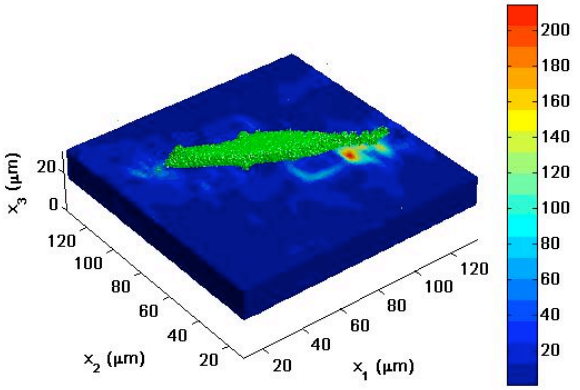

(a) Cell-induced surface tractions at $t_1 = 35$ min

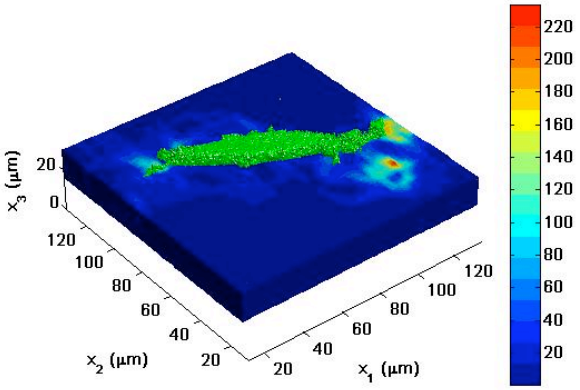

(b) Cell-induced surface tractions at $t_2 = 70$ min

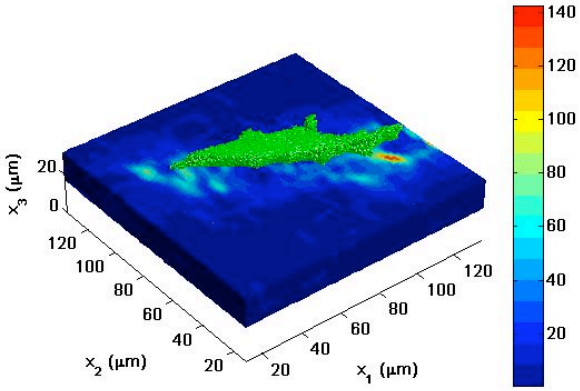

(c) Cell-induced surface tractions at $t_3 = 105$ min

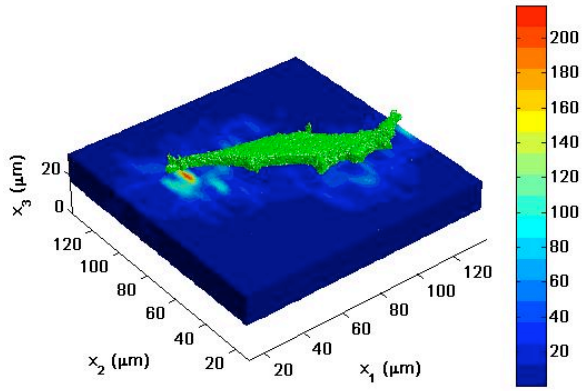

(d) Cell-induced surface tractions at $t_4 = 140$ min

Figure 4.8: Surface contour plots of the magnitude of the three-dimensional traction vector during cell migration. The color bar represents the magnitude of the total three-dimensional surface traction vectors in $pN/\mu m^2$, and the cell (green) is superimposed on the three-dimensional contour plots to show its position with respect to the traction field.

4.8. The color contour plots display the magnitude of the three-dimensional traction vector in $pN/\mu m^2$. The traction contour slices highlight the dynamic interaction of the cell with its substrate characterized by changes in magnitudes and location of the observed tractions. It should be noted that in figure 4.9(d) the cell outline extends past the rear end of the stress concentration (around $x_1 = 30\ \mu m$, $x_2 = 120\ \mu m$).

Figure 4.10 shows the traction field of the arbitrary planar slice shown in Fig. 4.9(a) in more detail. Figure 4.10(a) shows the magnitude of the three-dimensional traction vector as color contours along the same planar slice, while the white arrows represent the (T_3, T_1) traction vector components. The color bar displays the units in $pN/\mu m^2$, whereas the magnitude of the longest arrow corresponds to 40 $pN/\mu m^2$. Figure 4.10(b) plots an enlarged picture of Fig. 4.10(a) highlighting an arbitrarily chosen location to generate a line profile of each traction component as a function of depth (x_3), which is shown in Fig. 4.10(c). Comparing the decay of the magnitude of the three-dimensional traction vector to the decay of the total displacement vector in Fig. 4.3(c), the tractions decay noticeably faster than the corresponding displacements.

Figure 4.11 displays the distribution of the tractions along the same arbitrary plane as in Fig. 4.10 for the next time increment $t_2 = 70$ min. Figure 4.11(a) shows the magnitude of the three-dimensional traction vectors as color contours along the same planar slice, while the white arrows represent the (T_3, T_1) displacement components. The color bar displays the units in $pN/\mu m^2$, whereas the magnitude of the longest arrow corresponds to 100 $pN/\mu m^2$. Figure 4.11(b) plots an enlarged picture of Fig. 4.11(a), highlighting an arbitrarily chosen location to generate a line profile of each traction component as a function of depth (x_3), which is shown in Fig. 4.11(c). The traction contours and line profiles show a similar decay with thickness as presented in Fig. 4.10 at time t_1, however, in Fig. 4.11(c) T_3 is the dominant force term as compared to Fig. 4.10(c) where the in-plane tractions are most significant.

Figures 4.12(a) and 4.13(a) display the surface traction fields presented in Figs. 4.8(a) and 4.8(b) in more detail. In particular, Fig. 4.5(a) shows the magnitude of the three-dimensional traction vectors as color contours directly underneath the migrating cell, while the white arrows

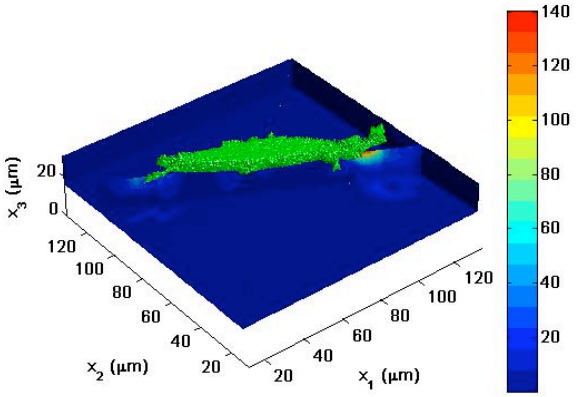

(a) Cell tractions at $t_1 = 35$ min

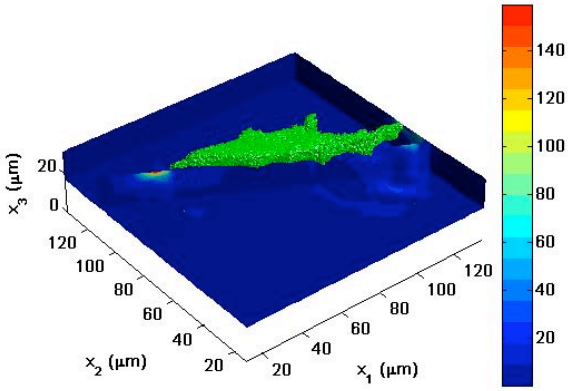

(b) Cell tractions at $t_2 = 70$ min

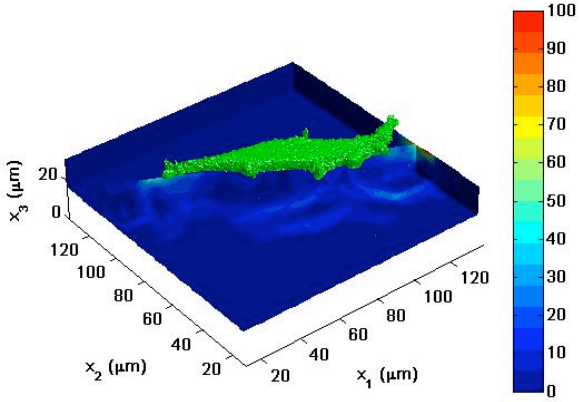

(c) Cell tractions at $t_3 = 105$ min

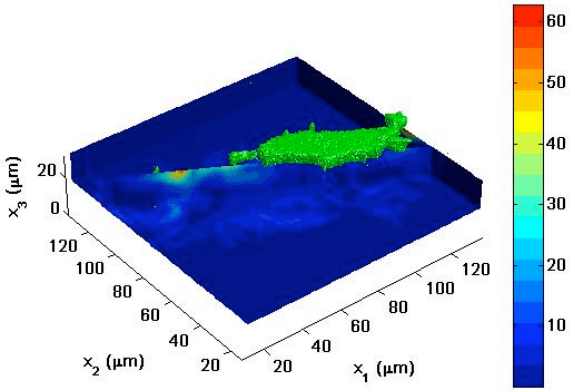

(d) Cell tractions at $t_4 = 140$ min

Figure 4.9: Arbitrary traction contour slices along the long axis of the cell. The color bar indicates the magnitude of the three-dimensional traction vectors along that particular plane in units of $pN/\mu m^2$. The slices of the traction contours underneath the migrating cells correspond to the displacement slices shown in Fig. 4.2. The two edges in the image are included to show that there are negligible tractions detected from neighboring cells (contours are dark blue). The cell (green) is superimposed on the three-dimensional contour plots to show its position with respect to the traction field.

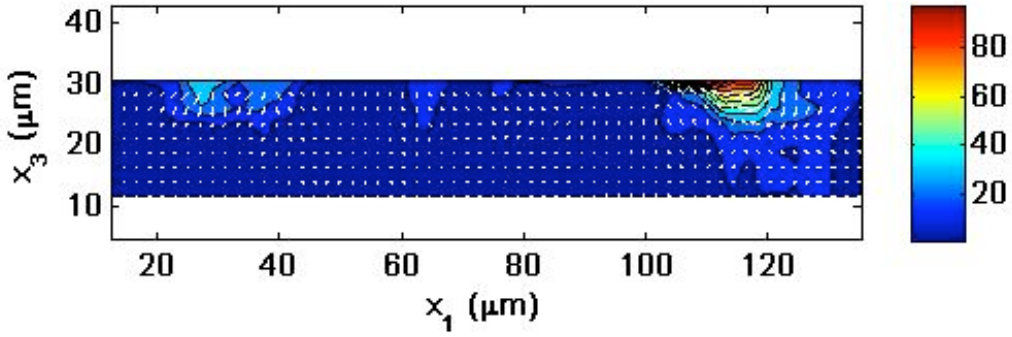

(a) Cross-sectional traction contour plot through the substrate thickness at $t_1 = 35$ min

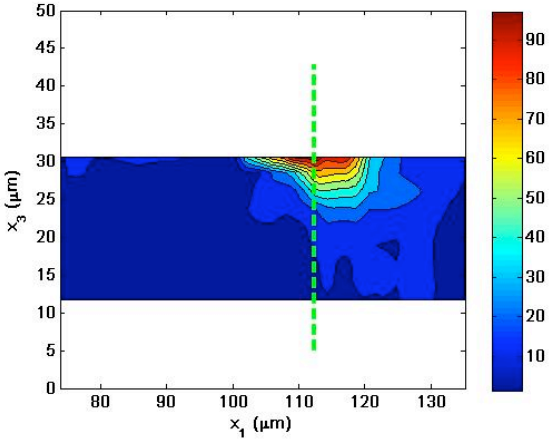

(b) Enlarged view of the contour plot in 4.10(a) and the location of traction line plot shown in 4.10(c)

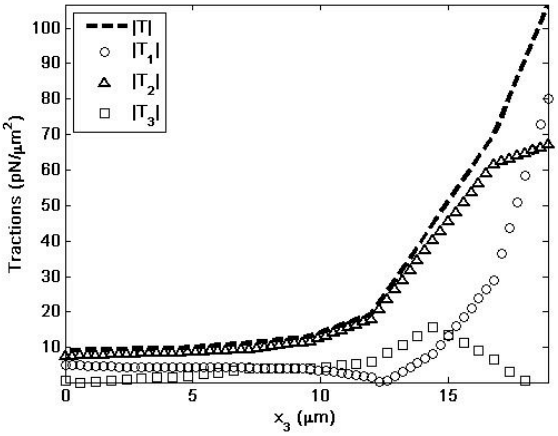

(c) Traction force line profile through the thickness of the gel (x_3). The maximum x_3 value corresponds to the gel surface

Figure 4.10: Traction contour and line plot profiles as a function of depth (x_3) through the thickness of the gel at time $t_1 = 35$ min. Figure 4.10(a) shows the same traction contours along the long axis of the cell as shown in Fig. 4.9(a), where the color bar represents the magnitude of the three-dimensional traction vectors along that particular plane, and the white arrows show the direction of the in-plane (T_1,T_3) traction components only. Figure 4.10(b) shows the zoom-in image of Fig. 4.10(a), whereas Fig. 4.10(c) illustrates the decay of all traction components and the magnitude of the three-dimensional traction vector in the x_3 direction. The color bar units are displayed in $pN/\mu m^2$.

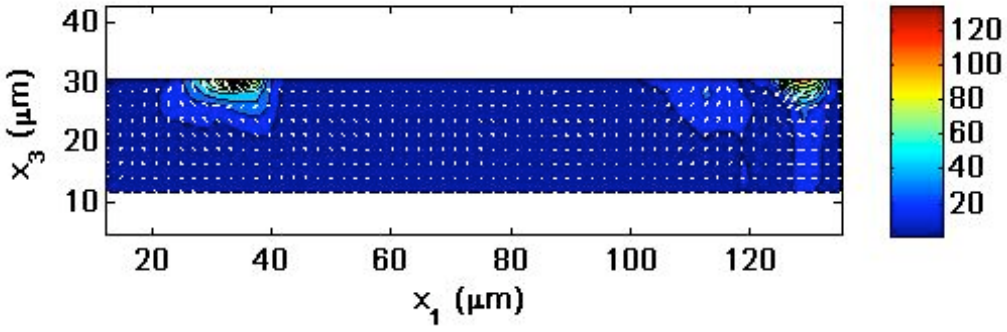

(a) Cross-sectional traction contour plot through the substrate thickness at $t_1 = 70$ min

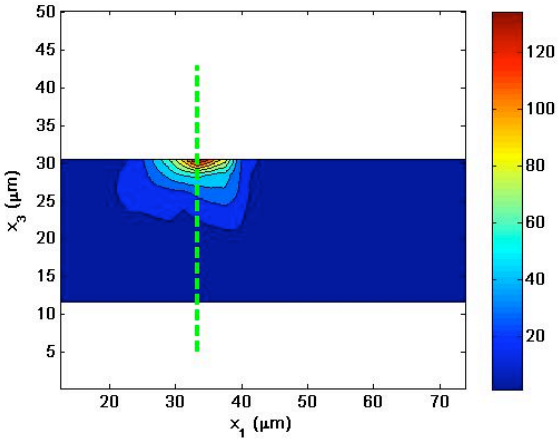

(b) Enlarged view of the contour plot in 4.11(a) and location of the traction line plot shown in 4.11(c)

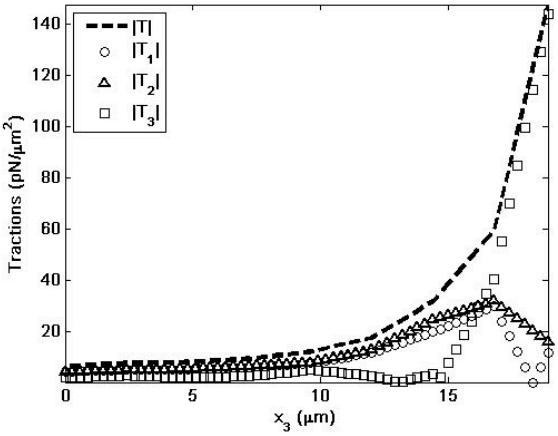

(c) Traction line profile through the thickness of the gel (x_3). The maximum x_3 value corresponds to the gel surface.

Figure 4.11: Traction contour and line plot profiles as a function of depth (x_3) through the thickness of the gel at time $t_2 = 70$ min. Figure 4.11(a) shows the same traction contours along the long axis of the cell as shown in Fig. 4.9(b), where the color bar represents the magnitude of the three-dimensional traction vectors along that particular plane, and the white arrows show the direction of the in-plane (T_1,T_3) traction components only. Figure 4.11(b) shows the zoom-in image of Fig. 4.11(a), whereas Fig. 4.11(c) illustrates the decay of all traction components and the magnitude of the three-dimensional traction vector in the x_3 direction. The color bar units are displayed in $pN/\mu m^2$.

represent the (T_1, T_2) traction components. The color bar displays the units in $pN/\mu m^2$, whereas the magnitude of the longest arrow corresponds to 140 $pN/\mu m^2$. Figure 4.12(b) plots an enlarged picture of Fig. 4.12(a), highlighting an arbitrarily chosen location to generate a line profile of each traction component as a function of spatial distance, which is shown in Fig. 4.12(c). Here, the tractions follow an almost Gaussian distribution obtaining a maximum value of 172 $pN/\mu m^2$ over a length of $\sim$ 1 μm, most likely corresponding to the particular location of a focal adhesion complex.

Figure 4.13(a) shows the same series of plots as Fig. 4.12(a) for the next time increment (t_2 = 70 min). The color contours display the magnitude of the three-dimensional traction vectors underneath the fibroblast, while the white arrows represent the (T_1, T_2) traction components. The color bar displays the units in $pN/\mu m^2$, whereas the magnitude of the longest arrow corresponds to 140 $pN/\mu m^2$. Figure 4.13(b) plots an enlarged picture of Fig. 4.13(a), highlighting an arbitrarily chosen location to generate a line profile of each traction component (T_1, T_2, T_3) and the magnitude of the three-dimensional traction vector ($|\mathbf{T}|$) as a function of spatial distance, which is shown in Fig. 4.3(c). The line profiles in Figs. 4.3(c) and 4.13(c) were chosen at the leading edge of the motile cell. Comparing the contour plots and in particular the two line profile plots, Fig. 4.13(c) shows a broader traction profile with two local maxima. The T_1 traction component attains a single maximum coinciding with the maximum peak of the total traction vector. The T_2 traction component obtains two smaller single peaks at the same spatial location as the overall traction vector, while the T_3 traction component reaches its highest value close to the location where the local minimum value of the total traction vector is shown.

Figure 4.14 compares the surface traction fields directly underneath the migrating cells shown in Figs. 4.8(a) and 4.8(b) by highlighting the contribution of the T_3 traction component. Figures 4.14(a) and 4.14(c) show surface contours of the magnitude of the three-dimensional traction vectors whereas Figs. 4.14(b) and 4.14(d) display the magnitude of only the two-dimensional, in-plane (T_1, T_2) traction vectors. Side-by-side comparison reveals that the cell applies mostly shear tractions (T_1, T_2). While the contribution of T_3 is observed in a few areas, shown in Figs. 4.12(c) and 4.13(c), its overall contribution is relatively insignificant for the given time increments t_1 and t_2.

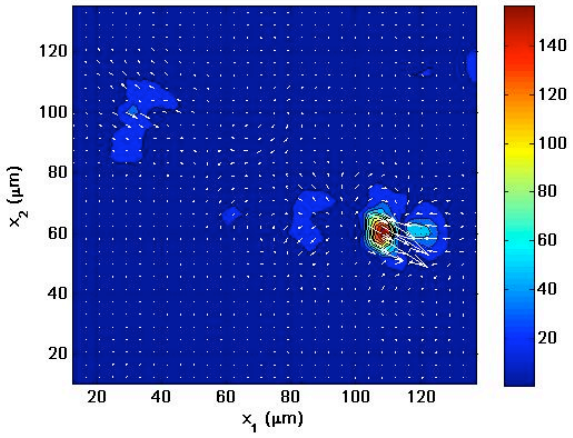

(a) Surface tractions contour plot underneath the migrating cell at $t_1 = 35$ min

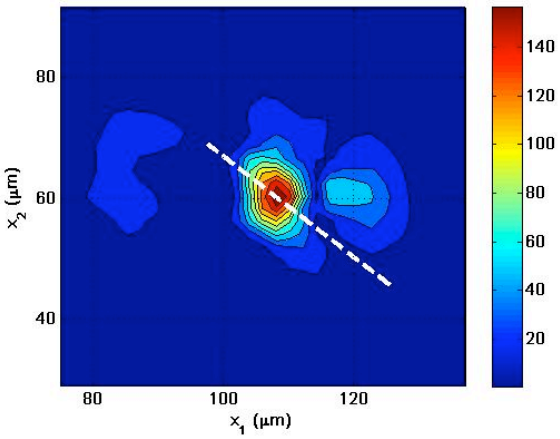

(b) Enlarged view of the contour plot in 4.12(a) and location of the traction line plot shown in 4.12(c)

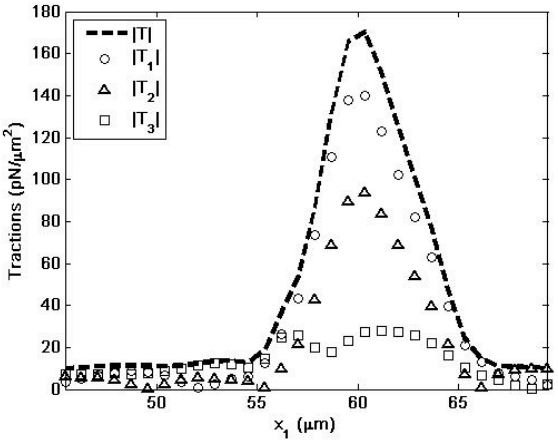

(c) Traction force profile along the selected line in 4.12(b)

Figure 4.12: Surface tractions contour and line plot profiles along a particular line in the $x_1 - x_2$ top surface plane at $t_1 = 35$ min. Figure 4.12(a) shows the same traction contours as shown in Fig. 4.8(a), where the color bar represents the magnitude of the three-dimensional surface traction vectors and the white arrows show the direction of the in-plane (T_1,T_2) traction components only. The color bar units are in $pN/\mu m^2$. Figure 4.5(b) shows the zoom-in image of Fig. 4.12(a) highlighting the particular region, where the line plot was generated. Figure 4.12(c) illustrates the distribution of all three traction components and the magnitude of the three-dimensional traction vector along the drawn line.

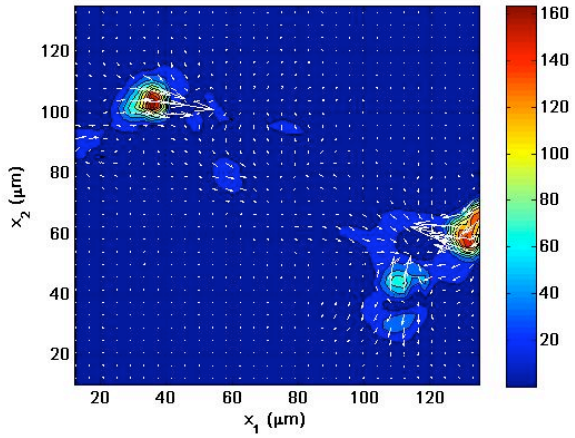

(a) Surface tractions contour plot underneath the migrating cell at $t_2 = 70$ min

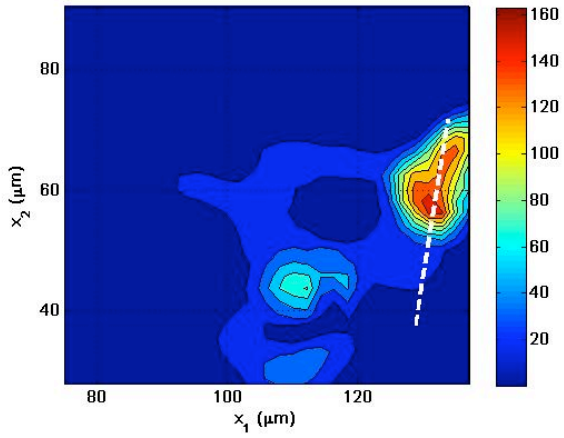

(b) Enlarged view of the contour plot in 4.13(a) and location of the traction line plot shown in 4.13(c)

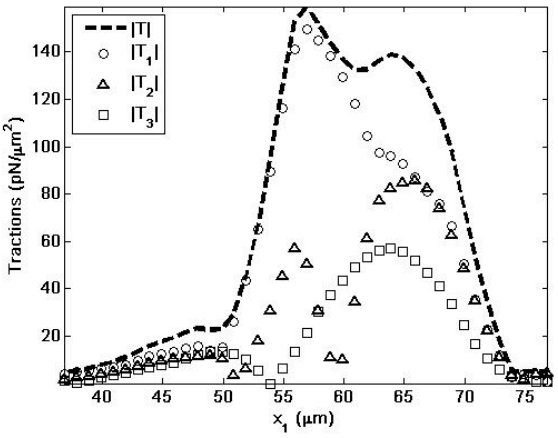

(c) Traction force profile along the selected line in 4.13(b)

Figure 4.13: Surface traction contour and line plot profiles along a particular line in the $x_1 - x_2$ top surface plane at $t_2 = 70$ min. Figure 4.13(a) shows the same traction force contours as shown in Fig. 4.8(b), where the color bar represents the magnitude of the three-dimensional surface traction vectors and the white arrows show the direction of the in-plane (T_1,T_2) traction components only. The color bar units are $pN/\mu m^2$. Figure 4.6(b) shows the zoom-in image of Fig. 4.13(a) highlighting the particular region, where the line plot was generated. Figure 4.13(c) illustrates the distribution of all three traction components and the magnitude of the three-dimensional traction vector along the drawn line.

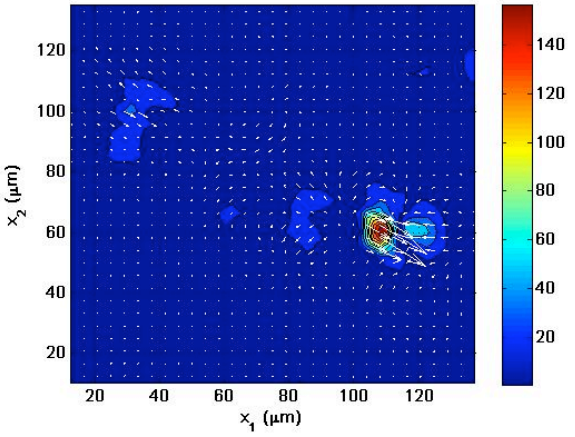

(a) Cell-induced surface tractions (3D) at $t_1 = 35$ min

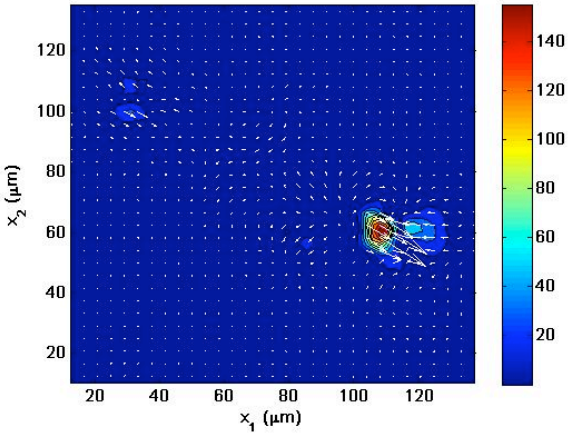

(b) Cell-induced surface tractions (2D) at $t_1 = 35$ min

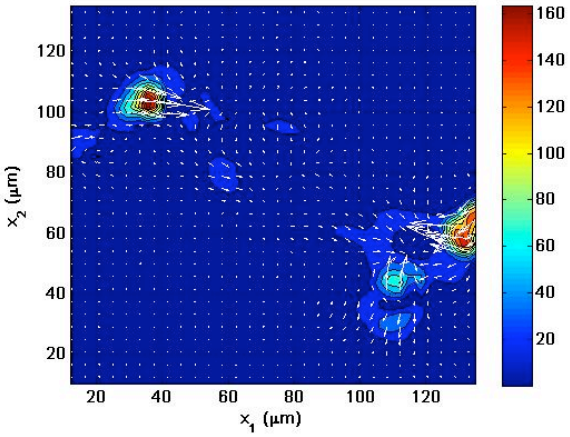

(c) Cell-induced surface tractions (3D) at $t_2 = 70$ min

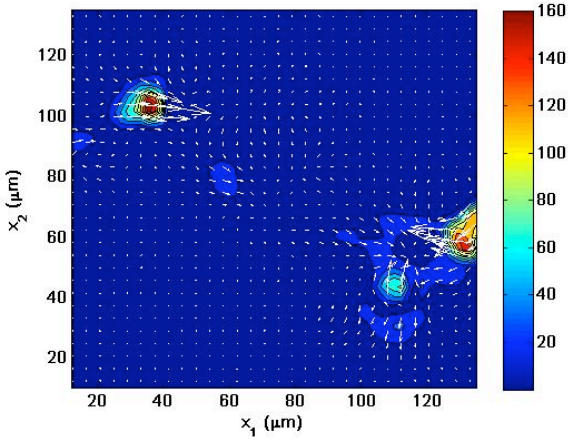

(d) Cell-induced surface tractions (2D) at $t_2 = 70$ min

Figure 4.14: Comparison between the magnitude of the three-dimensional traction vector (4.14(a) and 4.14(c)) and the magnitude of the two-dimensional traction vector (T_1, T_2) components only (4.14(b) and 4.14(d))). The color bar is displaying all traction values in $pN/\mu m^2$, and and the white arrows show the direction of the in-plane (T_1,T_2) traction components only.

4.4 Three-Dimensional Displacements During Cell Migration on Stiff Substrates

This section presents the full-field three-dimensional displacements induced by migration cells on *stiff* substrates (for definitions of *soft* and *stiff* refer to beginning of Chapter 4). All Figs. and results are displayed in the same format as in the previous sections. One observation worth mentioning is that the magnitude of the measured displacement fields are of the same order as those for the *soft* substrates and thus appear independent of the Young's modulus of the substrate material over the range of moduli investigated. These findings are discussed in more detail in Section 4.7.

Figure 4.15 shows a time evolution of the surface displacement fields beneath a migration cell over a time span of 140 min. The color contour plots display the magnitude of the three-dimensional displacement vector in μm. The linear dimension of the cell in all of the plots is approximately 80 - 100 μm. The direction of cell migration is from the left to right. The cell migration speed, as determined by tracking the nucleus of the cell, is ≈ 8 μm/hr.

Figure 4.16 shows the time evolution of the displacement field along an arbitrary slice beneath the migration cell's long axis over a time span of 140 min. Here the decay of the magnitude of the three-dimensional displacement vectors are shown for the same time series as in Fig. 4.15. The color contour plots display the magnitude of the three-dimensional displacement vector in μm. The displacement contour slices highlight the dynamic interaction of the cell with its substrate characterized by changes in magnitudes and location of the observed displacements.

Figure 4.17 shows the displacement field of the arbitrary planar slice in Fig. 4.16(a) in more detail. Figure 4.17(a) shows the magnitude of the three-dimensional displacement vector as color contours along the same planar slice, while the white arrows represent the (u_3, u_1) displacement components. The color bar displays the units in μm, whereas the magnitude of the longest arrow corresponds to 1 μm. Figure 4.17(b) plots an enlarged picture of Fig. 4.17(a), highlighting an arbitrarily chosen location to generate a line profile of each displacement component as a function of depth (x_3), which is shown in Fig. 4.17(c). While the overall displacement magnitude

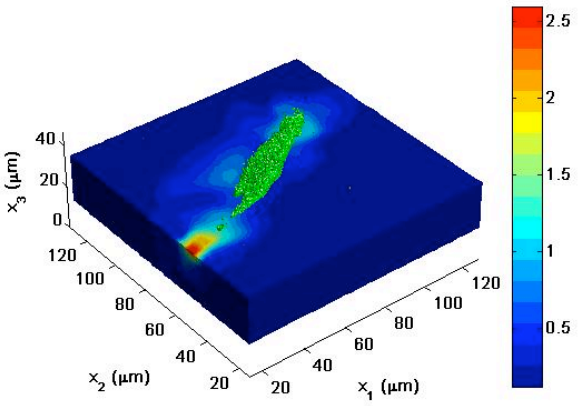

(a) Cell-induced surface displacements at $t_1 = 35$ min

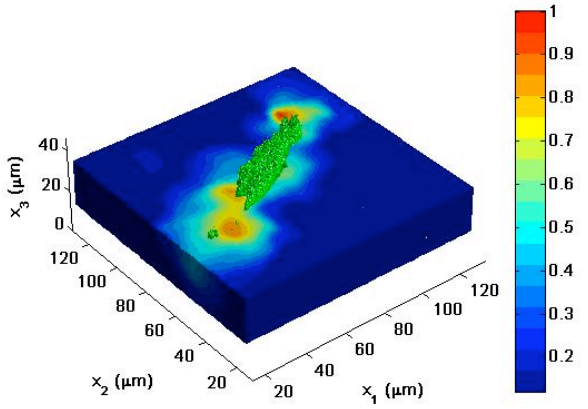

(b) Cell-induced surface displacements at $t_2 = 70$ min

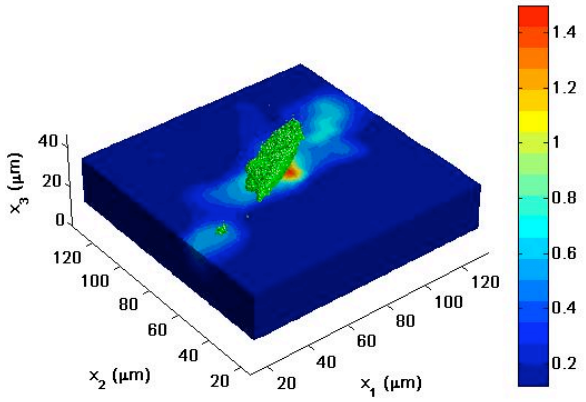

(c) Cell-induced surface displacements at $t_3 = 105$ min

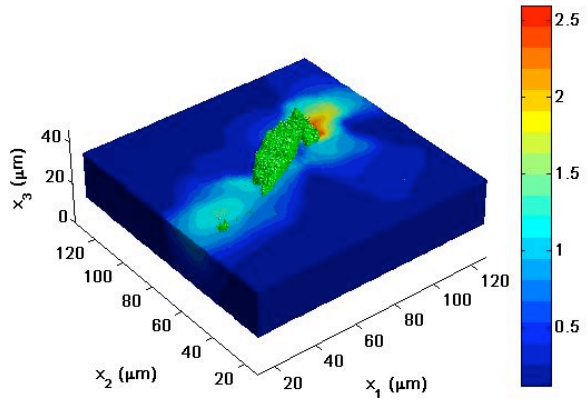

(d) Cell-induced surface displacements at $t_4 = 140$ min

Figure 4.15: Surface contour plots of the magnitude of the three-dimensional displacment vector during cell migration. The color bar represents the magnitude of the total three-dimensional displacement vectors in μm, and the cell (green) is superimposed on the three-dimensional contour plots to show its position with respect to the deformation field.

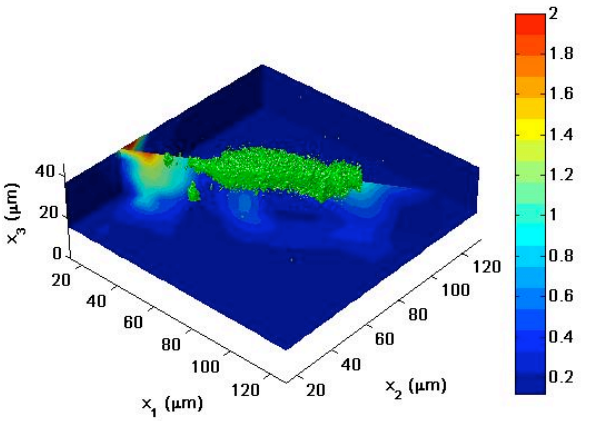

(a) Cell-induced displacements at $t_1 = 35$ min

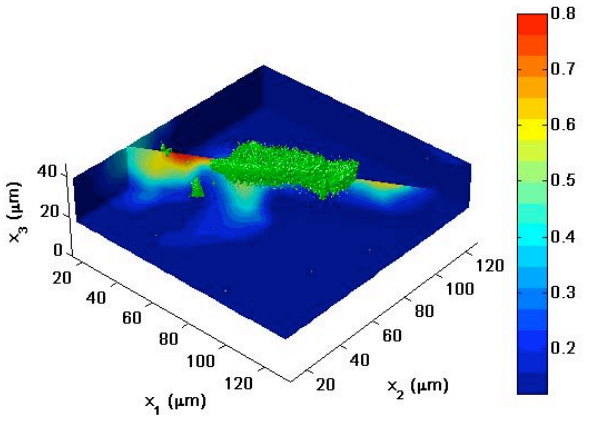

(b) Cell-induced displacements at $t_2 = 70$ min

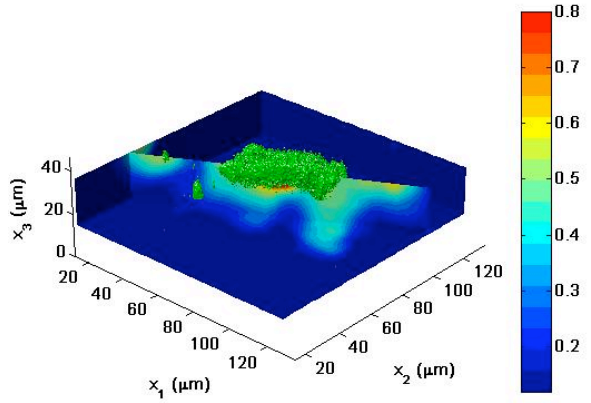

(c) Cell-induced displacements at $t_3 = 105$ min

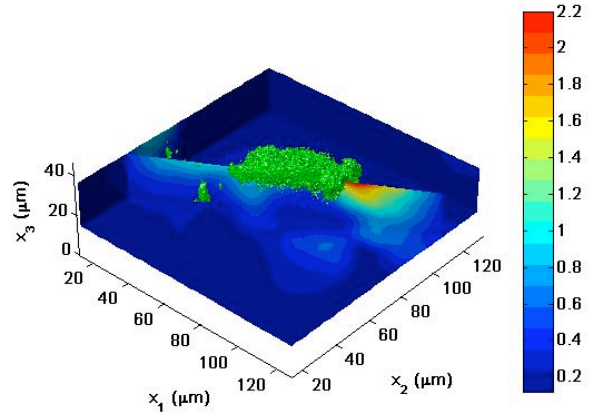

(d) Cell-induced displacements at $t_4 = 140$ min

Figure 4.16: Arbitrary displacement contour slices along the long axis of the cell. The slices of displacement contours underneath migrating cells show significant deformation in the normal plane that decay along the thickness of the sample. The two edges in the image are included to show that there are negligible displacements detected from neighboring cells (contours are dark blue). The color bar represents the magnitude of the total three-dimensional displacement vectors in μm, and the cell (green) is superimposed on the three-dimensional contour plots to show its position with respect to the deformation field.

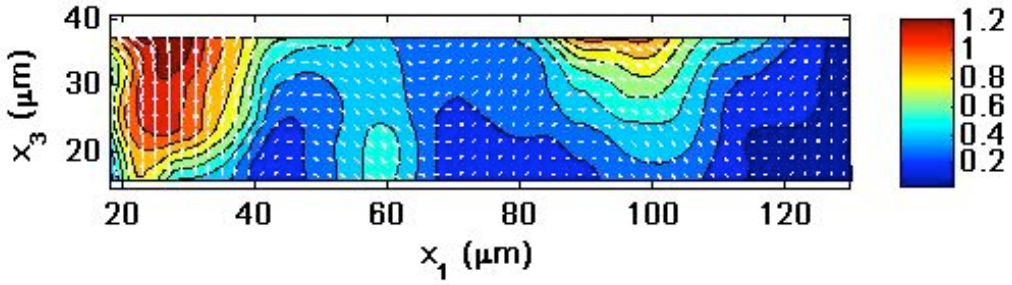

(a) Cross-sectional displacement contour plot through the substrate thickness at $t_1 = 35$ min

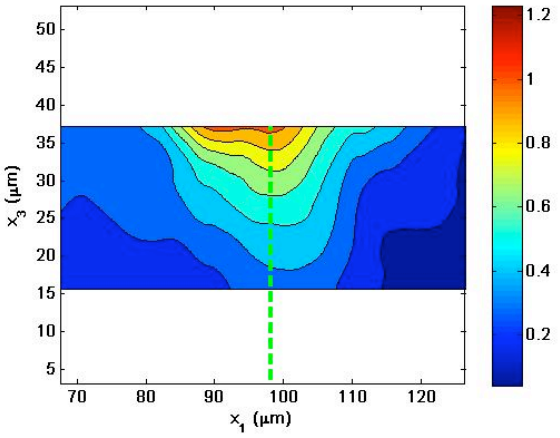

(b) Enlarged view of the contour plot in 4.17(a) and location of displacement line plot shown in 4.17(c)

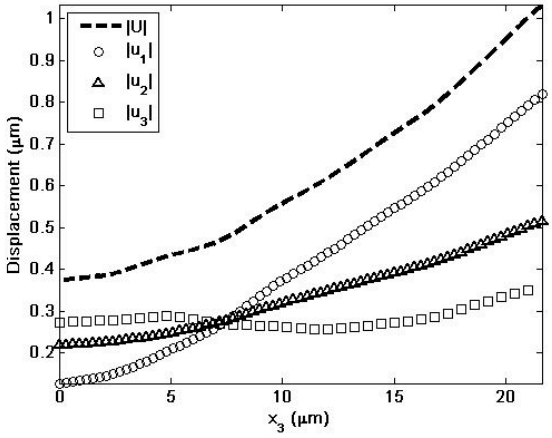

(c) Displacement line profile through the thickness of the gel (x_3). The maximum x_3 value corresponds to the gel surface.

Figure 4.17: Displacement contour and line plot profiles as a function of depth (x_3) through the thickness of the gel. Figure 4.17(a) shows the same displacement contours along the long axis of the cell as shown in Fig. 4.16(a), where the color bar represents the magnitude of the three-dimensional displacement vectors in μm, and the white arrows show the direction of the in-plane (u_1,u_3) displacement components only. Figure 4.17(b) shows the zoom-in image of Fig. 4.17(a), whereas Fig. 4.17(c) illustrates the decay of all three displacement components and the magnitude of the three-dimensional displacement vector in the x_3 direction.

decays approximately as $x_3^{3/2}$, the magnitude of the individual displacement components highlights the importance of the u_3 component at that particular time increment (t_1). Figure 4.18 displays the displacement distribution along the same arbitrary plane as in Fig. 4.17 for the next time increment $t_2 = 70$ min. Figure 4.18(a) shows the magnitude of the three-dimensional displacement vector as color contours along the same planar slice, while the white arrows represent the (u_3, u_1) displacement components. The color bar displays the units in μm, whereas the magnitude of the longest arrow corresponds to 0.6 μm. Figure 4.17(b) plots an enlarged picture of Fig. 4.17(a), highlighting an arbitrarily chosen location to generate a line profile of each displacement component as a function of depth (x_3), which is shown in Fig. 4.17(c). The displacement contour and line profiles show a similar decay with thickness than presented in Fig. 4.17 at time t_1.

Figures 4.19 and 4.20 display the surface displacement fields presented in Figs. 4.15(a) and 4.15(b) in more detail. In particular, Fig. 4.19(a) shows the magnitude of the three-dimensional displacement vector as color contours directly underneath the migrating cell, while the white arrows represent the (u_1, u_2) displacement components. The color bar displays the units in μm, whereas the magnitude of the longest arrow corresponds to 1.4 μm. Figure 4.19(b) plots an enlarged picture of Fig. 4.19(a), highlighting an arbitrarily chosen location to generate a line profile of each displacement component as a function of spatial distance, which is shown in Fig. 4.17(c). The displacement distribution is primarily dominated by the in-plane displacements with the u_3 displacement component showing its highest values at the periphery of the line profile. This particular displacement trend for the u_3 component is also observed in the *softer* substrate materials (see Fig. 4.5 and 4.6).

Figure 4.20(a) shows the same series of plots as Fig. 4.19(a) for the next time increment ($t_2 =$ 70 min). The color contours display the magnitude of the three-dimensional displacement vector underneath the fibroblast, while the white arrows represent the (u_1, u_2) displacement components. The color bar displays the units in μm, whereas the magnitude of the longest arrow corresponds to 1.8 μm. Figure 4.20(b) plots an enlarged picture of Fig. 4.20(a), highlighting an arbitrarily chosen location to generate a line profile of each displacement component as a function of spatial distance, which is shown in Fig. 4.17(c). The line profiles for both Figs. 4.17(c) and 4.18(c) were chosen at

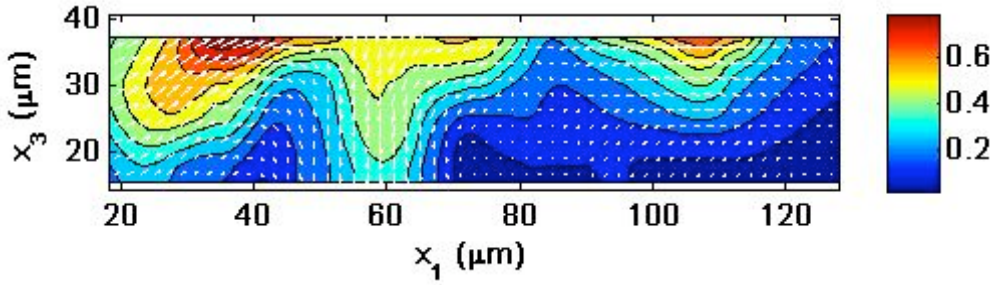

(a) Cross-sectional displacement contour plot through the substrate thickness at $t_2 = 70$ min

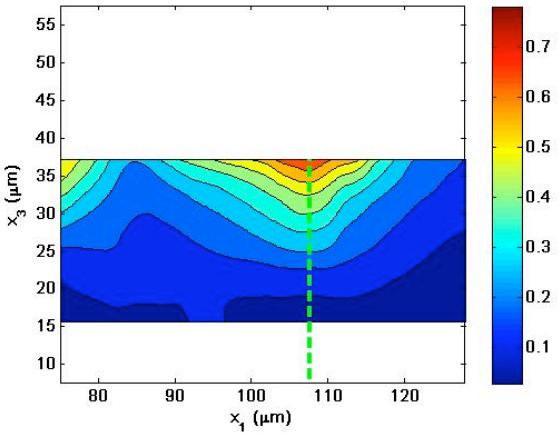

(b) Enlarged view of the contour plot in 4.18(a) and location of displacement line plot shown in 4.18(c)

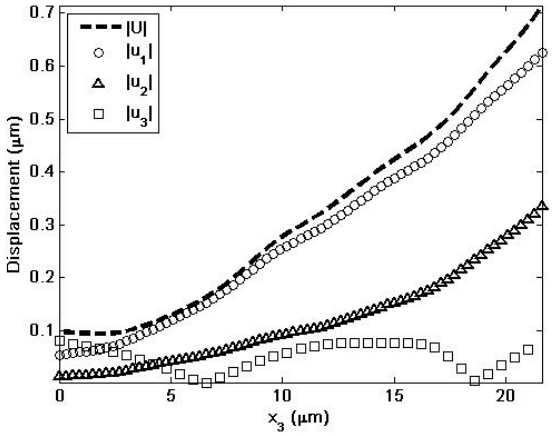

(c) Displacement line profile through the thickness of the gel (x_3). The maximum x_3 value corresponds to the gel surface.

Figure 4.18: Displacement contour and line plot profiles as a function of depth (x_3) through the thickness of the gel. Part 4.18(a) shows the same displacement contours along the long axis of the cell as shown in Fig. 4.16(b), where the color bar represents the magnitude of the three-dimensional displacement vectors in μm, and the white arrows show the direction of the in-plane (u_1,u_3) displacement components only. Figure 4.18(b) shows the zoom-in image of Fig. 4.18(a), whereas Fig. 4.18(c) illustrates the decay of all three displacement components and the magnitude of the three-dimensional displacement vector in the x_3 direction.

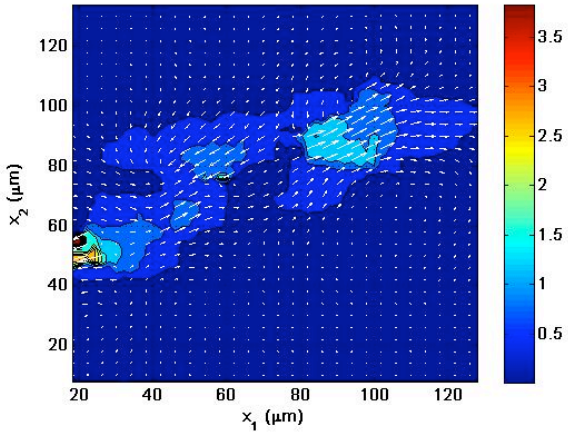

(a) Surface displacement contour plot underneath the migrating cell at $t_1 = 35$ min

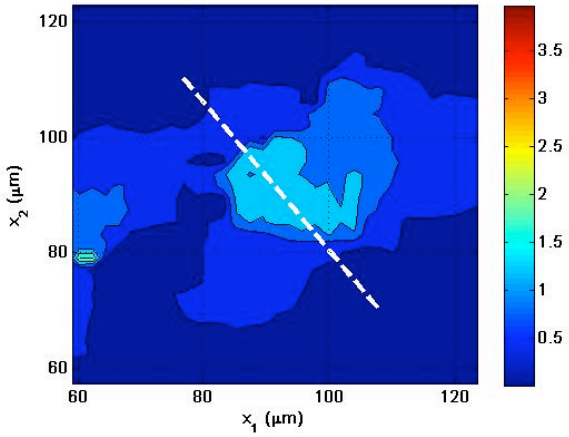

(b) Enlarged view of the contour plot in 4.5(a) and location of displacement line plot shown in 4.19(c)

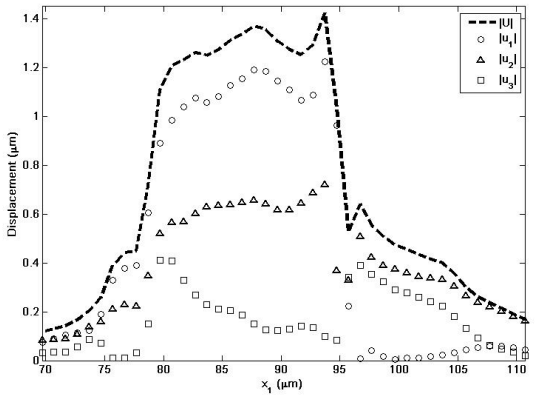

(c) Displacement profile along the selected line in 4.5(b)

Figure 4.19: Surface displacement contour and line plot profiles along a particular line in the $x_1 - x_2$ top surface plane at $t_1 = 35$ min. Figure 4.19(a) shows the same displacement contours as shown in Fig. 4.15(a), where the color bar represents the magnitude of the three-dimensional displacement vectors in μm, and the white arrows show the direction of the in-plane (u_1,u_2) displacement components only. Figure 4.19(b) shows the zoom-in image of Fig. 4.19(a) highlighting the particular region, where the line plot was generated. Figure 4.19(c) illustrates the distribution of all three displacement components and the magnitude of the three-dimensional displacement vector along the drawn line.

the leading edge of the motile cell. Comparing the contour plots and in particular the line profile plots, Fig. 4.18(c) shows a a narrower, Gaussian-like displacement distribution profile as compared to Fig. 4.17(c).

Figure 4.21 compares the surface displacement fields directly underneath the migrating cells shown in Fig. 4.15(a) and 4.15(b) by highlighting the contribution of the u_3 displacement component. Figures 4.21(a) and 4.21(c) show the displacement contours of the magnitude of the three-dimensional displacement vector whereas Figs. 4.21(b) and 4.21(d) display the magnitude of only the two-dimensional (u_1, u_2) displacement vectors. Side-by-side comparison reveals that most of the deformation occurs in-plane (u_1, u_2), however there are particular areas where the u_3 proves to be significant. These areas are found along the periphery of the maximum displacement peaks, which is also observed in Figs. 4.19(c) and 4.20(c).

4.5 Three-Dimensional Tractions During Cell Migration on Stiff Substrates

This section presents the traction calculation based upon the measured displacement field reported in Section 4.4. Following the same error analysis as in Section 4.3 the technique is sensitive to stresses and tractions that are greater than 80 Pa or 80 pN/μm^2. All of the subsequently presented Figs. are from the same data set as the displacement results reported in Section 4.4.

Figure 4.22 shows a time evolution of the cell surface tractions during migration over a time span of 140 min. The color contour plots display the magnitude of the three-dimensional traction vector in $pN/\mu m^2$. Again, the linear dimension of the cell in all of the plots is approximately 80 - 100 μm. The direction of cell migration is from the left to the right. The localized nature of the tractions is clearly visible in all time frames. As described earlier, due to the degradation of the actin-fluorescent cell stain (GFP-actin), the cell's outline is not always visible directly above some of the stress concentration locations, although the cell is still transmitting force there, as has been confirmed through multiple experiments where GFP-actin was clearly visible.

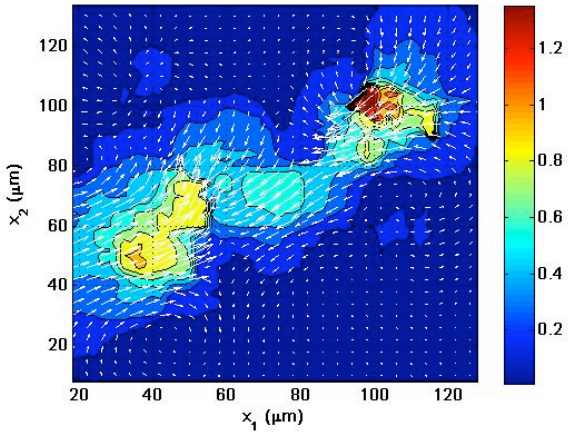

(a) Surface displacement contour plot underneath the migrating cell at $t_2 = 70$ min

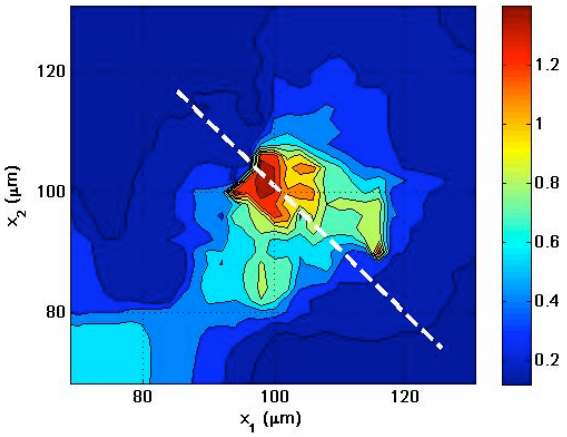

(b) Enlarged view of the contour plot in 4.6(a) and location of displacement line plot shown in 4.20(c)

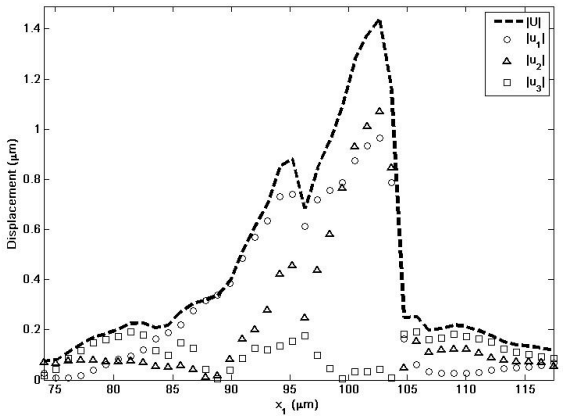

(c) Displacement profile along the selected line in 4.6(b)

Figure 4.20: Surface displacement contour and line plot profiles along a particular line in the $x_1 - x_2$ top surface plane at $t_2 = 70$ min. Figure 4.20(a) shows the same displacement contours as shown in Fig. 4.15(b), where the color bar represents the magnitude of the three-dimensional displacement vectors in μm, and the white arrows show the direction of the in-plane (u_1,u_2) displacement components only. Figure 4.19(b) shows the zoom-in image of Fig. 4.20(a) highlighting the particular region, where the line plot was generated. Figure 4.20(c) illustrates the distribution of all three displacement components and the magnitude of the three-dimensional displacement vector along the drawn line.

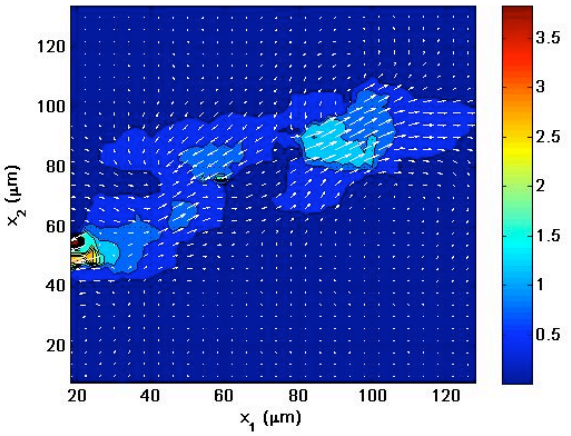

(a) Cell-induced surface displacements (3D) at $t_1 = 35$ min

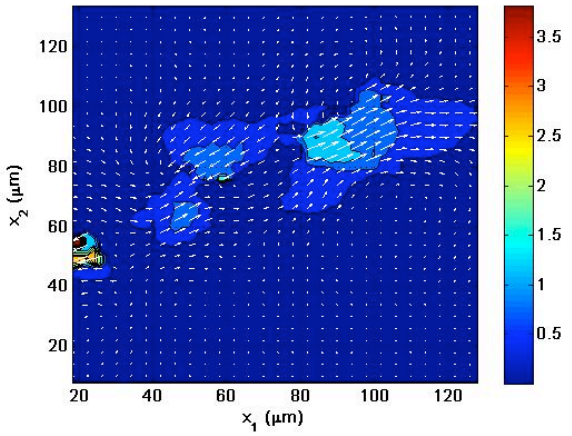

(b) Cell-induced surface displacements (2D) at $t_1 = 35$ min

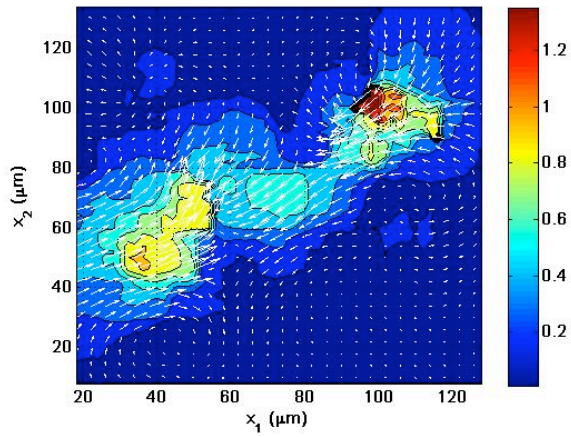

(c) Cell-induced surface displacements (3D) at $t_2 = 70$ min

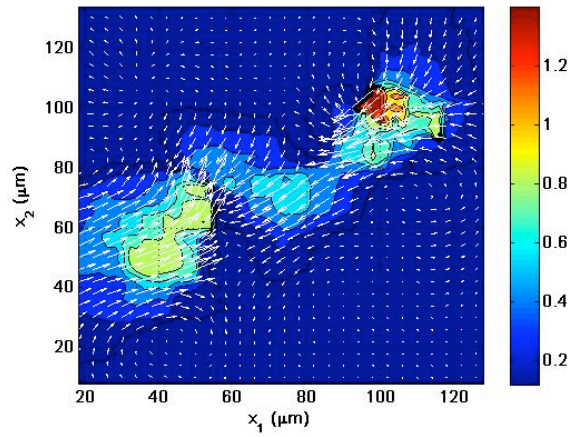

(d) Cell-induced surface displacements (2D) at $t_2 = 70$ min

Figure 4.21: Comparison between the displacement magnitude of all three-dimensional vector components (4.21(a) and 4.21(c)) and the magnitude of the two-dimensional vector components only (4.21(b) and 4.21(d)). The color bar is displaying all displacement values in μm, and and the white arrows show the direction of the in-plane (u_1,u_2) displacement components only.

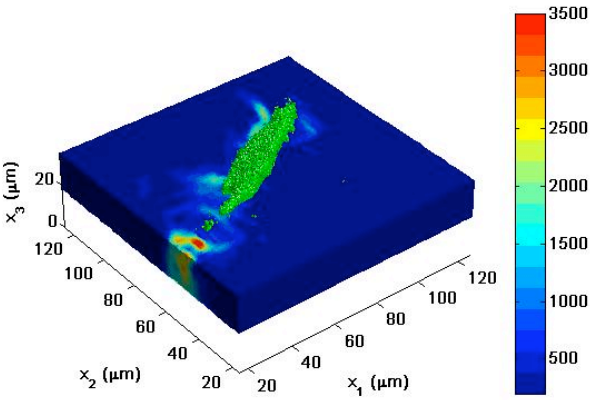

(a) Cell-induced surface tractions at $t_1 = 35$ min

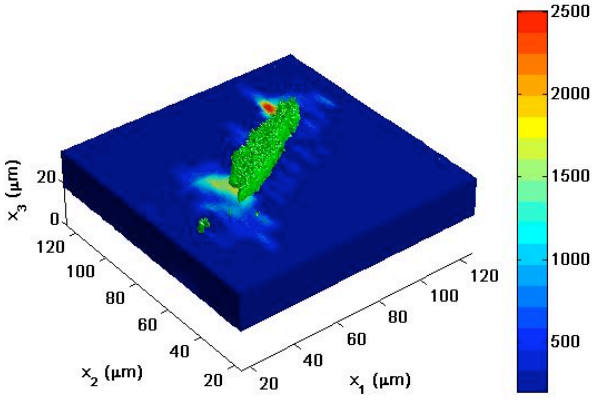

(b) Cell-induced surface tractions at $t_2 = 70$ min

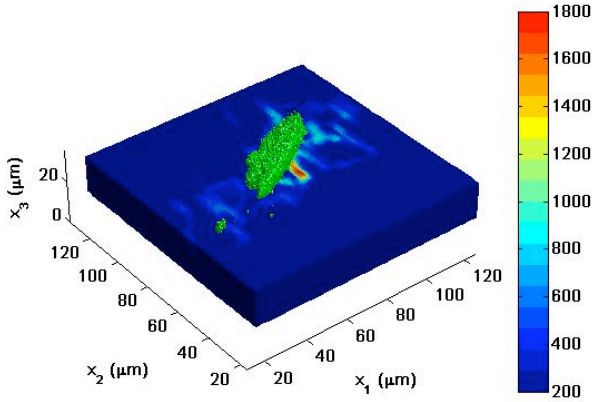

(c) Cell-induced surface tractions at $t_3 = 105$ min

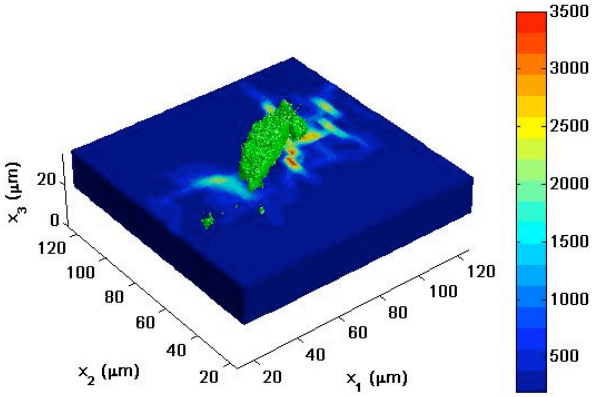

(d) Cell-induced surface tractions at $t_4 = 140$ min

Figure 4.22: Surface contour plots of the magnitude of the three-dimensional traction vector during cell migration. The color bar represents the magnitude of the total three-dimensional surface traction vectors with units in $pN/\mu m^2$, and the cell (green) is superimposed on the three-dimensional contour plots to show its position with respect to the traction field.

Figure 4.23 shows the time evolution of the traction field along an arbitrary slice beneath the migration cell's long axis over a time span of 140 min. The tractions acting along the shown plane were calculated as previously described (see Section 4.3). The decay of the magnitude of the three-dimensional traction vector is shown for the same time series as in Fig. 4.22. The color contour plots display the magnitude of the three-dimensional traction vector in $pN/\mu m^2$. The traction contour slices highlight the dynamic interaction of the cell with its substrate, characterized by changes in magnitudes and location of the observed tractions. It should be noted that in all Figs. the actual cell outline most likely extends further than is shown by the green rendered cell, where the GFP-actin is degraded as explained earlier.

Figure 4.24 examines the traction field of the arbitrary planar slice in Fig. 4.23(a) in more detail. Figure 4.24(a) shows the magnitude of the three-dimensional traction vector as color contours along the same planar slice, while the white arrows represent the (T_3, T_1) traction vector components. The color bar displays the units in $pN/\mu m^2$, whereas the magnitude of the longest arrow corresponds to 3000 $pN/\mu m^2$. Figure 4.24(b) plots an enlarged picture of Fig. 4.10(a), highlighting an arbitrarily chosen location to generate a line profile of each traction component as a function of depth (x_3), which is shown in Fig. 4.24(c). The decay of the total traction vector appears to have two linear regimes, one being dominated by the T_3 component closer to the surface of the gel, and one farther away from the surface, where T_1 contributes most significantly.

Figure 4.25 displays the traction distribution along the same arbitrary plane as in Fig. 4.24 for the next time increment $t_2 = 70$ min. Figure 4.25(a) shows the magnitude of the three-dimensional traction vectors as color contours along the same planar slice, while the white arrows represent the (T_3, T_1) traction components. The color bar displays the units in $pN/\mu m^2$, whereas the magnitude of the longest arrow corresponds to 680 $pN/\mu m^2$. Figure 4.25(b) plots an enlarged picture of Fig. 4.25(a), highlighting an arbitrarily chosen location to generate a line profile of each traction component as a function of depth (x_3), which is shown in Fig. 4.25(c). The traction contours and line profiles show a similar decay with thickness as presented in Fig. 4.24, however, in Fig. 4.25(c) T_3 dominates the total traction vector throughout the entire imaged gel thickness, whereas the in-plane

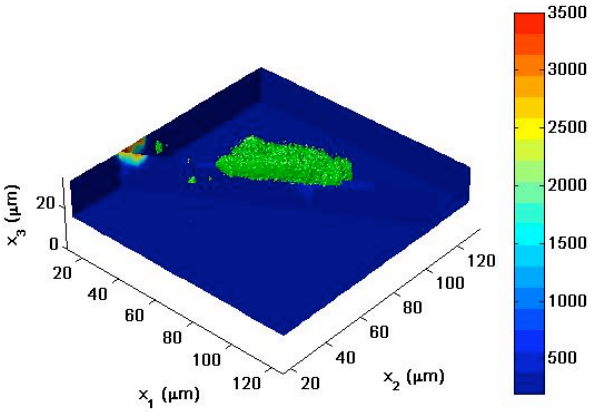

(a) Cell tractions at $t_1 = 35$ min

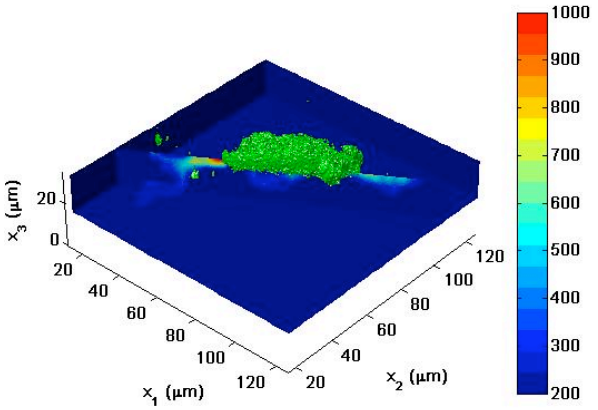

(b) Cell tractions at $t_2 = 70$ min

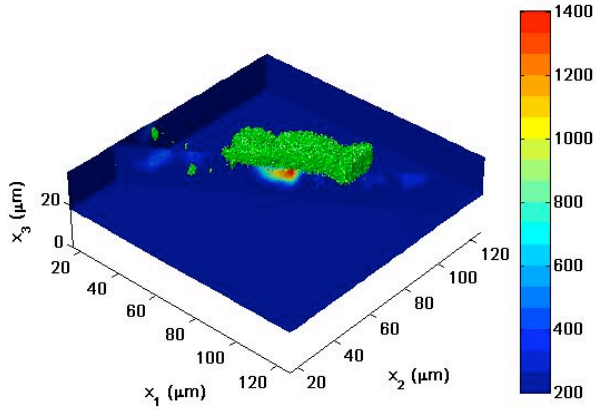

(c) Cell tractions at $t_3 = 105$ min

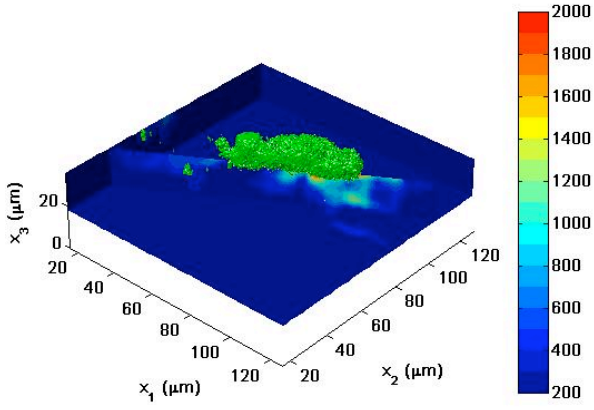

(d) Cell tractions at $t_4 = 140$ min

Figure 4.23: Arbitrary traction contour slices along the long axis of the cell. The color bar indicates the magnitude of the three-dimensional traction vectors along that particular plane in units of $pN/\mu m^2$. The slices of the traction contours underneath migrating cells correspond to the displacement slices shown in Fig. 4.16. The two edges in the image are included to show that there are negligible tractions detected from neighboring cells (contours are dark blue). The cell (green) is superimposed on the three-dimensional contour plots to show its position with respect to the traction field.

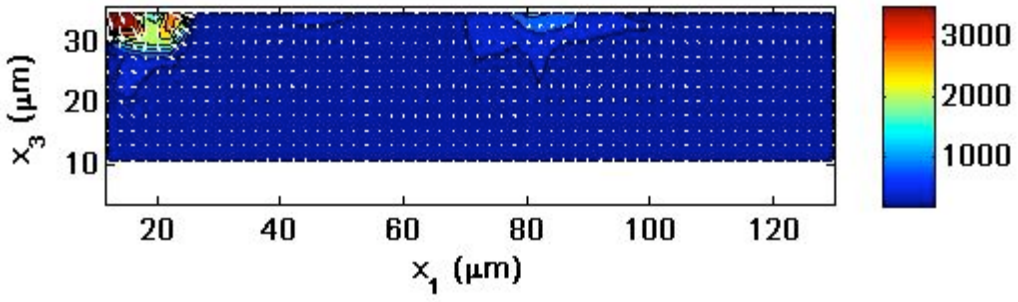

(a) Cross-sectional tractions contour plot through the substrate thickness at $t_1 = 35$ min

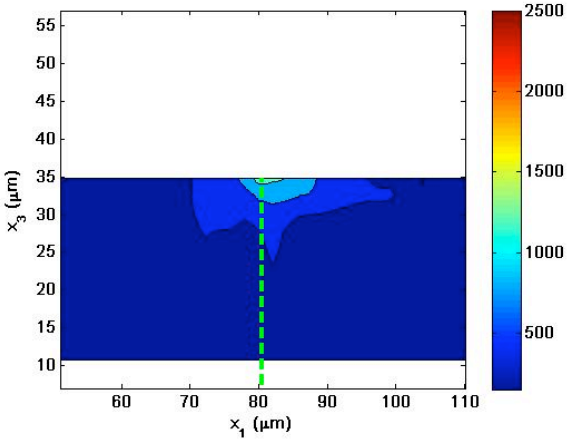

(b) Enlarged view of the contour plot in 4.24(a) and the location of the traction line plot shown in 4.24(c)

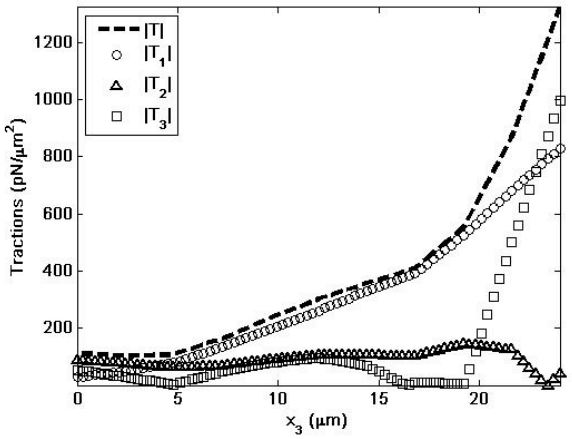

(c) Traction force line profile through the thickness of the gel (x_3). The maximum x_3 value corresponds to the gel surface.

Figure 4.24: Traction contour and line plot profiles as a function of depth (x_3) through the thickness of the gel at time $t_1 = 35$ min. Figure 4.24(a) shows the same traction contours along the long axis of the cell as shown in Fig. 4.23(a), where the color bar represents the magnitude of the three-dimensional traction vectors along that particular plane, and the white arrows show the direction of the in-plane (T_1,T_3) traction components only. Figure 4.24(b) shows the zoom-in image of Fig. 4.24(a), whereas Fig. 4.24(c) illustrates the decay of all traction components and the magnitude of the three-dimensional traction vector in the x_3 direction. All color bar units are $pN/\mu m^2$.

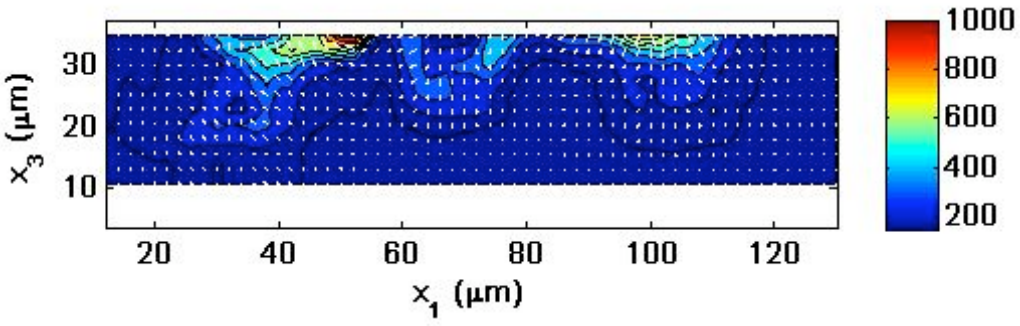

(a) Cross-sectional tractions contour plot through the substrate thickness at $t_1 = 70$ min

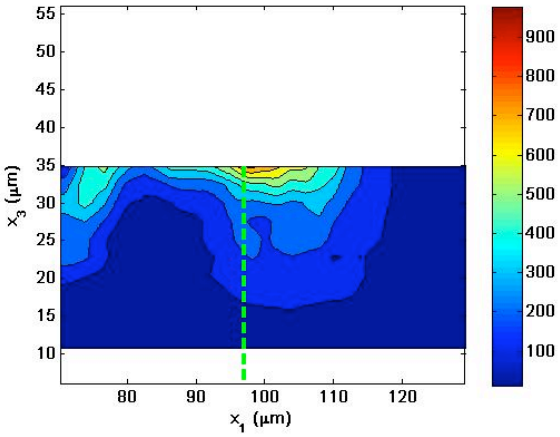

(b) Enlarged view of the contour plot in 4.11(a) and the location of the traction line plot shown in 4.25(c)

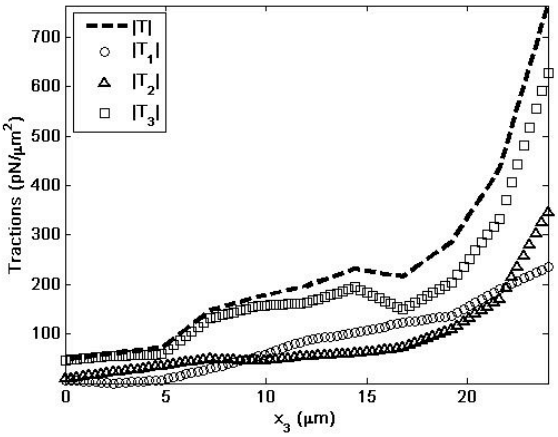

(c) Traction line profile through the thickness of the gel (x_3). The maximum x_3 value corresponds to the gel surface.

Figure 4.25: Traction contour and line plot profiles as a function of depth (x_3) through the thickness of the gel at time $t_2 = 70$ min. Figure 4.25(a) shows the same traction contours along the long axis of the cell as shown in Fig. 4.23(b), where the color bar represents the magnitude of the three-dimensional traction vectors along that particular plane, and the white arrows show the direction of the in-plane (T_1,T_3) traction components only. Figure 4.25(b) shows the zoom-in image of Fig. 4.25(a), whereas Fig. 4.25(c) illustrates the decay of all traction components and the magnitude of the three-dimensional traction vector in the x_3 direction. All color bar units are $pN/\mu m^2$.

components T_1 and T_2 contribute primarily on the surface of the gel to $|\mathbf{T}|$, the magnitude of the total traction vector.

Figures 4.26(a) and 4.27(a) display the surface traction fields presented in Figs. 4.22(a) and 4.22(b) in more detail. In particular, Fig. 4.19(a) shows the magnitude of the three-dimensional traction vectors as color contours directly underneath the migrating cell, while the white arrows represent the (T_1, T_2) traction components. The color bar displays the units in $pN/\mu m^2$, whereas the magnitude of the longest arrow corresponds to 2730 $pN/\mu m^2$. Figure 4.26(b) plots an enlarged picture of Fig. 4.26(a), highlighting an arbitrarily chosen location to generate a line profile of each traction component as a function of spatial distance, which is shown in Fig. 4.26(c). All three traction components display a similar behavior in that they attain there maximum along the same spatial position ($x_1 = 89\ \mu m$).

Figure 4.27(a) shows the same series of plots as Fig. 4.26(a) for the next time increment (t_2 = 70 min). The color contours display the magnitude of the three-dimensional traction vectors underneath the fibroblast, while the white arrows represent the (T_1, T_2) traction components. The color bar displays the units in $pN/\mu m^2$, whereas the magnitude of the longest arrow corresponds to 1000 $pN/\mu m^2$. Figure 4.27(b) plots an enlarged picture of Fig. 4.13(a), highlighting an arbitrarily chosen location to generate a line profile of each traction component as a function of spatial distance, which is shown in Fig. 4.17(c). The line profiles in Figs. 4.17(c) and 4.27(c) were chosen at the leading edge of the motile cell. Comparing the contour plots, and in particular the two line profile plots, Fig. 4.26(c) shows a broader traction profile than Fig. 4.27(c).

Figure 4.28 compares the surface traction fields directly underneath the migrating cells shown in Fig. 4.22(a) and 4.22(b) by highlighting the contribution of the T_3 traction component. Figures 4.28(a) and 4.28(c) show surface contours of the magnitude of the three-dimensional traction vectors whereas Figs. 4.28(b) and 4.28(d) display the magnitude of only the two-dimensional, in-plane (T_1, T_2) traction vectors. Side-by-side comparison reveals that the cell applies mostly in-plane shear tractions (T_1, T_2). Over the course of the shown time increments t_1 and t_2 the contribution of the T_3 traction component as shown in Figs. 4.26(c) and 4.27(c) is relatively insignificant.

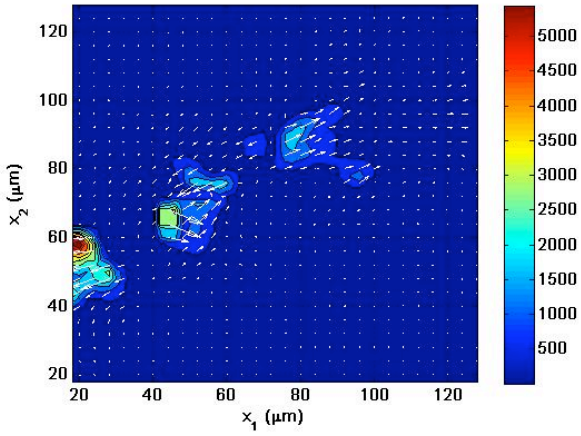

(a) Surface tractions contour plot underneath the migrating cell at $t_1 = 35$ min

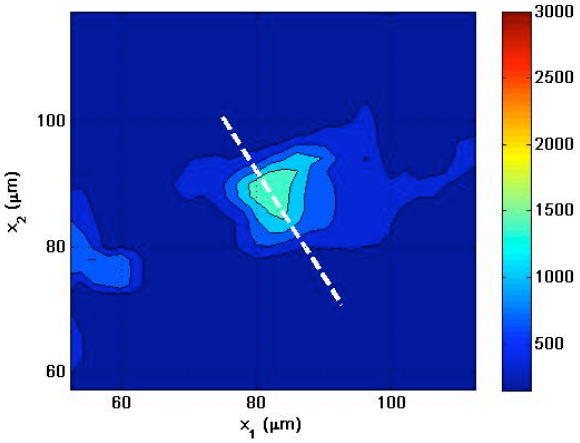

(b) Enlarged view of the contour plot in 4.26(a) and the location of the traction line plot shown in 4.26(c)

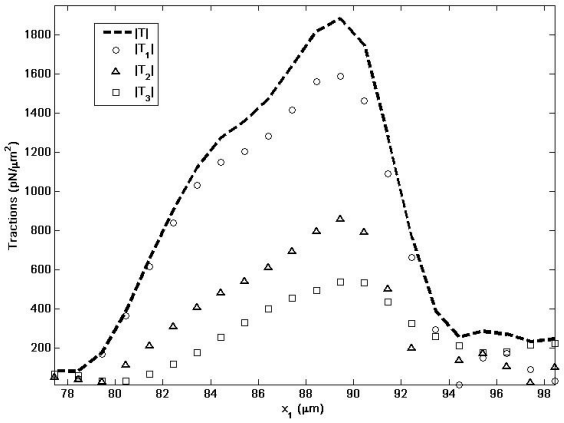

(c) Traction profile along the selected line in 4.26(b)

Figure 4.26: Surface traction contour and line plot profiles along a particular line in the $x_1 - x_2$ top surface plane at $t_1 = 35$ min. Figure 4.26(a) shows the same traction contours as shown in Fig. 4.22(a), where the color bar represents the magnitude of the three-dimensional surface traction vectors and the white arrows show the direction of the in-plane (T_1,T_2) traction components only. The color bar units represent $pN/\mu m^2$. Figure 4.19(b) shows the zoom-in image of Fig. 4.26(a) highlighting the particular region, where the line plot was generated. Figure 4.26(c) illustrates the distribution of all three traction components and the magnitude of the three-dimensional traction vector along the drawn line.

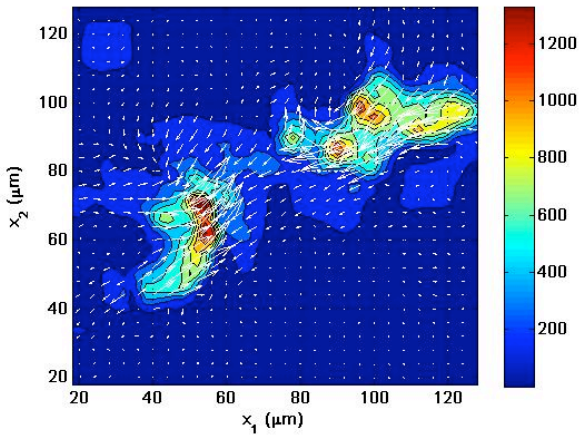

(a) Surface tractions contour plot underneath the migrating cell at $t_2 = 70$ min

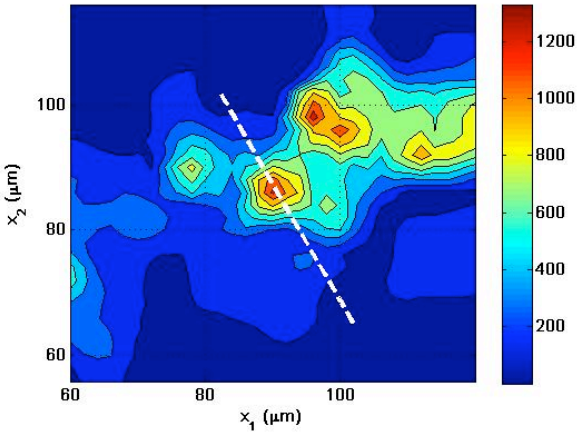

(b) Enlarged view of the contour plot in 4.27(a) and the location of the traction line plot shown in 4.27(c)

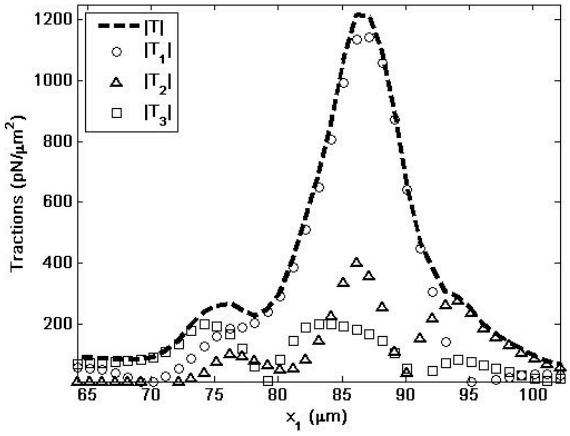

(c) Traction profile along the selected line in 4.27(b)

Figure 4.27: Surface traction contour and line plot profiles along a particular line in the $x_1 - x_2$ surface plane at $t_2 = 70$ min. Figure 4.27(a) shows the same traction contours as shown in Fig. 4.22(b), where the color bar represents the magnitude of the three-dimensional surface traction vectors and the white arrows show the direction of the in-plane (T_1,T_2) traction components only. The color bar units represent $pN/\mu m^2$. Figure 4.6(b) shows the zoom-in image of Fig. 4.27(a) highlighting the particular region, where the line plot was generated. Figure 4.27(c) illustrates the distribution of all three traction components and the magnitude of the three-dimensional traction vector along the drawn line.

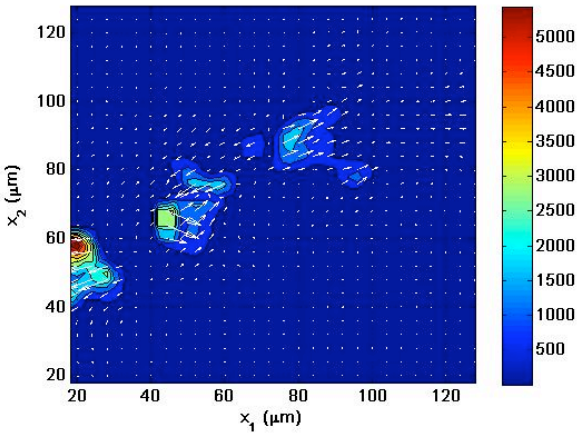

(a) Cell-induced surface tractions (3D) at $t_1 = 35$ min

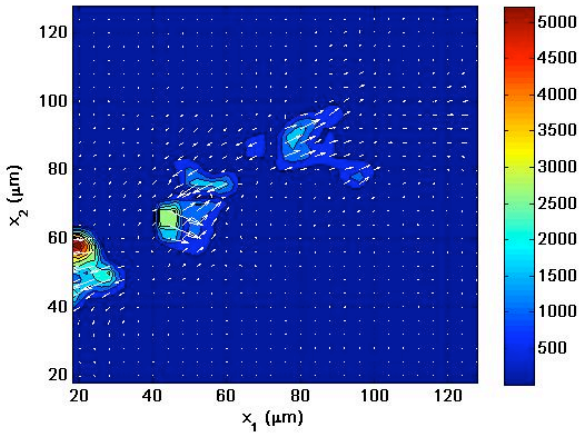

(b) Cell-induced surface tractions (2D) at $t_1 = 35$ min

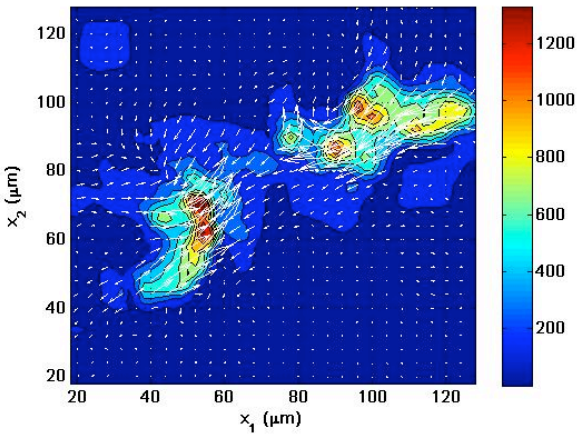

(c) Cell-induced surface tractions (3D) at $t_2 = 70$ min

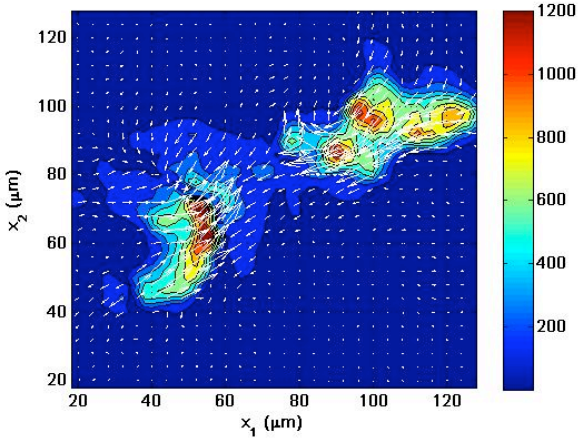

(d) Cell-induced surface tractions (2D) at $t_2 = 70$ min

Figure 4.28: Comparison between the magnitude of the three-dimensional traction vector (4.28(a) and 4.28(c) and the magnitude of the two-dimensional traction vector (T_1, T_2) components only (4.28(b) and 4.28(d))). The color bar is displaying all traction values in $pN/\mu m^2$, and and the white arrows show the direction of the in-plane (T_1,T_2) traction components only.

4.6 Inhibiting Cell Contractility and Cell Locomotion

In order to conclude that the experimentally observed displacements are indeed caused by cell-mediated forces, cell displacements were monitored before and after the cells were treated with a myosin II blocker. This blocker protein, blebbistatin (Sigma-Aldrich, St. Louis, MO), inhibits the myosin II molecular motor proteins from moving along the cell's actin filaments to cause cytoskeletal contraction. Blebbistatin is commonly used in traction or traction force measurements to inhibit actomyosin contraction in non-muscle cells [5, 6]. If the cell is unable to generate actomyosin based internal forces that are transmitted through focal adhesions to the substrate, then there should be be no evident substrate displacements. Hence, this experiment serves as a validation tool that the previously observed displacements are in fact cell-mediated, and are not due to thermal fluctuation or instrument noise. Confocal stacks of individual cells were captured 1-2 hours before treatment with 12.5 μM blebbistatin, and up to 4 hours post-treatment. Figures 4.29(a) - 4.29(d) show the resulting surface displacement fields before and after blebbistatin injection as displacement contours. The contours represent the magnitude of the three-dimensional displacement vectors, whereas the white arrows indicate the in-plane (u_1,u_2) displacements only. The color bar is indicating all values in μm. Figure 4.29(e) shows the average maximum surface displacements achieved by a single cell at time points before and after blebbistatin injection. Following the treatment, there is a notable decrease in the average maximum displacement. Despite the cell's presence, there are no detectable displacements after 35 minutes. Identical experiments performed without cells and in the presence of blebbistatin yielded no notable displacements, establishing that all measured displacements are cell-induced.

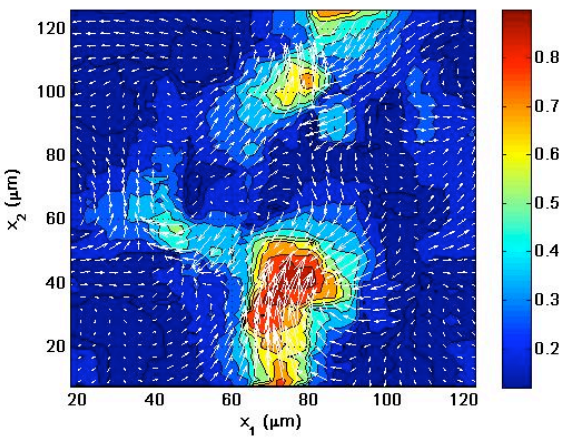

(a) Cell-induced surface displacements before blebbistatin treatment

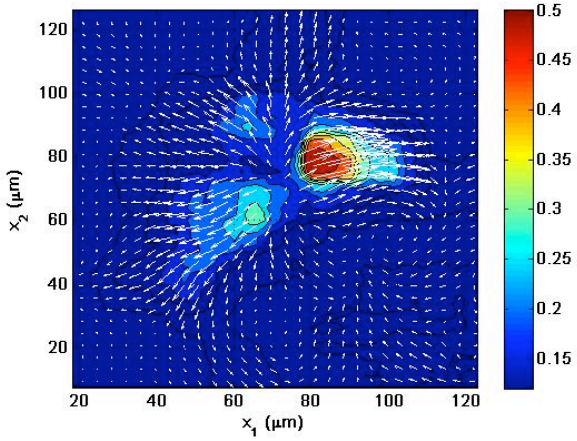

(b) Cell-induced surface displacements at blebbistatin injection

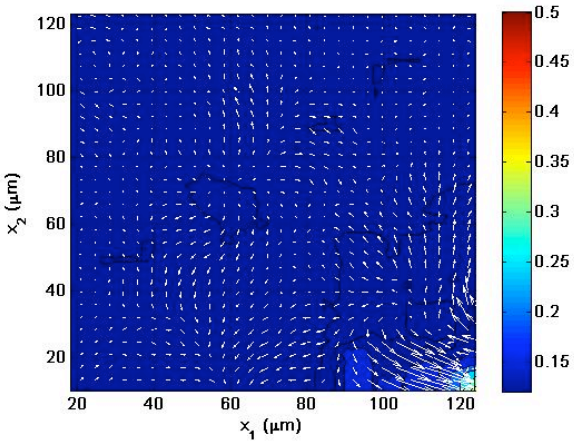

(c) Cell-induced surface displacements 35 min after treatment

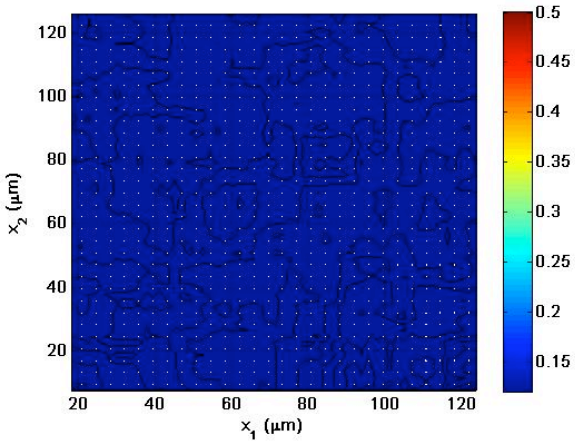

(d) Cell-induced surface displacements 245 min after treatment

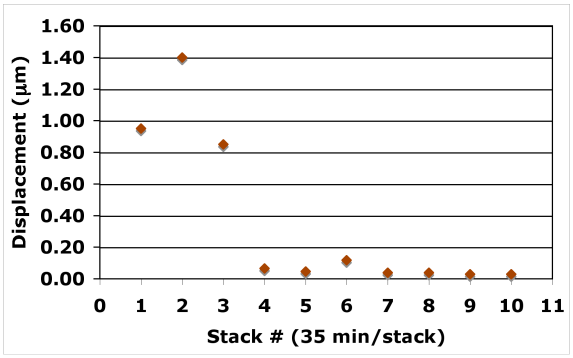

(e) Plot of the average maximum observed cell-induced surface displacement before and after treatment with blebbistatin. (blebbistatin injection occured at stack #3.)

Figure 4.29: Successive time series of cell-induced surface displacements before (4.29(a) and 4.29(b)) and after treatment with blebbistatin (4.29(c) and 4.29(d)). Color contours display the magnitude of the three-dimensional displacement vector, while the white arrows show the direction of the in-plane (u_1,u_2) displacement components only. The color bar represents all values in μm.

4.7 Comparison of Cell Response on Soft and Stiff Substrates

Comparing the magnitude of the measured displacement fields on *soft* and *stiff* substrates shows similar values (same order of magnitude) during cell migration, suggesting that the cell actively regulates the amount of force needed to generate enough surface displacements. Figures 4.30 and 4.31 show that while the magnitudes of the surface displacement on *soft* and *stiff* substrates display values of the same magnitude order, the tractions are different by approximately a factor of ten. The ratio of the *soft* and *stiff* substrate material Young's moduli is also approximately ten, which suggests that the cell tractions scale linearly with the Young's moduli of the substrates studied here. This trend is noticable throughout all of the experiments performed on both substrates, and this scaling behavior has been observed previously [3].

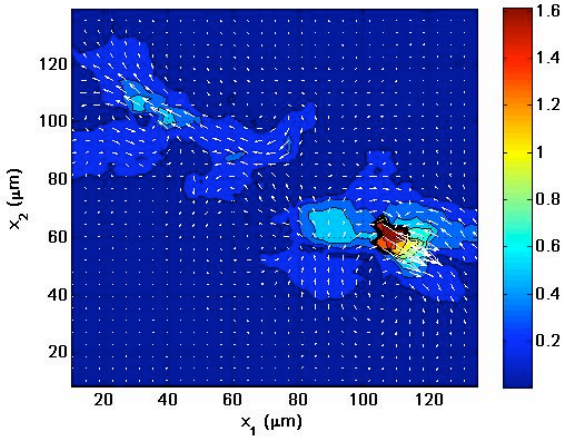

(a) Cell-induced surface displacements on *soft* polyacrylamide gels at $t_1 = 35$ min

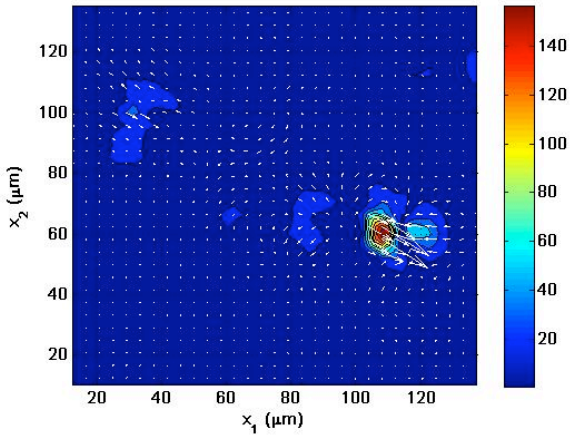

(b) Cell-induced surface tractions on *soft* polyacrylamide gels at $t_1 = 35$ min

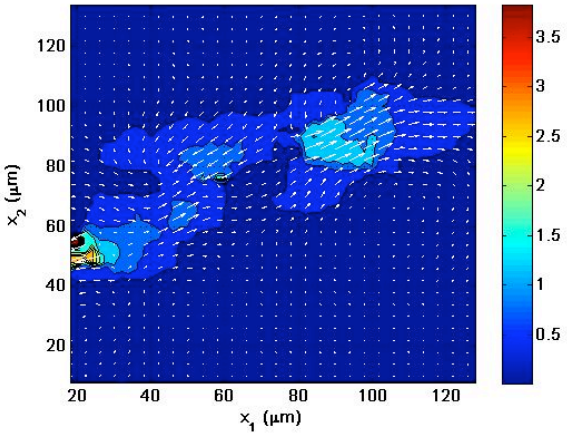

(c) Cell-induced surface displacements on *stiff* polyacrylamide gels at $t_1 = 35$ min

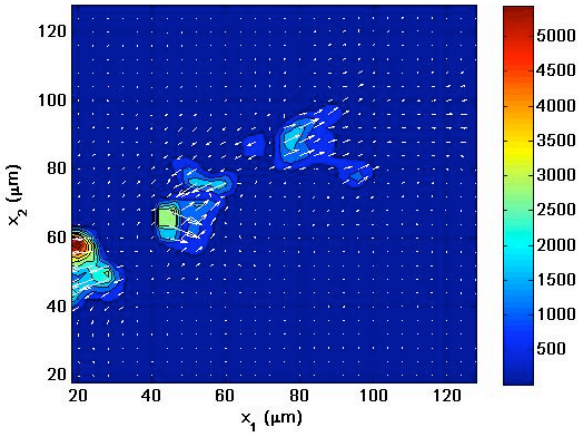

(d) Cell-induced surface tractions on *stiff* polyacrylamide gels at $t_1 = 35$ min

Figure 4.30: Comparison between the three-dimensional cell induced surface deformation on *soft* (4.31(a) and 4.31(b)) and *stiff* (4.31(c) and 4.31(d)) polyacrylamide gel substrates for a 35 min time increment. The color bar in Figs. 4.31(a) and 4.31(c) indicates all values in μm, whereas the color bar in Figs. 4.31(b) and 4.31(d) displays all values in $pN/\mu m^2$. The Young's moduli of the *soft* and *stiff* substrates are 0.82 and 9.64 kPa, respectively.

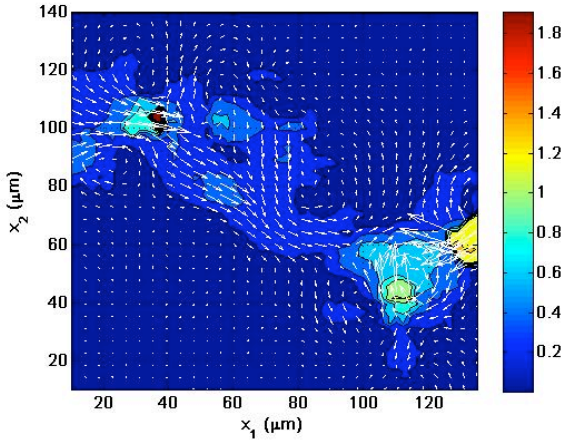

(a) Cell-induced surface displacements on *soft* polyacrylamide gels at $t_1 = 70$ min

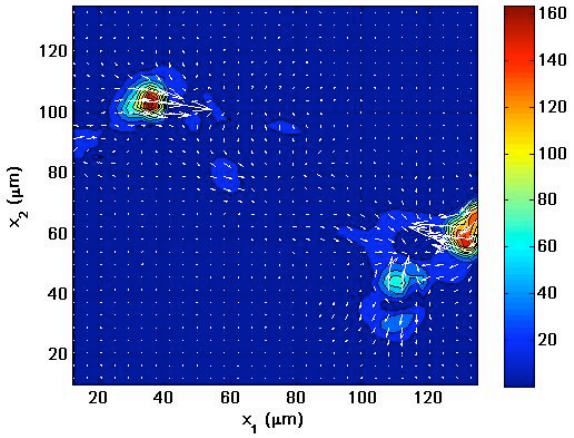

(b) Cell-induced surface tractions on *soft* polyacrylamide gels at $t_1 = 70$ min

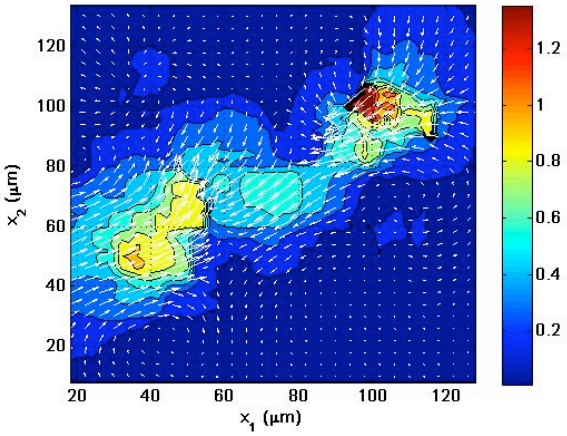

(c) Cell-induced surface displacements on *stiff* polyacrylamide gels at $t_1 = 70$ min

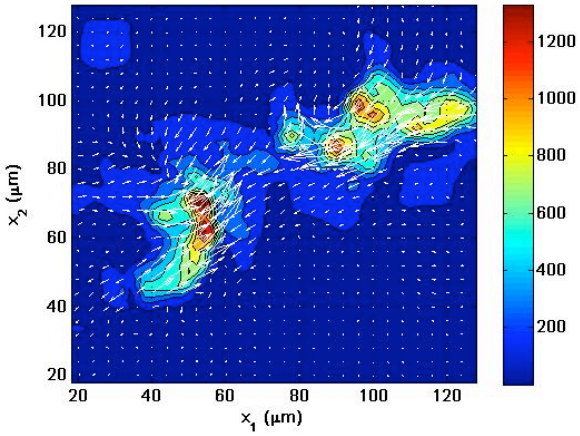

(d) Cell-induced surface tractions on *stiff* polyacrylamide gels at $t_1 = 70$ min

Figure 4.31: Comparison between the three-dimensional cell induced surface deformation on *soft* (4.31(a) and 4.31(b)) and *stiff* (4.31(c) and 4.31(d)) polyacrylamide gel substrates for a 35 min time increment. The color bar in Figs. 4.31(a) and 4.31(c) indicates all values in μm, whereas the color bar in Figs. 4.31(b) and 4.31(d) displays all measurements in $pN/\mu m^2$. The Young's moduli of the *soft* and *stiff* substrates are 0.82 and 9.64 kPa, respectively.

4.8 Implications of Three-dimensional Measurements for Current Cell Motility Models

The deformation results presented in Sections 4.2 - 4.5 highlight the strong three-dimensional dependence of cell-matrix interactions during cell migration. One important implication of these findings is in the context of cell motility models that are typically based on existing two-dimensional cell displacement and traction or traction force data. This section briefly reviews the basis of the most widely accepted motility model based on two-dimensional experimental data, and gives an outlook on a potential new cell migration mechanism based on the three-dimensional experimental observations presented here. It should be noted however, that the suggested migration mechanism outlined here is based on the results presented in the previous sections, and additional experiments are necessary to elucidate this further.

One of the most commonly accepted cell motility models describes the process of cell motion in four general steps, as illustrated in Fig. 4.32. The following is a summary of these steps, and further detailed information can be found elsewhere [2, 1]. The first step, as shown in Fig. 4.32(a), consists of the protrusion of actin fibers at the leading edge via actin polymerization. Typically, actin polymerization rates vary and can be different at either end leading to differential polymerization or treadmilling. This allows the cell to actively control the shape of its cytoskeleton. Next, the newly formed protrusion will engage the substrates through ligand-receptor connection (Fig. 4.32(b)), which generally involve the interplay of many focal adhesion proteins. This newly formed adhesion anchor site, or focal adhesion complex, will be utilized later by the cell to transmit forces to the substrate or matrix material. In step three, as shown in Fig. 4.32(c), the cell detaches from the trailing edge by possibly disassembling the focal adhesion complex. Finally, the cell generates an internal contractile force by the activation of actomyosin, and due to the imbalance of forces, propels itself forward, as illustrated in Fig. 4.32(d).

While this description of cell movement is oversimplified, the basic cell-generated tractions responsible for cell motion are thought to be only planar. However, as shown in the previous sections,

cell-induced displacements and tractions are not only planar but rather highly three-dimensional. This is further illustrated in Fig. 4.33, where the cell seems to undergo a sort of peeling or rolling motion during its movement from left to right. The leading edge of the cell is located towards the right end of the Fig., whereas the trailing edge is located towards the left end (also, see Figs. 4.15 - 4.23). The Fig. illustrates the progression of the in-plane (T_1) and normal (T_3) shear tractions underneath the long axis of the cell along the same arbitrarily selected slice as presented in Sections 4.4 and 4.5. The color contours display the magnitude of the three-dimensional traction vector, while the black arrows indicate the (T_1, T_3) shear traction components. The time series shows the evolution of the substrate shear tractions as the cell moves from the left to the right, suggesting a potential peeling mechanism. Examining the magnitude of each of the T_1 and T_3 components in Fig. 4.34 elucidates this mechanism in more detail. The in-plane (T_1) tractions seem to alternate between local contraction and extension close to force equilibrium, while the normal (T_3) tractions show a net moment around the center of the cell body in Figs. 4.34(a) and 4.34(e). This implies the cell is utilizing a more complex migration mechanism than previously thought, incorporating out-of-plane (normal) rotations along with in-plane contractions and extensions. Previous cell motility models primarily focused on the in-plane forces due to the lack of information in the third dimension, thus suggesting a purely in-plane "push-pull" hypothesis.

A potential analog to this observed mechanism is the rapid attachment and detachment of individual setae of a gecko's toe. These animals have the ability to generate large frictional and adhesion forces to climb steep inclines and vertical walls using van der Waals interactions between their spatulae that comprise the setae and the substrate material [50]. During the approach stage, the gecko's spatulae adhere to the substrate in an almost parallel configuration with minimal adhesive force. Then, the gecko "rolls" and "grips" its toes inward generating large frictional (in-plane) and adhesion (normal) forces. The final step involves a "rolling-out" process, in which the gecko peels its spatulae off the substrate surface from rear to front. The experimental findings presented here reveal new insights into the cell's complex migration machinery and should provide an impetus for the development of new three-dimensional cell motility models.

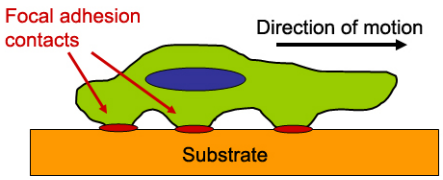

(a) Protrusion of the leading edge through actin polymerization

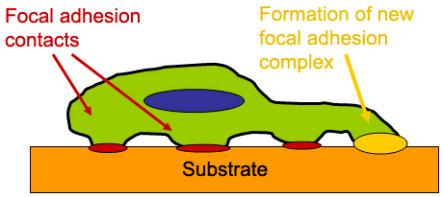

(b) Adhesion at the leading edge

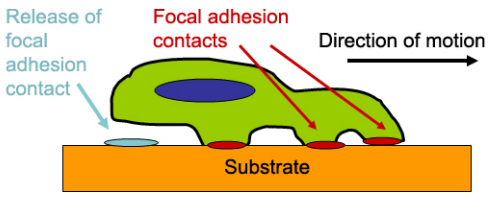

(c) Detachment at the trailing edge

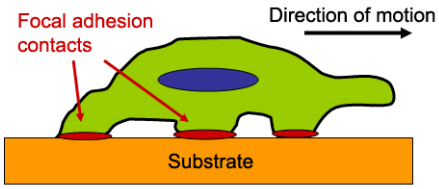

(d) Cell contraction and movement of the cell body

Figure 4.32: A schematic of the four basic steps involved in cell motion. Movement is initiated by the protrusion of the the cystoskeleton by actin polymerization 4.32(a) followed by formation of focal adhesion complexes and adhesion to the substrate 4.32(b). Next, the cell detaches its trailing edge from the substrate 4.32(c) and finally generates an internal force to contract and propel itself forward 4.32(d).

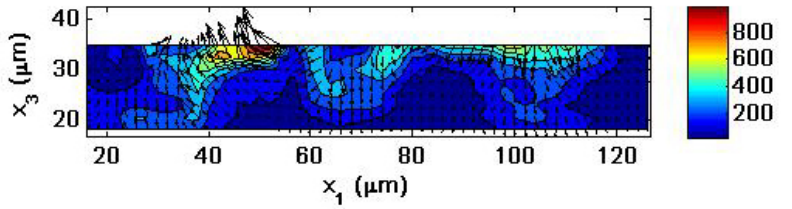

(a) Cell-induced shear tractions at $t_2 = 70$ min

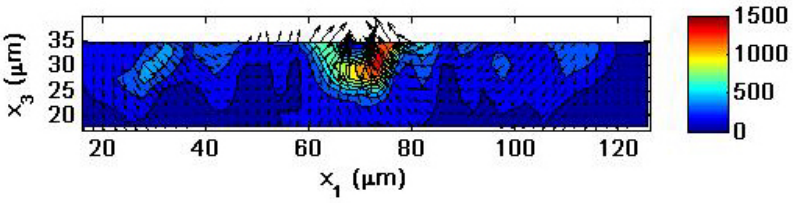

(b) Cell-induced shear tractions at $t_3 = 105$ min

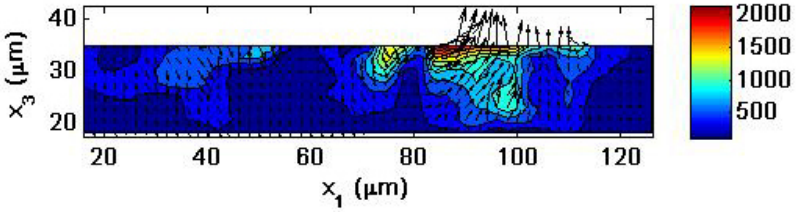

(c) Cell-induced shear tractions at $t_4 = 140$ min

Figure 4.33: Time evolution of cell-induced tractions as a function of depth (x_3) over 70 min along an arbitrary slice below the cell's long axis. The contour plots show the magnitude of the three-dimensional traction vector as previously plotted in Figs. 4.24(a) - 4.25(a). The black arrows represent the in-plane shear tractions (T_1, T_3), where the magnitude of the longest arrow in each Fig. is equal to the maximum value depicted by the color bar in $pN/\mu m^2$. The particular time increments that are shown here are t_2, t_3, and t_4, where the time increment between each frame is 35 min. The leading edge of the cell is located on the right ($\sim x_1 = 120$ μm), and the direction of cell migration is from left to right.

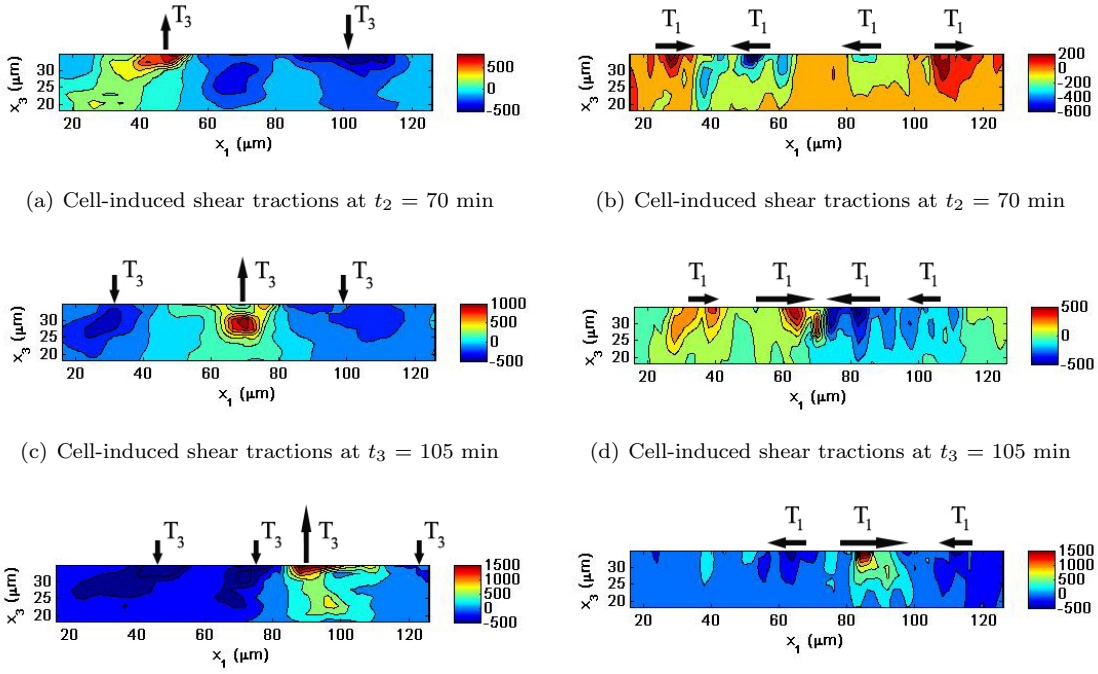

(a) Cell-induced shear tractions at $t_2 = 70$ min

(b) Cell-induced shear tractions at $t_2 = 70$ min

(c) Cell-induced shear tractions at $t_3 = 105$ min

(d) Cell-induced shear tractions at $t_3 = 105$ min

(e) Cell-induced shear tractions at $t_4 = 140$ min

(f) Cell-induced shear tractions at $t_4 = 140$ min

Figure 4.34: Time evolution of cell-induced shear tractions (T_1, T_3) as a function of depth (x_3) over 70 min along an arbitrary slice below the cell's long axis. The contour plots show the magnitude of the shear traction components (left column: T_3; right column: T_1). The color bar units are $pN/\mu m^2$. The black arrows on the top of each plot give the general direction of the cell-generated tractions. The particular time increments that are shown here are t_2, t_3, and t_4, where the time increment between each frame is 35 min. The leading edge of the cell is located on the right ($\sim x_1 = 120$ μm), and the direction of cell migration is from left to right.

Chapter 5

Conclusions

5.1 Summary

A novel experimental technique for measuring three-dimensional deformation fields in soft materials has been developed and its applicability to quantitatively investigate cell-matrix interactions has been demonstrated. This method utilizes the three-dimensional scanning ability of laser scanning confocal microscopy (LSCM) in conjunction with a digital volume correlation (DVC) algorithm as described in detail in Chapter 2. The utilization of a deconvolution algorithm to account for the effects of the point spread function along the optical imaging axis, is shown to improve the resolution of the LSCM images, leading to enhanced accuracy in the calculation of the displacement fields. The ability of this technique to determine full-field three-dimensional displacement information under large deformations was demonstrated in Chapter 2. One advantage of being able to measure large deformations accurately is being able to compile the cumulative evolution of the applied deformations. While incremental deformations can be added up to yield a cumulative representation of the deformation state, any perturbations or noise will not only affect the single measurement time point but rather the entire time evolution. Hence, a cumulative deformation evolution represents a more robust and potentially more accurate measurement.

The application of the LSCM-DVC technique to study the interaction of motile fibroblast cells with polyacrylamide substrates was discussed in Chapter 4. The results demonstrate the capability of this method to accurately map the cell-induced deformation fields during cell migration, and the

viability of determining the traction forces in three dimensions. While previous traction force methods provided significant insight into cell-matrix interactions in two dimensions, the newly developed technique demonstrates that these interactions can now be quantified in all three dimensions with high spatial resolution. Furthermore, all of the presented investigations in Chapter 4 were obtained dynamically with respect to the average speed of cell migration, allowing for an *in-situ* analysis of cell motility and the resulting mechanical interactions with the substrate. While previous studies focused primarily on quantifying traction forces and adhesion of spread cells [14, 41, 49], this study highlights the more dynamic substrate interactions of motile cells. While the main results of this study present quantitative experimental findings of cells interacting with soft biomaterials, in particular polyacrylamide gels of different moduli, Section 5.3 will provide an outlook on some of the experimental implications and future applications of these measurements and the LSCM-DVC technique.

5.2 Preliminary Cell Migration Studies on Artifical Extracellular Matrix Proteins (aECM)

This section provides some preliminary results on 3T3 fibroblast cells migrating on artificial extracellular matrix proteins (aECM) developed by Tirrell and coworkers [28, 21]. This new class of biomaterials offers greater control and versatility than traditional biomaterials since their molecular structure can be precisely controlled through genetic engineering. These proteins are designed to be employed as implant materials mimicking the key features of the natural extracellular matrix [28, 21]. Since, a cell's response is most often comprised of a variety of biochemical and biomechanical stimuli at a particular point in time, decoupling these signals requires information on the spatial and temporal location of these cell-matrix exchanges. In other words, by controlling the exact composition of the extracellular matrix, cell-specific signals and cues can be analyzed and potentially controlled. In brief, these novel biomaterials incorporate certain amino repeat sequences to control both a specific cell binding domain, e.g., RGD, CS5, etc., as well as their mechanical

properties. These materials can be crosslinked into thin films or three-dimensional matrices through the incorporation of the photosensitive non-canonical amino acid *p*-azidophenylalanine (pN$_3$Phe). Exposure of pN$_3$Phe to ultraviolet (UV) light results in the photodecomposition of the aryl azide, which mediates non-specific crosslinking, either by electrophilic trapping via ring expansion or by the diradical behavior of the triplet nitrene. Thus, this technique is well suited for fabrication of particular thin film geometric patterns [8]. Furthermore, the mechanical properties, such as the Young's modulus, can be tuned by altering the incorporation level of pN$_3$Phe with a typical modulus range of 0.3 - 1.0 MPa [33].

The experimental setup utilized is similar to the one described in Chapter 3 and hence, only the differences are discussed here. aECM proteins incorporating photosensitive pN$_3$Phe residues with elastin-based repeats for mechanical integrity and RGD cell binding domains are expressed and purified, dissolved, and deposited onto glass coverslips yielding typical thicknesses of 50 - 80 μm. As the protein is dissolved in dimethylsiloxane (DMSO), 0.5 μm fluorescent red microspheres are mixed with the protein solution similar in fashion to the preparation protocol described in Chapter 3. The final step consists of crosslinking the protein, which is achieved through UV irradiation for several minutes. Next, GFP-actin expressing cells are seeded on the top surface of the aECM matrices and imaged in 45 min time increments over time periods up to 24 hours. The imaging setup and the imaging conditions are the same as described in Chapter 3.

Figure 5.1 shows that the cells appear well adhered to the aECM substrate and remain motile and alive after several hours of imaging. Comparing the general cell shape in Fig. 5.1, the fibroblast seeded on top of the aECM protein substrates are spread over a larger area and are thinner in cross-section when compared to the fibroblast seeded on top of the presented polyacrylamide gels in Chapter 4. A very similar cell morphology is observed when fibroblasts are placed on glass substrates indicating a potential connection between cell shape and substrate Young's modulus.

Figure 5.2 shows preliminary cell displacement measurements during fibroblast migration on the aECM substrate shown in Fig. 5.1. It is important to note that the generally observed displacements in Figs. 5.2(a) - 5.2(d) are indiscernible from measurement noise, whose threshold was previously

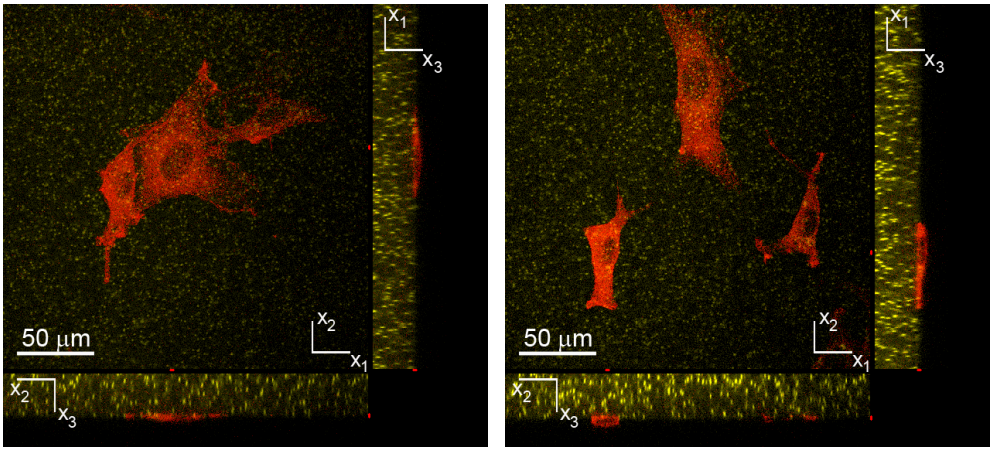

(a) LSCM composite image at t_0 (beginning of imaging)

(b) LSCM composite image at $t_{10} = 450$ min

Figure 5.1: LSCM image depicting three arbitrary planar slices of the entire volumetric image stack at two different imaging times. Fibroblast cells displaying GFP-actin are shown in red, whereas the 0.5 µm fluorescent microspheres are shown in yellow.

established ~ 0.12 µm. One possible explanation is that cells have a finite amount of internal force they can generate and transmit to the substrate. Hence, the resulting surface deformations due to the higher substrate stiffness cannot be detected by the optical methods employed here. It is also worth noting that most traction force studies typically report Young's moduli in the range of $\sim$ 0.1 - 25 kPa [14, 49, 41]. New proteins are currently being designed to increase the compliance of the aECM substrates by increasing the molecular weight between individual crosslinks, such that the LSCM-DVC can be successfully employed to study cell-induced surface deformations and their connection to specific biochemical stimuli. These studies have great potential in providing deeper insight into the biomechanochemical coupling during cell-matrix interactions.

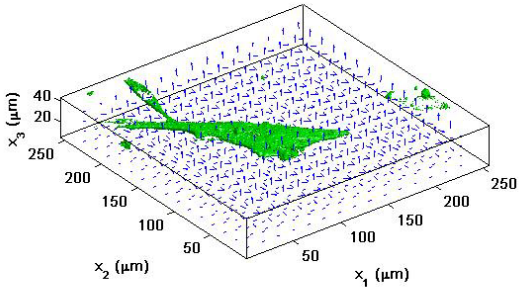

(a) Measured cell displacement fields at $t_1 = 45$ min

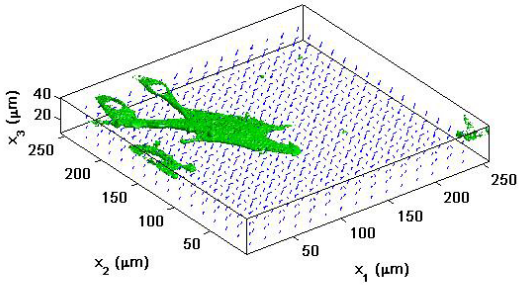

(b) Measured cell displacement fields at $t_3 = 135$ min

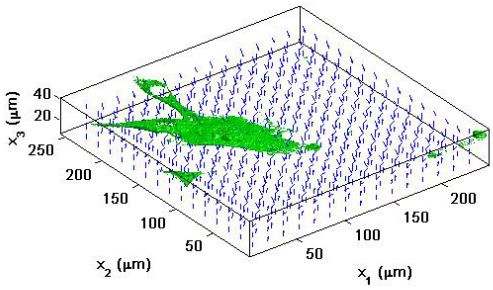

(c) Measured cell displacement fields at $t_5 = 225$ min

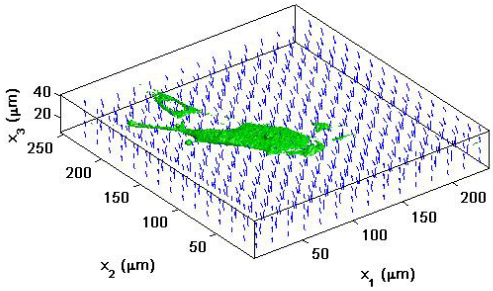

(d) Measured cell displacement fields at $t_7 = 315$ min

Figure 5.2: Time series of the LSCM-DVC measured three-dimensional displacement vector fields. The average vector length in each plot is between 0.06 - 0.18 µm. The fibroblasts cells are superimposed in green (GFP-actin).

5.3 Recommendation for Future Work

As demonstrated, the LSCM-DVC technique is capable of determining full-field three-dimensional displacement and strain information inside transparent materials with subpixel or submicron resolution. Also, the addition of a stretch-correction algorithm was shown to improve the overall precision of the methodology, especially under large deformation applications (strain $> 5\%$). However, in the large deformation formulation presented, only the three principal stretches were considered excluding both large shear deformations and rotations. In the future, the inclusion of the full stretch and rotation tensors should provide an even more accurate and precise full-field displacement measurement. While one study has addressed the issue of finite rotations [4], there has been no study to date that accounted for all 12 degrees of freedom. While this implementation, namely of the entire deformation gradient, is straightforward in the two-dimensional case of digital image correlation (DIC), it is non-trivial in three dimensions due to the high computational cost. The development of time-effective algorithms to incorporate both finite rotations and stretches in three-dimensional should alleviate this issue in the future. In particular, one of the potential next steps in the continued evolution of the DVC algorithm presented here is the incorporation of the already existing finite rotation algorithm into the stretch-correlation correction. Since DVC is not dependent on any particular image capturing method, its application might find further application in other imaging techniques, such as magnetic resonance imaging (MRI) and computer tomography (CT) scanning, where the only necessity is the generation of volumetric images entailing some sort of speckle or trackable pattern.

The combination of LSCM and DVC can lead to numerous quantitative applications in particular, but not exclusive, to cell mechanics. In particular, the method can be used to quantitatively study local force transmission by monitoring certain focal adhesion proteins and their force transmission locally using a smaller field of view. This can be achieved by using submicron tracker particles in conjunction with fluorescently labeled focal adhesion proteins, such as vinculin, talin, etc. Furthermore, interactions between multiple cells, including cell clusters and sheets, can be investigated quantitatively using the LSCM-DVC technique. In addition the development of novel biomaterials

relies on the capability of actively controlling or stimulating a particular cell response with the goal of reproducing the natural cell-cell or cell-matrix behavior. This technique has the ability to assist in the quantitative correlation between biomechanical and biochemical events. Furthermore, fundamental questions between biochemical signaling and mechanical stimulation for fully encapsulated cells, such as environmentally induced cell transformations from benign to malignant cancer cells can be addressed in a quantitative manner.

While these applications highlight the versatility of the technique to cell mechanics research, there are also many opportunities to study mechanics-based problems using the combination of LSCM and DVC. Some of these problems include contact studies, such as indentation and adhesion problems, where the contact area might be changing or non-linearities in the employed geometries make the observations difficult. For instance, some of the difficulties in calculating the mechanical properties from indentation data stems from the fact, that the contact area of the indenter and the surface interactions between the indenter and the sample surface are either unknown or poorly understood. The LSCM-DVC method could provide the deformation information needed to better understand these interactions for transparent materials. In conclusion, the quantitative three-dimensional full-field imaging technique presented here offers a new way to investigate cell-mediated mechanical interactions and three-dimensional mechanics problems with high spatial resolution.

Appendix A

Mechanically Tunable Thin Films of Photosensitive Artificial Proteins: Preparation and Characterization by Nanoindentation

It should be noted that what follows has been previously published by the authors in *Macromolecules* **2008**, *41*, 1839-1845.

Mechanically Tunable Thin Films of Photosensitive Artificial Proteins: Preparation and Characterization by Nanoindentation

Paul J. Nowatzki[1], Christian Franck[3], Stacey Maskarinec[1], Guruswami Ravichandran[3], and David A. Tirrell[1,2*] (1) Division of Chemistry and Chemical Engineering

(2) Joseph J. Jacobs Institute for Molecular Engineering for Medicine

(3) Division of Engineering and Applied Science

California Institute of Technology, Pasadena, California 91125, USA

Corresponding Author: tirrell@caltech.edu

Abstract

Thin films of controlled elastic modulus were made by photocrosslinking artificial extracellular matrix (aECM) proteins containing the photosensitive amino acid para-azidophenylalanine (pN$_3$Phe). The elastic moduli of the films were calculated from nanoindentation data collected by atomic force microscopy (AFM) using a thin-film Hertz model. The modulus was shown to be tunable in the range 0.3-1.0 MPa either by controlling the irradiation time or by varying the level of pN$_3$Phe in the protein. Tensile measurements on bulk films of the same proteins and finite-element simulation of the indentation process agreed with the thin-film modulus measurements from AFM. Substrates characterized by spatial variation in elastic modulus were created by local control of the irradiation time.

Introduction

Cellular interactions with the surrounding matrix play defining roles in biological processes ranging from normal tissue function to morphogenesis, immunity, wound healing, and tumor metastasis. The realization that substrate mechanical properties strongly influence cell behavior is comparatively recent and has stimulated considerable interest.[1] Substrate stiffness has been shown to affect cell adhesion,[2,3] morphology,[2,4,5] traction forces and migration rate,[2,6,7] growth,[8] and differentiation.[3,9−11].

Cell culture substrates with adjustable mechanical properties have become essential tools for the study of cell-matrix interactions. The stiffness-dependent cell behavior reported to date has been examined most frequently on synthetic gels such as polyacrylamide.[2,6,12] Because biological and mechanical signals are often interdependent,[1,13] some investigators have chosen substrates (e.g., collagen-coated gels) that mimic more closely the natural extracellular matrix.[3,8] Additional advantages accrue from varying mechanical properties on a single substrate, in that many sets of culture conditions can be probed at once, reducing the experimental variability that arises from lot-to-lot variation in the behavior of cultured cells. Moreover, films of spatially varying elastic modulus allow

the examination of cell behavior at mechanical interfaces,6 and elastic modulus gradients allow the study of mechanotaxis or durotaxis.[7,14,15]

Here we describe the use of photosensitive artificial proteins to make substrates on which the interrelated effects of elastic modulus and extracellular matrix biology can be studied directly. These proteins are intended for use as implantable biomaterials, and are designed to mimic key features of the extracellular matrix.[16−19] The design (Figure A.1) includes cell-binding domains periodically spaced between elastin-like repeating elements. The CS5 cell-binding domain, derived from human fibronectin, enables attachment of cells that express the $\alpha_4\beta_1$ integrin adhesion receptor.[20] The origin of the elasticity of the protein is the repeating pentapeptide VPGVG (Val-Pro-Gly-Val-Gly), derived from mammalian elastin and shown by Urry and others to confer mechanical properties appropriate for soft tissue engineering and regenerative medicine.[21]

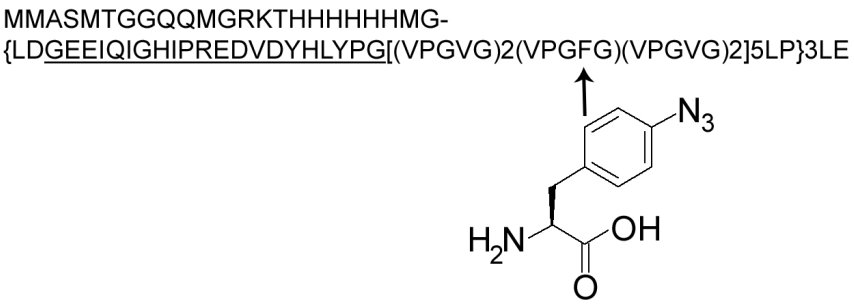

Figure A.1: Amino acid sequence of the artificial extracellular matrix protein examined in this work. The cell-binding sequence CS5 is underlined. Proteins containing the photosensitive amino acid para-azidophenylalanine are designated aE-pN$_3$Phe.

The phenylalanine (Phe) sites encoded within the elastin-like domains of the protein serve as sites for incorporation of the non-canonical amino acid para-azidophenylalanine (pN$_3$Phe, Figure A.1). Incorporation of pN$_3$Phe into recombinant proteins is accomplished by using a bacterial expression host that harbors a mutant phenylalanyl-tRNA synthetase (PheRS) with an enlarged binding pocket.[22,23] Upon photolysis, pN$_3$Phe generates a reactive nitrene intermediate that yields non-specific crosslinks to surrounding protein molecules. Varying the concentration of pN$_3$Phe in the expression medium controls the extent of incorporation of the photosensitive amino acid into the protein, and ultimately determines the crosslink density and elastic modulus of the irradiated

protein film. We recently reported photochemical patterning of similar proteins (and adherent cells) on solid substrates.[24] Here we describe detailed mechanical characterization of thin photocrosslinked protein films and demonstrate the preparation of step-gradients of mechanical properties within a single film.

Mechanical properties of thin, substrate-bound films are typically measured by nanoindentation, and atomic force microscopy (AFM)-based nanoindentation in particular offers significant advantages in spatial and force resolution over conventional nanoindenters. The method is especially attractive for analyzing soft samples and materials whose elastic modulus varies over short length scales.[25−27]

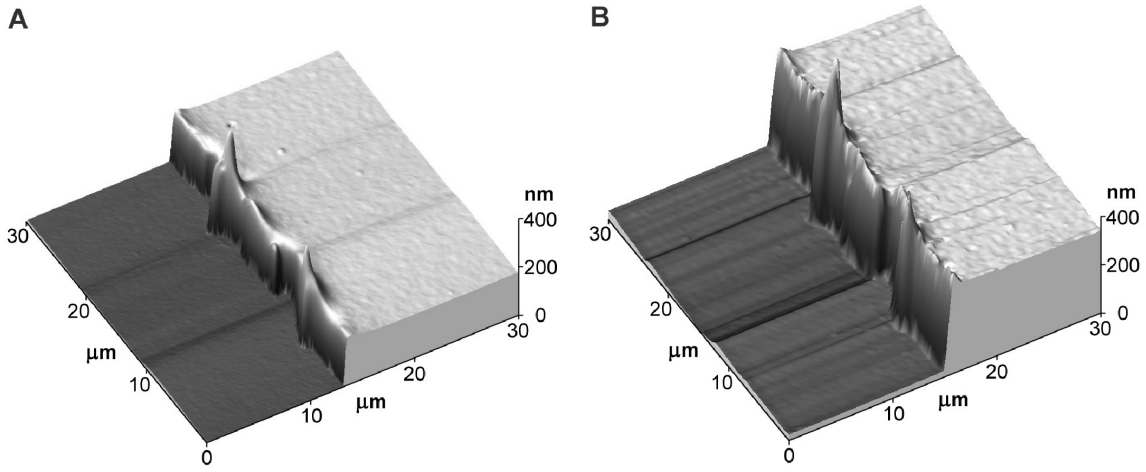

Figure A.2: AFM topography scans of cut edges of an aE-48%-pN$_3$Phe film, dry (A) and in water (B). The spikes at the edge are artifacts of the scratching procedure.

Here AFM nanoindentation with a microspherical tip (600 nm diameter) was used to obtain accurate measurements of the elastic moduli of thin photocrosslinked protein films.[11,28,29] The use of a spherical tip is important, in that it allows a spherical indentation model to be correctly applied; the classical Hertz spherical model is known to cause distortions when used to analyze AFM data collected with conventional sharp, pyramidal or conical tips.[30] A film-height dependent physical model [31] accounts for the mechanical coupling of the film to its underlying substrate, another known source of distortion in AFM nanoindentation.[32,33] Bulk tensile tests of the same materials confirm the validity of the nanoindentation analysis.Finite element simulations of the indentations were also performed to verify the modulus calculations and to explore the possibility of determining a more

sophisticated mechanical material model from the AFM data. While the linear elasticity model [31] accurately characterizes the Young's (elastic) moduli of the films described herein, the finite element analysis is appropriate for characterization of thinner films undergoing large deformations due to higher-strain indentation or certain tip geometries.

Experimental Section

Protein aE-pN$_3$Phe. The amino acid sequence of the photosensitive artificial extracellular protein, aE-pN$_3$Phe, is shown in Figure A.1. aE-pN$_3$Phe is made biosynthetically in a Phe-auxotrophic strain of Escherichia coli outfitted with a plasmid bearing genes coding for both the protein and the Ala294Gly mutant of the *E.* coli phenylalanyl-tRNA synthetase (PheRS).[34] Use of the mutant synthetase allows incorporation of pN$_3$Phe (Bachem) into recombinant proteins in place of Phe.[23] Because the relative amounts of Phe and pN$_3$Phe in the protein can be controlled by varying the concentrations of the amino acids in the expression medium, the designation aE-pN$_3$Phe refers to a family of artificial proteins rather than to a single protein.

The expression and purification of aE-pN$_3$Phe were performed as described previously.[24] To deplete Phe from the expression medium, cells were centrifuged and resuspended in minimal medium lacking Phe and containing pN$_3$Phe 10 minutes after expression was induced. This procedure allows enough time for functional copies of PheRS to be synthesized before Phe is depleted.

The extent of replacement of Phe by pN$_3$Phe was measured by 600 MHz 1H NMR spectroscopy (Varian) at a protein concentration of 15 mg/mL in DMSO-d6 (Cambridge Isotope Laboratories).[24] Phe replacement levels of 28%, 31%, 48%, and 66% were achieved by using 125, 188, 250, and 250 mg/L, respectively, of pN$_3$Phe in the culture medium; the corresponding proteins are designated aE-28%-pN$_3$Phe, etc.

AFM - instrument. Images and force curves were collected on a Park Scientific Instruments AutoProbe M5 atomic force microscope, with accompanying ProScan v1.51b software. Pyramidal-tipped triangular silicon nitride cantilevers with nominal spring constant 0.58 N/m were used for imaging (Veeco DNP-S). A silicon nitride cantilever of the same shape, with an attached 600 nm

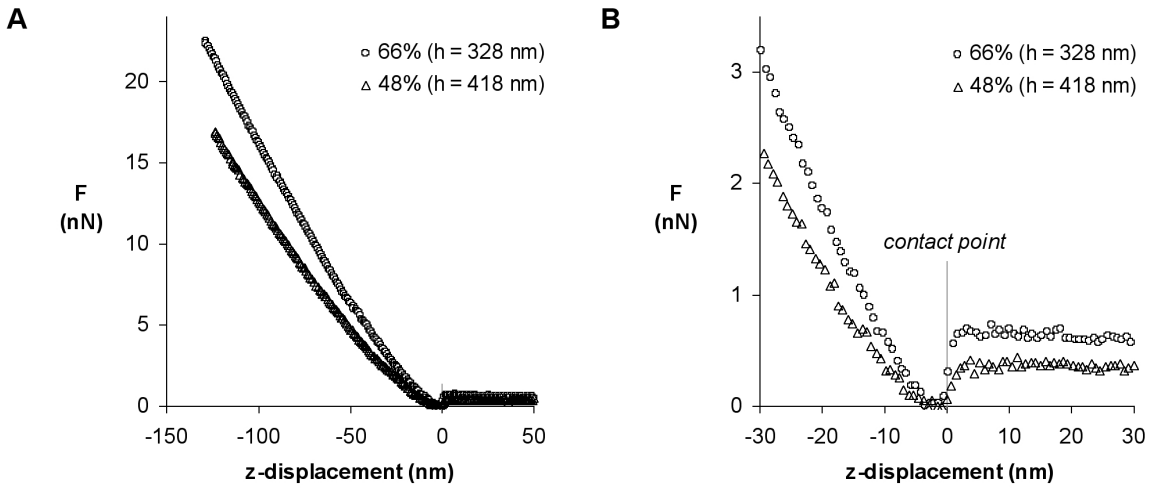

Figure A.3: Representative loading indentation profiles for thin films of aE-66%-pN$_3$Phe and aE-48%-pN$_3$Phe, showing force versus indentation depth (z-displacement). (A) shows the entire profiles; (B) is magnified to show the contact point assignment.

diameter SiO_2 particle tip (Novascan, Ames, IA), was used to indent samples for collecting force curves. The spring constant of the cantilever was calculated to be 0.37 N/m by indenting against reference cantilevers with predetermined spring constants of 1.00 N/m and 0.125 N/m (Veeco CLFC). Here, $k_{test}/k_{ref} = (\delta_{tot} - \delta_{test})/(\delta_{test} cos(\theta))$, where k_{test} and k_{ref} are the spring constants of the test and reference cantilevers, δ_{tot} and δ_{test} are slopes of the force-distance curves when the test cantilever is indented against a rigid surface and against the free end of a reference cantilever, respectively, and θ is the angle between the cantilevers (15^o). A glass slide was glued to the back of the cantilever mount so that the cantilever and sample could be submerged in water.

Bulk protein films. aE-pN$_3$Phe (4 mg) was dissolved in dimethylsulfoxide (40 µL, Mallinckrodt). The solution was spread to cover an area ca. 1.5 cm x 1 cm on a poly(methyl methacrylate) surface, and the solvent was evaporated at 50^oC overnight. The resulting films were ca. 20 µm thick (dry). After photocrosslinking (vide infra), uniaxial tension tests were performed at 22^oC on an Instron 5542 Materials Testing System outfitted with a 0.5 N load cell and modified to contain the sample in a water bath. The nominal strain rate was 0.1 per minute;[35] at this rate viscoelastic effects are negligible.

Thin protein films. All film-making procedures were performed in a cold room (4^oC), below the

lower critical solution temperature (LCST)21 of the protein in water. Protein (10 mg) was dissolved in water (100 μL), and the solution was centrifuged (5 min, 16,500g) to remove any aggregates or particles. Protein solution (10 μL) was pipetted onto and spread to cover an unmodified 12 mm glass slide (Hecht-Assistent, Sondheim, Germany). Films were spin-coated (Specialty Coating Systems, Inc. P6204, Indianapolis, IN) at 7,000 rpm for 30 seconds and dried overnight at 4°C. Typical film thickness was ca. 160 nm (dry).

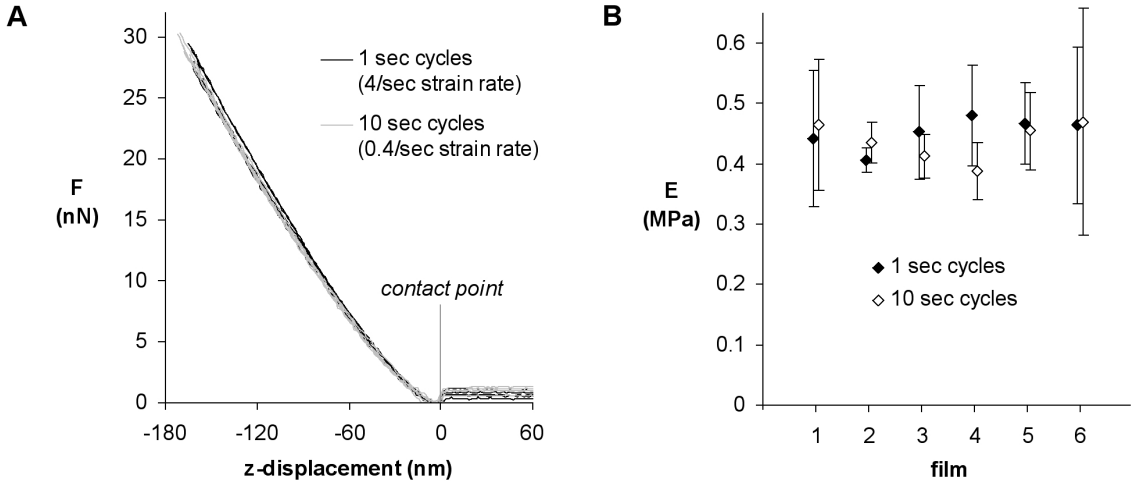

Figure A.4: (A) Superimposed force profiles for multiple indentations of a single aE-48%-*p*N_3Phe film for 1 sec and 10 sec indent cycles. (B) Calculated Young's modulus for 1 sec and 10 sec indentation cycles on five different aE-48%-*p*N_3Phe films.

Irradiation of films. Dry protein films were exposed to unfiltered UV light from a high-pressure mercury arc lamp (Oriel Q, 100 watt @ 5 amps, > 20 min warm-up time; measured intensity in irradiation plane = 1.5 mW/mm2). The time required to achieve complete conversion, ca. 300 sec, was determined empirically. Zones of differential crosslinking were prepared on the same substrate by placing an opaque shutter over portions of the film during irradiation. Specifically, a step-gradient of irradiation times (0, 12, 20, 30, 50, 80, 120, 180, and 300 sec) was made across a 12 mm slide by manually repositioning the shutter between exposures.

Slides were agitated in excess water at 4°C to remove any soluble protein. Un-irradiated protein, or protein irradiated for 12 sec or less, was completely removed during this rinsing process as evidenced by AFM imaging. No delamination of irradiated films from their glass substrates was

protein	pN$_3$Phe added to medium (mg/L)	% replacement of Phe by pN$_3$Phe	protein yield (mg protein/liter of culture)
aE-66%-pN$_3$Phe	250	66	66
aE-48%-pN$_3$Phe	250	48	35
aE-31%-pN$_3$Phe	188	31	76
aE-28%-pN$_3$Phe	125	28	66

Table A.1: Expression conditions and protein yields

observed.

AFM film thickness. The tip of a pair of fine forceps was dragged lightly across the surface of the protein film, tearing away the protein along the scratch and revealing the underlying glass substrate. The edge of this scratch was imaged by AFM both dry and under water; the thickness of the film is apparent from the scan (see Figure A.2). The surface revealed by the scratch was confirmed to be glass, based on its smoothness and linear force profile when indented. The protein film thickness was calculated by averaging the height measurements at many (n $\geq$ 16) points on the film, using the revealed glass surface as a baseline.

AFM indentation force curves. The films and cantilever assembly were submerged in water under ambient conditions. The 600-nm SiO_2 microsphere tip was placed above a spot where the film thickness had been measured (identified visually from the optical microscope image using reference markers on the film) to ensure that the thickness at the point of indentation was known. Force curves were collected; the instrument records z (piezo) displacement, and force, which is the product of measured tip deflection and cantilever spring constant.

The indentation range was set to (-150 nm, +1350 nm) relative to the contact point, effectively limiting the force to ca. 20-30 nN and the strain magnitude to less than 20%. The indent-retract cycle time was 1 sec (tip speed 3 μm/sec). Viscoelastic effects did not appear to be a significant factor at this strain rate (ca. 4 sec 1), as evidenced by the statistical superimposability of force curves collected using 1 sec and 10 sec cycles (strain rate ca. 0.4 sec 1) (Figure A.4).

To assess the uniformity of the films, force curves were evaluated repeatedly at the same spot and at nearby spots spaced 10-20 μm apart. For uniformly irradiated pN$_3$Phe films this procedure

was repeated at three distant (> 1 mm apart) spots of known height.

Calculation of Young's (elastic) modulus. The Dimitriadis model [31] for indentation of linearly-elastic soft material films of finite height with a spherical indenter was applied to the loading force data. For a support-bonded film with Poisson's ratio of $\nu = 0.5$ (incompressible, a reasonable estimate for both for rubbery networks and biological materials):

$$F = \frac{16E}{9} R^{1/2} \delta^{3/2} [1 + 1.133\chi + 1.283\chi^2 + 0.769\chi^3 + 0.0975\chi^4]. \tag{A.1}$$

The first term of this series is the classical Hertz indentation model, giving the force F as a function of (Young's) elastic modulus E and indentation depth δ using a rigid sphere of radius R. The additional terms [31] correct for the finite height of the film, where χ is given by:

$$\chi = \sqrt{R\delta}/h, \tag{A.2}$$

where h is the thickness of the film. As the film gets thinner, or as the indentation depth increases, the indenting sphere (AFM tip) experiences a higher force than it would for an infinitely-thick film of the same material, owing to mechanical effects of film confinement to the stiff underlying substrate. The film indentation δ was calculated by subtracting the tip displacement from the total (z) displacement.

The contact point of each force-distance curve, where the indentation and force were set to zero in the analysis, was determined by visual inspection. While this can be difficult in some experiments, [31] it is straightforward for the force curves collected here, because we observe a distinct snap-in when the tip touches the surface (see Figure A.3 for examples). The apparent elastic modulus was calculated by evaluating equations A.1 and A.2 at each recorded force-indentation point between 15 nm and 10% film thickness indentation and averaging over the range. Below 15 nm, the scatter in the data is magnified in the calculations and distortions are common; the 10% maximum indentation constrains the data to the near-linear response range.31 In this strain range, the finite-height correction factor was as large as 1.78 ($\chi = 0.395$) for the films analyzed here.

Finite element simulation. Simulations of the nanoindentation process were conducted by using the commercial finite element software, ABAQUS (ABAQUS, Inc., Providence, RI). The geometries of the indenter and the film were discretized by using 2D axisymmetric elements ($CAX4R$) and the known protein film height and indenting spherical tip geometry ($R = 300$ nm). From tensile data collected for bulk samples of aE-pN$_3$Phe, material model parameters for each material were calculated and entered into the simulation. Various hyperelastic material models describing the large strain material behavior (e.g., Neo-Hookean, Mooney-Rivlin, etc.) were evaluated. The Yeoh model [36] was found to best describe the material response of aE-pN$_3$Phe as determined through numerous uniaxial tension and compression tests. The output of force versus film indentation was compared to the AFM data collected experimentally.

Results And Discussion

Protein production and purification. aE-pN$_3$Phe proteins were expressed in a phenylalanine-auxotrophic $E.$ coli expression host using a medium shift procedure which allowed controlled replacement of phenylalanine by pN$_3$Phe. Cells were grown for several hours in media containing all 20 natural amino acids, washed and transferred to minimal media containing 19 amino acids and lacking phenylalanine. Production of the mutant PheRS during the initial growth period provides the cellular machinery needed for insertion of pN$_3$Phe into recombinant proteins. Target proteins were collected from harvested cells and separated from contaminant proteins through a series of temperature-shift centrifugation cycles24, and protein purity was monitored by denaturing gel electrophoresis. Titrating the amount of pN$_3$Phe in the expression medium generated artificial proteins containing controlled levels of incorporation of the photosensitive amino acid (Table A.1).

Thin films. Spin-coated thin films of aE-pN$_3$Phe proteins appeared smooth (RMS roughness = 1.3 nm, versus 0.9 nm for the revealed glass) when imaged by AFM (Figure A.2). Film thickness was uniform over the surface of each 12 mm diameter glass substrate, varying no more than 11% from the average. Local thickness was much more uniform, with $< 2\%$ variation in a 30 μm scan. The protein films had average hydrated thicknesses between 206 and 368 nm, except for two films

protein	thickness (μm)	average elastic modulus, E (MPa)	molecular weight between crosslinks, Mc	pN$_3$Phe crosslinking reaction efficiency (%)
aE-66%-pN$_3$Phe	20	1.01 ± 0.07	4300 ± 200	50 ± 3
aE-48%-pN$_3$Phe	21	0.52 ± 0.04	7000 ± 400	42 ± 2
aE-31%-pN$_3$Phe	19	0.20 ± 0.04	11,900 ± 1000	39 ± 3
aE-28%-pN$_3$Phe	20	0.14 ± 0.02	13,800 ± 600	37 ± 2

Table A.2: Physical properties of bulk aE-pN$_3$Phe films tested in uniaxial tension (n=2).

protein	average hydrated thickness of each tested film (nm)	average elastic modulus, E (MPa)	molecular weight between crosslinks, Mc	pN$_3$Phe crosslinking reaction efficiency (%)
aE-66%-pN$_3$Phe	312, 322, 328, 1682, 1466	0.91 ± 0.16	4900 ± 700	45 ± 7
aE-48%-pN$_3$Phe	293, 368	0.44 ± 0.04	7800 ± 400	38 ± 2
aE-31%-pN$_3$Phe	223, 252	0.30 ± 0.02	9800 ± 400	47 ± 2
aE-28%-pN$_3$Phe	206, 206	0.29 ± 0.03	10,000 ± 500	51 ± 3

Table A.3: Physical properties of thin aE-pN$_3$Phe films tested by AFM (n6 spots, n24 total indents).

ca. 1500 nm thick, which were made by using a higher concentration of aE-66%-pN$_3$Phe (Table A.3). The average ratio of wet-to-dry film thickness was 1.80, corresponding to a polymer volume fraction of 0.56 in the hydrated films. We observed little variation in the polymer volume fraction under the conditions used here.

AFM Force Curves. Representative loading force-displacement curves are shown in Figure A.3, and exhibit the parabolic shape typical of indentation of soft materials. Since the assembly is submerged in water, the attractive force between the tip and the surface is screened; nevertheless, a distinct snap-in event appears in each force curve, and allows a contact point to be confidently assigned.

In cases where snap-in appeared to occur over a few nanometers, the contact point was assigned to the middle of the snap-in rather than the bottom (at minimum force); this procedure was found to give the best reproducibility between repeated indentations at the same spot. Adhesion forces between the indenter and sample appeared to be negligible during indentation loading, and finite element simulations confirmed this interpretation.

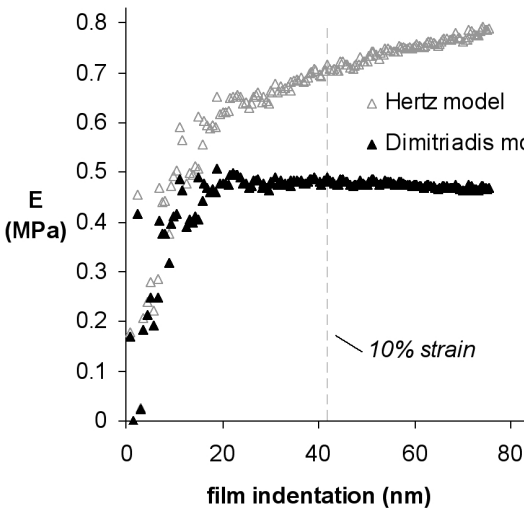

Figure A.5: The elastic modulus (E) calculated at each point in the AFM indentation using Hertz and Dimitriadis models (Eq. A.1) is shown for an aE-48%-pN$_3$Phe film.

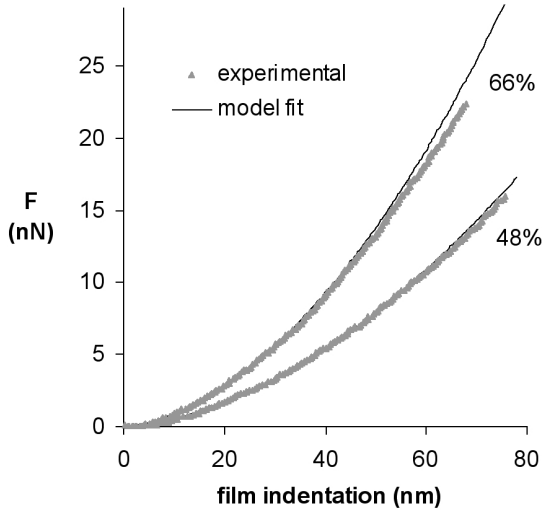

Figure A.6: Experimental AFM indentation data compared to Dimitriadis model (Eq. A.1) fits for thin films of aE-66%-pN$_3$Phe and aE-48%-pN$_3$Phe.

When the strain rate was reduced by a factor of 10 (from a 1 sec indentation cycle, strain rate ca. 4 sec-1), the resulting force curves appeared indistinguishable from the originals, indicating that viscoelastic effects did not significantly influence the results (Figure A.4) in the range of loading rates considered here (0.4 to 4 sec-1). Faster indentation cycles allow increased throughput and minimize the deleterious effects of sensor drift.

Repeated indentations (up to 100) of the same spot did not cause any change in the force-displacement curves, likely because the hydrated protein films are highly elastic (albeit nonlinear) and the indentation depth was controlled. When surfaces on which the indentations had been performed were subsequently imaged by AFM, no evidence of indentation was seen on either hydrated or dry films. These results suggest that the collection of force curves did not permanently deform or otherwise alter the mechanical properties of the samples.

Analysis of AFM force curves. Once a force curve is collected, all variables except E in Eqs. A.1 and A.2 are known, so each point on the force-distance curve can be used to calculate an elastic modulus for the material. If the model describes the system correctly, the calculated modulus should be the same at each indentation depth. The Hertz and Dimitriadis [31] models were evaluated using

this criterion for a representative data set (Figure A.5). Because the films were less than a micron in thickness and the indentation depth represented a significant portion of the film height, the Hertz model for infinite-height film was inappropriate for elastic modulus calculation. The effective elastic properties of the protein films were significantly influenced by the underlying glass substrate, as has been observed previously for soft thin films.[31,32]

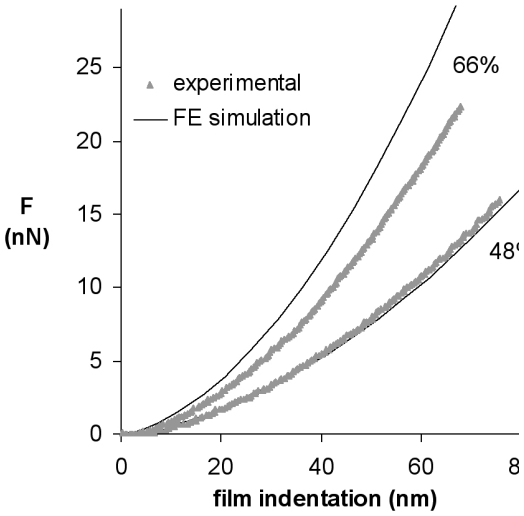

Figure A.7: Superposition of experimental AFM data and finite element simulations of indentation based on bulk tensile data for thin films of aE-66%-pN$_3$Phe and aE-48%-pN$_3$Phe.

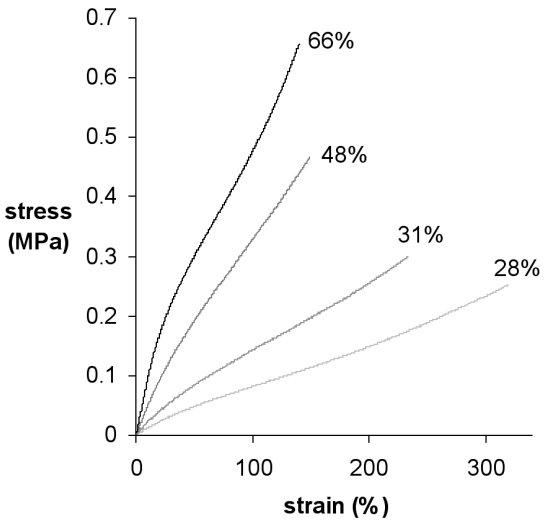

Figure A.8: Sample tensile data for bulk films containing varying amounts of pN$_3$Phe.

Because it accounts for finite sample thickness and coupling to a rigid substrate, the Dimitriadis model is able to extract the true elastic modulus of the protein film, thus yielding much more consistent predictions of thin film modulus for each force curve in the indentation depth range of 15 nm to 10% (or more) of the film thickness.

A single value of Young's modulus (E) was assigned to each surface by averaging the model-predicted moduli from 15 nm to 10% strain; the standard deviation in E over this range averaged 3.4% and was $< 10\%$ for all curves, indicating that the Dimitriadis model gives uniform predictions of E. In general, the model-calculated value of E is sensitive to the placement of the contact point,[31] but since contact is observed directly and the sub-15 nm data (recorded forces < 1 nN) are excluded, the fits are robust. Illustrations of the fit of the Dimitriadis model to the experimental AFM data

are shown in Figure A.6.

The standard deviation in E from repeated indentation of the same spot (n=3-4 indentations, 51 spots) averaged 5.1%. We observed no tendency of the film to change in modulus with repeated indentation. The standard deviation in E between different spots on the same film (n=3-4 spots,$\geq$10 μm apart, 13 films) averaged 7.2%, nearly as small as the same-spot variance, indicating that E was uniform over the films. The uniformity of modulus is important for the application of these films as probes of mechanosensitive cell behavior.

In principle, raw AFM data could be used to estimate film thickness, by iterating the height parameter in Eq. A.2 to minimize the variation in predicted modulus over the selected strain range, since over- or underestimated thickness will result in less consistent modulus predictions. For this technique to be applied, the linear model would need to completely describe the material mechanics in the analyzed strain range. However, experimental error makes it likely that decreases in film thickness could be mistaken for increases in elastic modulus, or vice-versa. The determination of modulus is more accurate when the film thickness is known, as it is here.

Finite element simulation of indentation. All bulk tensile data were well-described by a Yeoh hyperelastic model.[36] When the Yeoh parameters calculated from the tensile data (vide infra; see Figure A.8) were used to model indentation using a finite element simulation, the predicted force-displacement curves were very similar to those obtained experimentally; representative data are presented in Figure A.7. Because of the experimental error in measuring quantities such as the bulk film thickness or AFM cantilever spring constant, some differences in scalar magnitude between these two plots can be expected, although their shapes should be similar, as observed. The similarity between experimental AFM indentation data and simulations of the indentation using only bulk tensile properties is encouraging since it implies that the physical properties of thin and bulk films are similar, and it confirms the validity of the finite element analysis technique.

The samples investigated here are thick relative to the indentation depth and are highly elastic, so the deviations from linearity are small, as can be seen by comparing the linear model fit with experimental AFM data in Figure A.6. However, the simulation approach should be applicable

to thinner films (e.g., <100 nm) and to non-linear strain data as well, where a limited amount of data can be collected in the linear deformation range. While the Dimitriadis model is restricted to spherical tips, the simulation can be easily changed to describe conical or pyramidal tips, the type more commonly used because of their robustness and lower cost. These sharp tips have the additional advantage of being usable for imaging as well as indentation.

In performing the inverse analysis of predicting the AFM response from the tensile data, we used the AFM data to calculate a modulus for the material using the simulation. Coefficients of the Yeoh model were iterated in the finite element simulation to minimize the difference between the simulated and experimental AFM data using the entire force curve (including indentation data past 10% of the film thickness). The moduli determined in this way were indistinguishable from those calculated with the Dimitriadis model. If high-strain data are collected, this technique can provide the complete strain energy function for the material being tested in addition to the elastic Young's modulus (E). While the finite element technique provides more flexibility, the simplicity of the Dimitriadis model is preferable when the geometry of the tip is known and when the linear elastic modulus is the only value required.

Modulus control by variable incorporation of *p*N_3Phe bulk films. As described earlier, the extent of incorporation of $p$$N_3$Phe into a$E$-$p$$N_3$Phe proteins can be controlled by varying the concentration of the photosensitive amino acid in the expression medium. We examined the effects of variable incorporation of $p$$N_3$Phe, both for bulk samples tested in uniaxial tension and for thin-film samples analyzed by AFM nanoindentation.

The tensile behavior of the bulk samples (Figure A.8) is typical of rubbery materials; all aE-$p$$N_3$Phe films were extensible to 150% (or greater) strains. As expected, the modulus increases with the $p$$N_3$Phe content of the protein, a result of increased crosslink density after irradiation. If the materials are assumed to behave as ideal rubber networks, the shear modulus (G) can be related to the crosslink density through the expression[37]:

$$G = (\rho RT/M_c)(1 - 2M_c/M), \tag{A.3}$$

an approximation shown to be valid for similar elastin-like hydrogels.[17,35] The shear modulus is equal to one-third of the elastic modulus for an incompressible material (ν=0.5), a good approximation for rubbery hydrated protein films. The chain mass density ρ is found by multiplying the density of elastin[3]8 (1.32 g/cm^3) by the measured polymer volume fraction (0.56) in the films, M_c is the average molecular weight between crosslinks, and the term (1-2M_c/M) represents the fraction of elastically active crosslinks, where M is the molecular weight of the protein (42,900). The values of M_c calculated for the films examined here are listed in Table A.2.

The efficiency of crosslinking can be calculated from Mc and the pN$_3$Phe content of the protein. For example, the value of Mc (4300) estimated for aE-66%-pN$_3$Phe corresponds to ca. 10 (42,900/4300) crosslinks per protein chain, assuming random crosslinking a reasonable assumption given the periodic Phe spacing in the protein and the statistical nature of its replacement by pN$_3$Phe. Incorporation of the photosensitive amino acid at 66% of the 15 Phe sites yields an average of 9.9 pN$_3$Phe side chains per molecule; because each crosslinking event couples two molecules, the measured value of Mc indicates a reaction efficiency of ca. 50% (10/9.9/2). The crosslinking efficiency declines slightly as the pN$_3$Phe content of the film is reduced (Table A.2).

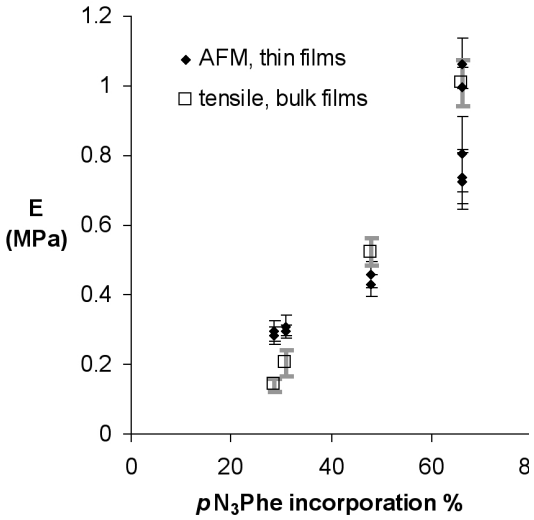

Figure A.9: Measured elastic moduli of thin films of aE-pN$_3$Phe versus fraction replacement of Phe by pN$_3$Phe. Results from AFM nanoindentation of thin films and tensile testing of bulk films are compared.

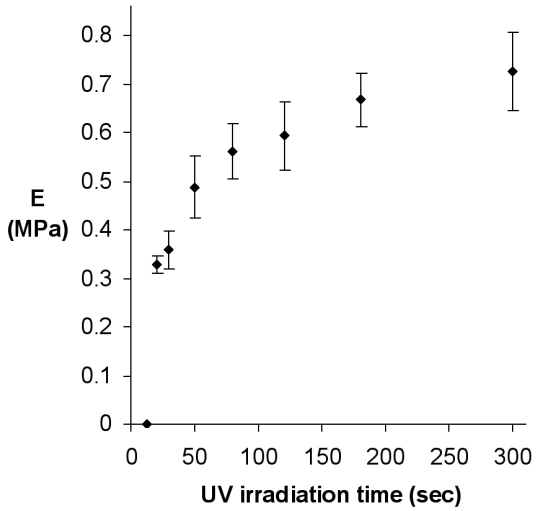

Figure A.10: Preparation of a step gradient in elastic modulus by variable irradiation of a single aE-66%-pN$_3$Phe film. Error bars indicate standard deviation in modulus within each zone of the gradient.

Modulus control by variable incorporation of pN$_3$Phe thin films. Figure A.9 compares the elastic moduli calculated from AFM data for thin films to those measured for bulk films in uniaxial tension. For aE-48%-pN$_3$Phe and aE-66%-pN$_3$Phe, the values match within experimental error, indicating that the mechanical properties of the bulk films can be reproduced in films 200-400 nm thick, and supporting the validity of the Dimitriadis model for measuring Young's modulus. The bulk and thin films, although cast from different solvents, are both crosslinked in the dry state, and are thus expected to have similar structures and elastic moduli. For films of lower pN$_3$Phe content, AFM yields moduli slightly higher than those obtained from tensile measurements (Table A.3).

Engineering of the elastic moduli of thin protein films by controlling pN$_3$Phe content should prove useful in cell culture experiments designed to study mechanosensitive cell behavior. An especially attractive prospect is the use of microfluidic mixing[15,39] to prepare protein substrates characterized by controlled gradients in elastic modulus.

Modulus control by variable irradiation. Elastic modulus gradients can also be prepared by variation in the radiation dose used for photocrosslinking. To demonstrate, we prepared a step-gradient by irradiating adjacent portions of an aE-66%-pN$_3$Phe film for increasing lengths of time. The elastic moduli measured (by AFM) at different locations on the film are shown in Figure A.10; the modulus increases slightly more than two-fold as the irradiation time increases from 20 to 300 sec. The majority of the rise in elastic modulus occurs over the first minute of exposure, consistent with the photolysis behavior reported previously.[24]

When the gradient film was washed to remove soluble protein, the thicknesses of the 20 sec and 30 sec zones were ca. 35% and ca. 20%, respectively, less than the thickness of the zones irradiated for longer periods, indicating incomplete crosslinking. Taking into account the known film height (as in the Dimitriadis calculation of the modulus) is essential for these gradient films, since variable film height would make the Hertz model inaccurate even as a comparative measure of the local elastic modulus.

Films that exhibit spatial variation in modulus on millimeter length scales offer unique advantages as substrates for the study of cell behavior. Large numbers of cells can be cultured on each zone

of a step-gradient substrate, allowing average cell properties to be measured as a function of elastic modulus on a single substrate. This approach minimizes reagent use and substrate preparation, and avoids lot-to-lot variation in the behavior of cultured cells. Observation of cell behavior at interfaces between stiff and soft materials has also proven instructive.[6] Films with more complex patterns of mechanical properties can also be envisioned. Irradiation through a mask, used previously to pattern proteins on solid supports,[24] could be easily adapted to the preparation of films with micropatterned moduli. Cell behavior on micropatterned materials has been the subject of a recent study.[40]

While step gradients are easy to characterize with a limited number of indentations, films with smooth gradients of elastic modulus could also be made via the variable irradiation approach by moving an opaque shutter continuously across the film.[41] Gradients could be implemented over a variety of length scales. The spatial resolution of the modulus measurement is limited only by the 300 nm radius of the tip used for indentation, and is adequate for measurement of the variation in mechanical properties under a single spread cell. Even higher resolution might be achieved through use of conventional sharp (< 20 nm) conical or pyramidal tips together with finite element analysis of the indentation process. Gradients extending over distances greater than the ca. 100 μm lateral piezo range of conventional AFM instruments could be characterized by using translational reference points in the sample.

Conclusions

Incorporation of the photosensitive amino acid *p*-azidophenylalanine into artificial proteins enables the photochemical synthesis of thin protein films of controlled elastic modulus. A film height-dependent indentation model, validated by bulk tensile measurements and finite element simulation, allows the elastic modulus to be determined with confidence by nanoindentation. The thin films prepared in this work enable new approaches to the study of mechanosensitive cell behavior in the context of coincident biological signals.

Acknowledgment

We gratefully acknowledge support of this research by the Center for the Science and Engineering of Materials at Caltech (NSF DMR-0520565) and by NIH grant EB1971. We thank Marissa Mock for NMR characterization and Doron Shilo for help with AFM measurements.

References and Notes

(1) Discher, D. E.; Janmey, P.; Wang, Y. L. *Science* **2005**, *310*, 1139-1143.

(2) Pelham, R. J.; Wang, Y. L. *Proc. Natl. Acad. Sci. U.S.A.* **1997**, *94* 13661-13665.

(3) Cukierman, E.; Pankov, R.; Stevens, D. R.; Yamada, K. M. *Science* **2001**, *294*, 1708-1712.

(4) Engler, A.; Bacakova, L.; Newman, C.; Hategan, A.; Griffin, M.; Discher, D. *Biophys. J.* **2004**, *86*, 617-628.

(5) Engler, A. J.; Richert, L.; Wong, J. Y.; Picart, C.; Discher, D. E. *Surf. Sci.* **2004**, *570*, 142-154.

(6) Lo, C. M.; Wang, H. B.; Dembo, M.; Wang, Y. L. *Biophys. J.* **2000**, *79*, 144-152.

(7) Gray, D. S.; Tien, J.; Chen, C. S. J. *Biomed. Mater. Res. A* **2003**, *66A*, 605-614.

(8) Wang, H. B.; Dembo, M.; Wang, Y. L. *Am. J. Physiol. - Cell Ph.* **2000**, *279*, C1345-C1350.

(9) Engler, A. J.; Griffin, M. A.; Sen, S.; Bonnetnann, C. G.; Sweeney, H. L.; Discher, D. E. *J. Cell Biol.* **2004**, *166*, 877-887.

(10) Engler, A. J.; Sen, S.; Sweeney, H. L.; Discher, *D. E. Cell* **2006**, *126*, 645-647.

(11) Engler, A. J.; Rehfeldt, F.; Sen, S.; Discher, D. E. *Methods Cell Biol.* **2007**, *83*, 521-545.

(12) Wang, Y. L.; Pelham, R. J. *In Molecular Motors and the Cytoskeleton*, Pt B, **1998**, *298*, 489-496.

(13) Maskarinec, S. A.; Tirrell, D. A. *Curr. Opin. Biotechnol.* **2005**, *16*, 422-426.

(14) Wong, J. Y.; Velasco, A.; Rajagopalan, P.; Pham, Q. *Langmuir **2003***, *19*, 1908-1913.

(15) Zaari, N.; Rajagopalan, P.; Kim, S. K.; Engler, A. J.; Wong, J. Y. *Adv. Mater.* **2004**, *16*, 2133-2137.

(16) Panitch, A.; Yamaoka, T.; Fournier, M. J.; Mason, T. L.; Tirrell, D. A. *Macromolecules* **1999**, *32*, 1701-1703.

(17) Welsh, E. R.; Tirrell, D. A. *Biomacromolecules* **2000**, *1*, 23-30.

(18) Di Zio, K.; Tirrell, D. A. *Macromolecules* **2003**, *36*, 1553-1558.

(19) Liu, J. C.; Heilshorn, S. C.; Tirrell, D. A. *Biomacromolecules* **2004**, *5*, 497-504.

(20) Mould, A. P.; Komoriya, A.; Yamada, K. M.; Humphries, M. J. *J. Biol. Chem.* **1991**, *266*, 3579-3585.

(21) Urry, D. W. *J. Phys. Chem. B* **1997**, *101*, 11007-11028.

(22) Kast, P.; Hennecke, H. *J. Mol. Biol.* **1991**, *222*, 99-124.

(23) Kirshenbaum, K.; Carrico, I. S.; Tirrell, D. A. *Chembiochem* **2002**, *3*, 235-237.

(24) Carrico, I. S.; Maskarinec, S. A.; Heilshorn, S. C.; Mock, M. L.; Liu, J. C.; Nowatzki, P. J.; Franck, C.; Ravichandran, G.; Tirrell, D.A. *J. Am. Chem. Soc.* **2007**, *129*, 4874-4875.

(25) Vinckier, A.; Semenza, G. *FEBS Lett.* **1998**, *430*, 12-16.

(26) Cappella, B.; Dietler, G. *Surface Science Reports* **1999**, *34*, 1-103.

(27) Heinz, W. F.; Hoh, J. H. *Trends Biotechnol.* **1999**, *17*, 143-150.

(28) Mahaffy, R. E.; Shih, C. K.; MacKintosh, F. C.; Kas, *J. Phys. Rev. Lett.* **2000**, *85*, 880-883.

(29) Richert, L.; Engler, A. J.; Discher, D. E.; Picart, C. *Biomacromolecules* **2004**, *5*, 1908-1916.

(30) Costa, K. D.; Yin, F. C. P. *J. Biomech. Eng.* **1999**, *121*, 462-471.

(31) Dimitriadis, E. K.; Horkay, F.; Maresca, J.; Kachar, B.; Chadwick, R. S. *Biophys. J.* **2002**, *82*, 2798-2810.

(32) Domke, J.; Radmacher, M. *Langmuir* **1998**, *14*, 3320-3325.

(33) Akhremitchev, B. B.; Walker, G. C. *Langmuir* **1999**, *15*, 5630-5634.

(34) Sharma, N. Ph.D. Thesis, University of Massachusetts Amherst, 2001.

(35) Nowatzki, P. J.; Tirrell, D. A. *Biomaterials* **2004**, *25*, 1261-1267.

(36) Yeoh, O. H. *Rubber Chem. Technol.* **1993**,*66*, 754-771.

(37) Flory, P. J. *Principles of Polymer Chemistry*; Cornell University Press: Ithaca, NY, 1953.

(38) Lillie, M. A.; Gosline, J. M. *Biopolymers* **2002**, *64*, 115-126.

(39) Jeon, N. L.; Dertinger, S. K. W.; Chiu, D. T.; Choi, I. S.; Stroock, A. D.; Whitesides, G.M. *Langmuir* **2000**, *16*, 8311-8316.

(40) Stevens, M. M.; George, J. H. *Science* **2005**, *310*, 1135-1138.

(41) Pucci, V.; Raggi, M. A.; Svec, F.; Frechet, J. M. J. *J. Sep. Sci.* **2004**, *27*, 779-788.

Bibliography

[1] B. Alberts, A. Johnson, J. Lewis, M. Raff, K. Roberts, and P. Walter. *Molecular biology of the cell*. Garland Science, 4th edition, 2002.

[2] R. Ananthakrishnan and A. Ehrlicher. The forces behind cell movement. *International Journal of Biological Sciences*, 3(5):303–317, 2007.

[3] N.Q. Balaban, U.S. Schwarz, D. Riveline, P. Goichberg, G. Tzur, I. Sabanay, D. Mahalu, S. Safran, A. Bershadsky, L. Addadi, and B. Geiger. Force and focal adhesion assembly: a close relationship studied using elastic micropatterned substrates. *Nature Cell Biology*, 3(5):466–472, 2001.

[4] B.K. Bay, T.S. Smith, D.P. Fyhrie, and M. Saad. Digital volume correlation: Three-dimensional strain mapping using x-ray tomography. *Experimental Mechanics*, 39(3):217–226, 1999.

[5] K.A. Beningo, K. Hamao, M. Dembo, Y.L. Wang, and H. Hosoya. Traction forces of fibroblasts are regulated by the rho-dependent kinase but not by the myosin light chain kinase. *Archives of Biochemistry and Biophysics*, 456(2):224–231, 2006.

[6] K. Bhadriraju, M. Yang, S.A. Ruiz, D. Pirone, J. Tan, and C.S. Chen. Activation of rock by rhoa is regulated by cell adhesion, shape, and cytoskeletal tension. *Experimental Cell Research*, 313(16):3616–3623, 2007.

[7] J.P. Butler, I.M. Tolic-Norrelykke, B. Fabry, and J.J. Fredberg. Traction fields, moments, and strain energy that cells exert on their surroundings. *American Journal of Physiology - Cell Physiology*, 282(3):C595–C605, 2002.

[8] I.S. Carrico, S.A. Maskarinec, S.C. Heilshorn, M.L. Mock, J.C. Liu, P.J. Nowatzki, C. Franck, G. Ravichandran, and D.A. Tirrell. Lithographic patterning of photoreactive cell-adhesive proteins. *Journal of the American Chemical Society*, 129(16):4874ff., 2007.

[9] D.J. Chen, F.P. Chiang, Y.S. Tan, and H.S. Don. Digital speckle-displacement measurement using a complex spectrum method. *Applied Optics*, 32(11):1839–1849, 1993.

[10] T.C. Chu, W.F. Ranson, M.A. Sutton, and W.H. Peters. Applications of digital-image-correlation techniques to experimental mechanics. *Experimental Mechanics*, 25(3):232–244, 1985.

[11] T.R. Corle and G.S. Kino. *Confocal scanning optical microscopy and related imaging systems*. Academic Press, San Diego, xv edition, 1996.

[12] E. Cukierman, R. Pankov, D.R. Stevens, and K.M. Yamada. Taking cell-matrix adhesions to the third dimension. *Science*, 294(5547):1708–1712, 2001.

[13] M. Dembo, T. Oliver, A. Ishihara, and K. Jacobson. Imaging the traction stresses exerted by locomoting cells with the elastic substratum method. *Biophysical Journal*, 70(4):2008–2022, 1996.

[14] M. Dembo and Y.L. Wang. Stresses at the cell-to-substrate interface during locomotion of fibroblasts. *Biophysical Journal*, 76(4):2307–2316, 1999.

[15] A. Diaspro, F. Federici, and M. Robello. Influence of refractive-index mismatch in high-resolution three-dimensional confocal microscopy. *Applied Optics*, 41(4):685–690, 2002.

[16] S. Even-Ram and K.M. Yamada. Cell migration in 3d matrix. *Current Opinion Cell Biology*, 17(5):524–532, 2005.

[17] C. Franck, S. Hong, S.A. Maskarinec, D.A. Tirrell, and G. Ravichandran. Three-dimensional full-field measurements of large deformations in soft materials using confocal microscopy and digital volume correlation. *Experimental Mechanics*, 47(3):427–438, 2007.

[18] F. Ghahremani. Effect of grain-boundary sliding on anelasticity of polycrystals. *International Journal of Solids and Structures*, 16(9):825–845, 1980.

[19] M. Gu. *Principles of Three-Dimensional Imaging in Confocal Microscopes*. World Scientific, 1996.

[20] A.K. Harris, P. Wild, and D. Stopak. Silicone-rubber substrata - new wrinkle in the study of cell locomotion. *Science*, 208(4440):177–179, 1980.

[21] S.C. Heilshorn, K.A. DiZio, E.R. Welsh, and D.A. Tirrell. Endothelial cell adhesion to the fibronectin cs5 domain in artificial extracellular matrix proteins. *Biomaterials*, 24(23):4245–4252, 2003.

[22] S. Hong and G. Ravichandran, 2007. FFT-Based digital image correlation algorithm for large deformation measurements. Galcit SM Technical Report, California Institute of Technology, Pasadena, CA.

[23] H. Huang, R.D. Kamm, and R.T. Lee. Cell mechanics and mechanotransduction: pathways, probes, and physiology. *American Journal of Physiology - Cell Physiology*, 284(1):C1–C11, 2004.

[24] D.E. Ingber, L. Dike, L. Hansen, S. Karp, H. Liley, A. Maniotis, H. McNamee, D. Mooney, G. Plopper, J. Sims, and N. Wang. Cellular tensegrity - exploring how mechanical changes in the cytoskeleton regulate cell-growth, migration, and tissue pattern during morphogenesis. *International Review of Cytology - A Survey of Cell Biology*, 150:173–224, 1994.

[25] L.D. Landau and E.M. Lifshitz. *Theory of Elasticity*. Pergamon Press, Oxford, UK, 3rd edition, 1986.

[26] F. Lanza di Scalea, S.S. Hong, and G.L. Cloud. Whole-field strain measurement in a pin-loaded plate by electronic speckle pattern interferometry and the finite element method. *Experimental Mechanics*, 38(1):55–60, 1998.

[27] J. Lee, M. Leonard, T. Oliver, A. Ishihara, and K. Jacobson. Traction forces generated by locomoting keratocytes. *Journal of Cell Biology*, 127(6):1957–1964, 1994.

[28] J.C. Liu, S.C. Heilshorn, and D.A. Tirrell. Comparative cell response to artificial extracellular matrix proteins containing the rgd and cs5 cell-binding domains. *Biomacromolecules*, 5(2):497–504, 2004.

[29] C.M. Lo, H.B. Wang, M. Dembo, and Y.L. Wang. Cell movement is guided by the rigidity of the substrate. *Biophysical Journal*, 79(1):144–152, 2000.

[30] L.B. Lucy. Iterative technique for rectification of observed distributions. *Astronomical Journal*, 79(6):745–754, 1974.

[31] R. Merkel, N. Kirchgebner, C.M. Cesa, and B. Hoffmann. Cell force microscopy on elastic layers of finite thickness. *Biophysical Journal*, 93(9):3314–3323, 2007.

[32] C.T. Mierke, D. Roesel, B. Fabry, and J. Brabek. Contractile forces in tumor cell migration. *European Journal of Cell Biology, (in press)*, 2008.

[33] P.J. Nowatzki, C. Franck, S.A. Maskarinec, G. Ravichandran, and D.A. Tirrell. Mechanically tunable thin films of photosensitive artificial proteins: Preparation and characterization by nanoindentation. *Macromolecules*, 41(5):1839–1845, 2008.

[34] T. Oliver, M. Dembo, and K. Jacobson. Traction forces in locomoting cells. *Cell Motility and the Cytoskeleton*, 31(3):225–240, 1995.

[35] R.J. Pelham and Y.L. Wang. Cell locomotion and focal adhesions are regulated by substrate flexibility. *Proceedings of the National Academy of Sciences, USA*, 94(25):13661–13665, 1997.

[36] S Petronis, J Gold, and B Kasemo. Microfabricated force-sensitive elastic substrates for investigation of mechanical cell-substrate interactions. *Journal of Micromechanics Microengineering*, 13(6):900–913, 2003.

[37] A.M. Pizzo, K. Kokini, L.C. Vaughn, B.Z. Waisner, and S.L. Voytik-Harbin. Extracellular matrix (ecm) microstructural composition regulates local cell-ecm biomechanics and fundamental fibroblast behavior: a multidimensional perspective. *Journal of Applied Physiology*, 98(5):1909–1921, 2005.

[38] C.A. Reinhart-King, M. Dembo, and D.A. Hammer. Endothelial cell traction forces on rgd-derivatized polyacrylamide substrata. *Langmuir*, 19(5):1573–1579, 2003.

[39] B.A. Roeder, K. Kokini, J.P. Robinson, and S.L. Voytik-Harbin. Local, three-dimensional strain measurements within largely deformed extracellular matrix constructs. *Journal of Biomechanical Engineering-Transactions of the ASME*, 126(6):699–708, 2004.

[40] B. Sabass, M.L. Gardel, C.M. Waterman, and U.S. Schwarz. High resolution traction force microscopy based on experimental and computational advances. *Biophysical Journal*, 94(1):207–220, 2008.

[41] U.S. Schwarz, N.Q. Balaban, D. Riveline, L. Addadi, A. Bershadsky, S.A. Safran, and B. Geiger. Measurement of cellular forces at focal adhesions using elastic micro-patterned substrates. *Materials Science and Engineering C-Biomimetic and Supramolecular Systems*, 23(3):387–394, 2003.

[42] U.S. Schwarz, N.Q. Balaban, D. Riveline, A. Bershadsky, B. Geiger, and S.A. Safran. Calculation of forces at focal adhesions from elastic substrate data: The effect of localized force and the need for regularization. *Biophysical Journal*, 83(3):1380–1394, 2002.

[43] C. Sheppard and D. Shotton. *Confocal laser scanning microscopy*. BIOS Scientific; Springer, in association with the Royal Microscopical Society, Oxford, New York, xii edition, 1997.

[44] C.J.R. Sheppard and P. Torok. Effects of specimen refractive index on confocal imaging. *Journal of Microscopy*, 185:366–374, 1997.

[45] F.H. Silver. *Mechanosensing and mechanochemical transduction in extracellular matrix*. Springer, 2006.

[46] T.S. Smith, B.K. Bay, and M.M. Rashid. Digital volume correlation including rotational degrees of freedom during minimization. *Experimental Mechanics*, 42(3):272–278, 2002.

[47] J.K. Stevens, L.R. Mills, and J.E. Trogadis. *Three-Dimensional Confocal Microscopy: Volume Investigation of Biological Systems*. Academic Press. San Diego, 1994.

[48] K. Takita, Y. Sasaki, T. Higuchi, and K. Kobayashi. High-accuracy subpixel image registration based on phase-only correlation. *Leice Transactions on Fundamentals of Electronics Communications and Computer Sciences*, E86A(8):1925–1934, 2003.

[49] J.L. Tan, J. Tien, D.M. Pirone, D.S. Gray, K. Bhadriraju, and C.S. Chen. Cells lying on a bed of microneedles: An approach to isolate mechanical force. *Proceedings of the National Academy of Sciences, USA*, 100(4):1484–1489, 2003.

[50] Y. Tian, N. Pesika, H.B. Zeng, K. Rosenberg, B.X. Zhao, P. McGuiggan, K. Autumn, and J. Israelachvili. Adhesion and friction in gecko toe attachment and detachment. *Proceedings of the National Academy of Sciences, USA*, 103(51):19320–19325, 2006.

[51] P. Torok, P. Varga, and G.R. Booker. Electromagnetic diffraction of light focused through a planar interface between materials of mismatched refractive-indexes - structure of the electromagnetic-field. *Journal of the Optical Society of America A - Optics Image Science and Vision*, 12(10):2136–2144, 1995.

[52] T.D. Visser, J.L. Oud, and G.J. Brakenhoff. Refractive-index and axial distance measurements in 3-d microscopy. *Optik*, 90(1):17–19, 1992.

[53] V. Vogel and M. Sheetz. Local force and geometry sensing regulate cell functions. *Nature Reviews Molecular Cell Biology*, 7(4):265–275, 2006.

[54] J.H.C. Wang and J.S. Lin. Cell traction force and measurements methods. *Biophysical Journal*, 6(6):361–371, 2007.

[55] M.H. Zaman, R.D. Kamm, P. Matsudaira, and D.A. Lauffenburger. Computational model for cell migration in three-dimensional matrices. *Biophysical Journal*, 89(2):1389–1397, 2005.